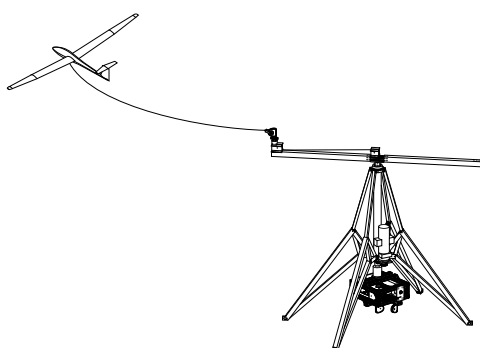


# Design and Operation of Airborne Wind Energy Systems

Experimental Validation of Moving Horizon  
Estimation for Pose Estimation



**Kurt Geebelen**

Dissertation presented in partial  
fulfilment of the requirements for the  
degree of Doctor in Engineering  
Science

April 2015



# **Design and Operation of Airborne Wind Energy Systems**

Experimental Validation of Moving Horizon Estimation for Pose Estimation

**Kurt GEEBELEN**

Examination committee:

Prof. dr. ir. J. Berlamont, chair  
Prof. dr. ir. J. Swevers, supervisor  
Prof. Dr. M. Diehl, co-supervisor  
Prof. dr. ir. D. Vandepitte  
Prof. dr. ir. J. De Schutter  
Prof. dr. ir. F. Logist  
Dr. Ing. R. Schmehl  
(Delft University of Technology)

Dissertation presented in partial fulfilment of the requirements for the degree of Doctor in Engineering Science

April 2015

© 2015 KU Leuven – Faculty of Engineering Science  
Uitgegeven in eigen beheer, Kurt Geebelen, Celestijnenlaan 300B box 2420, B-3001 Leuven (Belgium)

Alle rechten voorbehouden. Niets uit deze uitgave mag worden vermenigvuldigd en/of openbaar gemaakt worden door middel van druk, fotokopie, microfilm, elektronisch of op welke andere wijze ook zonder voorafgaande schriftelijke toestemming van de uitgever.

All rights reserved. No part of the publication may be reproduced in any form by print, photoprint, microfilm, electronic or any other means without written permission from the publisher.

# Preface

The story of my PhD starts back in the spring of 2009, the day before we had to submit our top 5 of master thesis topics. I met Joris Gillis in the bicycle parking at the mechanical engineering department, and went through the list with him one last time. It was at this point we saw the topic about harvesting wind power using kites, and we were both immediately interested. We directly went to the supervising assistant to get more information and were sold. We both put the subject at the top of our list, and were lucky enough to get it. If it wasn't for this coincidence, I may never have started a PhD. Halfway through my master thesis, I still liked the subject so much that I didn't have to think long about doing a PhD about it.

Now, 6 years after my first contact with Airborne Wind Energy, I have a lot of people to thank. First of all I would like to thank my supervisors Jan and Moritz for supporting me and giving me the opportunity to work on such an exciting subject! I also want to express my gratitude to the examination committee for their constructive comments and suggestions.

I also want to thank all members, past and current, of the Highwind team: Andrew, Milan, Greg, Mario, Joris, Reinhart, Sebastien, Hammad, Julia, all of you have helped me in some way, and without you, I can't imagine where the project would be now. I therefore also want to thank the European Research Council for providing the financial support. A lot of help also came through master theses. For this, I want to thank Mathias, Jeroen, Wouter, Bram, Dries and Kurt, thanks for being motivated to work for someone who didn't always exactly know what he wanted.

The construction of experimental set-ups is not a one-man job. I want to thank Rudi Casteels, who put many days, weeks, even months in the mechanical construction of the outdoors carousel. Building a set-up also means a lot of things need to be purchased. I sincerely want to thank Jacqueline, John and Elsy for all their help. It was always much appreciated.

I am also grateful to all my colleagues from PMA and ESAT for all the discussions during the many lunch breaks we had together. I especially thank my office mates Jan, Shoaib, Ke, Johan and Sebastiaan for all the good times we had in our office.

I thank my family and especially Liesl, for always being there for me, also during difficult times. Thank you to my friends for providing plenty of distractions from work. Much gratitude goes to my fellow teammates of Cauberg VV for the many Saturdays on which I could try to kick a football.

*Kurt Geebelen  
Leuven, April 2015*

# Abstract

Global climate change as well as water and air pollution lead to a demand for a sustainable energy supply. Renewable energy sources such as wind and solar power, hydro-electric power and geothermal energy, together with energy efficiency measures, are a viable alternative to fossil fuels. Focussing the attention on wind energy it is interesting to note that Airborne Wind Energy (AWE) has the potential to capture wind energy at a fraction of the cost achievable by current wind turbines. In the method explored in this thesis, an aeroplane flies a crosswind trajectory while it is tethered to a ground based winch. This winch consists of a drum connected to a motor/generator. The tether is wound up on the drum, and electricity is produced using the '*pumping cycle*'. In the first phase of the pumping cycle, the aeroplane delivers a high traction force on the tether while it is being reeled out, causing the generator to produce electricity. Once the tether is fully unrolled, the aeroplane is controlled such that the force on the tether is reduced and the tether is reeled in using only a fraction of the electricity produced in the first phase.

Unfortunately the benefits of airborne wind energy come at a cost. While a wind turbine only needs to be aimed towards the wind to operate, an AWE system needs to be constantly controlled to fly a certain crosswind trajectory. Because of this, AWE systems need an automatic control system, which in turn needs a reliable estimate of the system state.

The first part of this dissertation discusses the development of two experimental AWE test set-ups, one set-up for indoors use and one set-up for outdoors use. The goal of these set-ups is to analyse and experimentally validate the rotation start, a start-up method for AWE systems in which the tethered aeroplane is brought up to speed by an arm rotating around a central vertical axis. The dissertation presents the development and design choices for both set-ups.

The indoors set-up is equipped with sensors that allow estimating the position and orientation of the aeroplane, including an Inertial Measurement Unit (IMU)

that measures the acceleration and angular velocity of the aeroplane, and a stereo vision system that offers measurements of the aeroplane's position and orientation. The outdoors set-up is larger than the indoors set-up and mobile to allow experiments to be done at remote locations using larger aeroplanes. The set-ups will be used to implement and experimentally validate advanced, optimisation-based state and parameter estimation techniques and in the future advanced control techniques.

The second part of this dissertation investigates methods to fuse the different sensor measurements to form a reliable state estimate. Moving Horizon Estimation (MHE) is presented as a technique that can reliably fuse the information from the nonlinear system and measurement models and compared to traditional methods such as the extended and unscented Kalman filter using both simulations and experimental data obtained on the indoors set-up. MHE is shown to have both a better start-up behaviour and average estimation performance than Kalman filtering techniques.

Estimators based on both a kinematic and a dynamic model are presented. The developed moving horizon estimator based on a dynamic model of the system is shown to have better estimation performance than estimation based on a kinematic model, at the cost of an increase in computation time.

A main concern of the developed estimators is the limited sampling rate caused by the computational load of the MHE. To relieve this limitation and achieve higher update frequencies, a novel approach using a second inner MHE is presented. This inner MHE uses the IMU measurements to update the state estimates and is shown to perform better than traditional dead reckoning for long prediction times.

# Beknopte samenvatting

Wereldwijde klimaatverandering en water- en luchtvervuiling leiden naar de vraag voor een duurzame energievoorziening. Hernieuwbare energiebronnen zoals wind- en zonne-energie, waterkracht en geothermische energie, in combinatie met betere energie-efficiëntie zijn een mogelijk alternatief voor fossiele brandstoffen. Als we de aandacht vestigen op windenergie is het interessant om op te merken dat *Airborne* windenergie (AWE) het potentieel heeft om windenergie op te wekken aan een fractie van de kost van conventionele windturbines. Airborne slaat hier op het door de wind in de lucht gehouden worden van een deel van het systeem. In de methode die in deze thesis wordt onderzocht vliegt een vliegtuig een traject dwars op de wind terwijl het met een kabel aan een generator op de grond is bevestigd. In een eerste fase levert het vliegtuig een hoge kracht op de kabel terwijl deze wordt uitgerold, waardoor de generator elektriciteit produceert. Wanneer de kabel volledig is uitgerold wordt het vliegtuig zo gecontroleerd zodat de kracht op de kabel verminderd. De kabel wordt nu ingerold waarbij slechts een klein deel van de elektriciteit die tijdens de eerste fase werd opgewekt weer wordt gebruikt.

Het eerste deel van dit proefschrift bespreekt de ontwikkeling van twee experimentele testopstellingen, een opstelling voor binnenshuis gebruik en een opstelling voor buitenshuis gebruik. Het doel van deze opstellingen is om de rotatiestart te analyseren en experimenteel te valideren. De rotatiestart is een startmethode voor AWE systemen waarbij de vlieger op snelheid gebracht wordt door een arm die rond een centrale as draait. Het proefschrift presenteert de ontwikkeling en de ontwerpkeuzes voor beide opstellingen.

De opstelling voor binnenshuis gebruik is uitgerust met sensoren die toelaten om de positie en oriëntatie van het vliegtuig te schatten, zoals onder meer een IMU die de versnelling en rotatiesnelheid van het vliegtuig meet, en een stereovisie systeem dat metingen van de positie en oriëntatie van het vliegtuig biedt. De opstelling voor buitenshuis gebruik is groter dan de opstelling voor binnenshuis gebruik en is verplaatsbaar om experimenten met grotere vliegtuigen op afgelegen

locaties toe te laten. Beide opstellingen zullen gebruikt worden om geavanceerde, op optimalisatie gebaseerde parameter- en toestandsschattingstechnieken, en in de toekomst geavanceerde controletechnieken, te implementeren en experimenteel te valideren.

Het tweede deel van dit proefschrift onderzoekt methoden om de metingen van de verschillende sensoren met elkaar te combineren om een betrouwbare toestandsschatting te vormen. De glijdende-horizon schatter (*Moving Horizon Estimator*) wordt voorgesteld als techniek die betrouwbaar de informatie van de niet-lineaire systeem- en meetmodellen kan combineren, en wordt vergeleken met traditionele methoden zoals de *extended* en *unscented* Kalman filter op basis van zowel simulaties als experimentele data verkregen op de opstelling voor binnenshuis gebruik. Het wordt aangetoond dat de glijdende-horizon schatter een beter opstartgedrag en gemiddelde schattingssprestatie biedt dan de Kalman filters.

Schatters gebaseerd op zowel een kinematisch als op een dynamisch model worden voorgesteld. Het wordt aangetoond dat de ontwikkelde glijdende-horizon schatter gebaseerd op een dynamisch model van het systeem een betere schattingssprestatie heeft dan schatting gebaseerd op een kinematisch model, ten koste van het toenemen van de nodige rekentijd.

Een belangrijke bezorgdheid van de ontwikkelde schatters is de lage bemonsteringsfrequentie, veroorzaakt door de rekenkracht nodig voor de glijdende-horizon schatter. Om deze beperking te verminderen en schattingen aan een hogere frequentie te verkrijgen wordt een nieuwe manier, gebruik makende van een tweede binnennste glijdende-horizon schatter, voorgesteld. Deze binnennste glijdende-horizon schatter gebruikt de metingen van de IMU om de toestandsschattingen bij te werken en het wordt aangetoond dat deze manier beter presteert dan gegist bestek voor lange voorspellingstijden.

# Abbreviations

ACADO	Toolkit for Automatic Control and Dynamic Optimisation
AWE	Airborne Wind Energy
DAE	Differential Algebraic Equation
EKF	Extended Kalman filter
IMU	Inertial Measurement Unit
KF	Kalman filter
MHE	Moving Horizon Estimation
NMPC	Nonlinear Model Predictive Control
OCP	Optimal control problem
ODE	Ordinary Differential Equation
QP	Quadratic Program
RTI	Real Time Iteration
UKF	Unscented Kalman filter



# Contents

<b>Abstract</b>	<b>iii</b>
<b>Contents</b>	<b>ix</b>
<b>List of Figures</b>	<b>xv</b>
<b>List of Tables</b>	<b>xix</b>
<b>1 Introduction</b>	<b>1</b>
1.1 Introduction to airborne wind energy . . . . .	1
1.2 Performance of an AWE system . . . . .	5
1.3 Existing AWE prototypes . . . . .	8
1.4 Launch methods for AWE systems . . . . .	12
1.5 The rotation start . . . . .	15
1.6 Objective and contributions of the thesis . . . . .	18
1.7 Thesis outline . . . . .	19
<b>I Test devices for AWE</b>	<b>21</b>
<b>2 Description of the indoors test set-up</b>	<b>23</b>
2.1 Introduction . . . . .	23

2.2	Carousel design . . . . .	24
2.3	Winch and tether . . . . .	25
2.4	Aeroplane . . . . .	26
2.5	Measurement system . . . . .	27
2.6	Data acquisition system . . . . .	29
2.7	Software . . . . .	29
2.8	Conclusion . . . . .	31
<b>3</b>	<b>Design and development of the outdoors test set-up</b>	<b>33</b>
3.1	Introduction . . . . .	33
3.2	Requirements . . . . .	34
3.3	Balanced kites set-up . . . . .	35
3.3.1	Double tether . . . . .	35
3.3.2	Single tether . . . . .	37
3.3.3	Selected configuration and conceptual design . . . . .	39
3.4	Single kite set-up . . . . .	41
3.4.1	Carousel . . . . .	41
3.4.2	Winch . . . . .	44
3.4.3	Aeroplane . . . . .	49
3.4.4	Electrical design . . . . .	49
3.4.5	Line angle sensor . . . . .	51
3.5	Conclusion . . . . .	55
<b>II</b>	<b>MHE with application to AWE</b>	<b>57</b>
<b>4</b>	<b>State estimation</b>	<b>59</b>
4.1	Introduction . . . . .	59

4.2	Model representation . . . . .	59
4.3	Full information estimation . . . . .	61
4.4	Recursive state estimation . . . . .	62
4.4.1	Kalman filter . . . . .	63
4.4.2	Extended Kalman filter . . . . .	66
4.4.3	Unscented Kalman filter . . . . .	67
4.5	Moving Horizon Estimation . . . . .	70
4.5.1	Problem formulation . . . . .	71
4.5.2	Solution method . . . . .	72
4.5.3	Benefits of MHE . . . . .	73
4.6	Conclusion . . . . .	73
<b>5</b>	<b>Moving horizon estimation with a kinematic model</b>	<b>75</b>
5.1	Introduction . . . . .	75
5.2	Kinematic model for AWE system . . . . .	76
5.2.1	State definition . . . . .	76
5.2.2	Model equations . . . . .	79
5.3	Measurement model for stereo vision system . . . . .	80
5.4	Estimation problem . . . . .	82
5.5	Discretisation of continuous problem . . . . .	84
5.6	Choices for penalty function . . . . .	88
5.6.1	Least Squares Estimation . . . . .	88
5.6.2	Robust Estimation . . . . .	89
5.7	Simulation results . . . . .	91
5.8	Results with experimental data . . . . .	92
5.9	Conclusion . . . . .	95
<b>6</b>	<b>Moving horizon estimation and control with a dynamic model</b>	<b>97</b>

6.1	Introduction . . . . .	97
6.2	Dynamic model for AWE system . . . . .	99
6.2.1	State definition . . . . .	99
6.2.2	Model equations . . . . .	100
6.2.3	Process noise . . . . .	104
6.2.4	Minimal versus natural coordinates . . . . .	105
6.3	Outer estimation problem . . . . .	106
6.3.1	Polynomial approximation of the IMU measurements . .	106
6.3.2	Assessment of estimation performance . . . . .	109
6.3.3	MHE settings . . . . .	109
6.3.4	Comparison with dynamic Kalman filters . . . . .	115
6.3.5	Comparison with kinematic MHE . . . . .	116
6.4	Dead reckoning using fast MHE . . . . .	118
6.4.1	Setup . . . . .	118
6.4.2	MHE settings . . . . .	118
6.4.3	Results . . . . .	119
6.5	Closed loop control experiments . . . . .	120
6.5.1	Nonlinear Model Predictive Control . . . . .	121
6.5.2	Flight experiments and observations . . . . .	123
6.6	Conclusion . . . . .	126
<b>7</b>	<b>Concluding remarks</b>	<b>129</b>
7.1	Summary of the thesis . . . . .	129
7.2	Future work . . . . .	130
<b>Bibliography</b>		<b>133</b>
<b>A</b>	<b>Technical drawings of outdoors carousel</b>	<b>143</b>

<b>B Technical drawings of outdoors winch</b>	<b>161</b>
<b>C Parameters of the dynamic model</b>	<b>185</b>
<b>Curriculum Vitae</b>	<b>187</b>
<b>List of publications</b>	<b>189</b>



# List of Figures

1.1	Conventional wind turbines. . . . .	3
1.2	Graphical impression of a balanced kites system. . . . .	7
1.3	Average power output as a function of wing surface of a balanced kites system compared to a single kite system for aeroplanes with a gliding ratio of 25 at a reference wind speed of $10 \frac{\text{m}}{\text{s}}$ . . . . .	7
1.4	Airborne wind energy research and development activities by country and by team. Countries with academic or commercial activities in 2013 are coloured in dark grey. . . . .	8
1.5	AWE systems using soft kites. . . . .	9
1.6	AWE systems using hard kites. . . . .	10
1.7	Lighter-than-air systems and kite-powered water pump. . . . .	11
1.8	Skysails kite during launch. . . . .	12
1.9	Kitegen system using air blowers to launch the kite. . . . .	13
1.10	Piggy-back chin docking of flexible kite on an aerostat. . . . .	13
1.11	Lighter than air system supporting power generating turbine. .	14
1.12	The AWE system of Makani Power. . . . .	14
1.13	A schematic top view of the arm towing the aeroplane. . . . .	16
1.14	Transition trajectory for rotation start. . . . .	17
1.15	Example of a start-up and crosswind trajectory. . . . .	17

2.1	The final design and realisation of the carousel. . . . .	24
2.2	The final design and realisation of the winch. . . . .	25
2.3	Cable interaction and on-board power electronics. . . . .	26
2.4	Analog Devices ADIS16367 IMU. . . . .	27
2.5	Software overview. . . . .	30
2.6	The carousel in its current configuration. . . . .	31
3.1	Two configurations for the balanced kites set-up. . . . .	35
3.2	The winch drums mounted concentric with the carousel shaft but with an independent rotation speed. . . . .	37
3.3	Conceptual drawing of a tether clamping mechanism. . . . .	37
3.4	Pulley assembly at top of the arm that support tether in all directions. . . . .	38
3.5	Step 1: landing the airborne connection. . . . .	39
3.6	Step 2: gripping the short tethers. . . . .	40
3.7	Step 3: Bringing the attachment points to the end of the arm, reeling in the tethers and landing the kites. . . . .	40
3.8	The designed and built outdoors carousel. . . . .	42
3.9	Top and bottom bearing assemblies. . . . .	43
3.10	Side views of winch. . . . .	45
3.11	Linear guide of level wind mechanism. . . . .	45
3.12	Swivelling pulley used for level wind mechanism. . . . .	47
3.13	Swivelling pulleys as mounted on the winch. . . . .	48
3.14	Connection between the winch and the carousel. . . . .	48
3.15	Siemens proposal for electrical drive system. . . . .	50
3.16	Line angle sensor. . . . .	53
3.17	Schematic representation of tether path through line angle sensor. . . . .	53
3.18	Tether guide at end of guidance rod with spirals such that the tether can be looped through. . . . .	54

4.1	Graphical representation of null space decomposition. . . . .	65
4.2	Illustration of MHE for system with one state and measurements of that state. . . . .	72
5.1	Frame definitions. . . . .	77
5.2	Representation of pinhole camera. . . . .	81
5.3	Illustration of the measurements. . . . .	82
5.4	The relative measurements are projected on a polynomial basis and then used in MHE. These polynomials are also affected by the absolute measurements through the kinematic model. . . . .	84
5.5	The Gram polynomials up to order 4 for a grid of 50 nodes. . . . .	87
5.6	Huber penalty function and 2-norm. . . . .	90
5.7	Reprojection of MHE state estimate on camera image for one marker on one image. . . . .	93
5.8	Error in pose estimates. . . . .	94
5.9	Camera image reprojection of state estimate for one marker on one image. . . . .	95
5.10	$x$ -component of acceleration measurements and polynomials that fit this acceleration measurement for four frames of one MHE solution. . . . .	95
6.1	z-component of acceleration measurements and polynomials that fit these measurements for ten frames of one MHE solution. . . . .	111
6.2	Root mean square of estimation error of MHE for position, orientation, velocity and angular velocity in function of horizon length. . . . .	113
6.3	Experimental performance of MHE for different horizon lengths. . . . .	114
6.4	Execution times of MHE based on dynamic model for different horizon lengths. . . . .	114
6.5	2-norm of pose estimate error of EKF compared to MHE. . . . .	116
6.6	2-norm of pose estimate error of UKF compared to MHE. . . . .	117

6.7	Execution times of MHE based on kinematic model for different horizon lengths. . . . .	118
6.8	Root mean square of position estimate error in function of prediction time for MHE and dead reckoning. . . . .	120
6.9	Root mean square of marker prediction error for MHE and dead reckoning. . . . .	121
6.10	Closed loop tracking behaviour for roll, angular velocity around the $z$ -axis and height. . . . .	124
6.11	Open loop behaviour for roll, angular velocity around the $z$ -axis and height. . . . .	124
6.12	Timing diagram of the closed loop system. . . . .	125

# List of Tables

2.1	Two available Inertial Measurement Units. . . . .	28
2.2	Sensors on indoors set-up. . . . .	29
5.1	State definition for kinematic model. . . . .	78
5.2	Control definition for kinematic model. . . . .	78
5.3	Average estimation error over 100 runs for EKF and MHE using Huber penalty function and $\ell_2$ -norm. . . . .	94
6.1	State definition for dynamic model. . . . .	99
6.2	Control definition for dynamic model. . . . .	99
6.3	Model comparison without aerodynamic forces, the computational times are averaged over $10^4$ function evaluations. . . . .	106
6.4	Model comparison with aerodynamic forces, the computational times are averaged over $10^4$ function evaluations. . . . .	106
6.5	Standard deviations of process and measurement noise. . . . .	110
6.6	Estimation performance, expressed as root mean square of the estimation error, for different orders of polynomials for approximation of acceleration measurements for MHE with a horizon length of 8 estimation intervals for a typical simulation. .	111
6.7	Estimation performance, expressed as root mean square of the estimation error, for different orders of polynomials for approximation of angular velocity measurements for MHE with a horizon length of 8 estimation intervals for a typical simulation.	112

6.8	Root mean square of marker prediction error in pixels for different experiments for MHEs with a horizon length of 16 estimation intervals. . . . .	117
6.9	Execution times and sampling periods of inner MHE for different horizon lengths. . . . .	119
6.10	Average prediction error of dead reckoning compared to inner MHE. . . . .	119
6.11	Execution times of the MHE and NMPC. . . . .	125
C.1	Parameters of dynamic model for the indoors carousel. . . . .	186
C.2	Parameters of aerodynamic model for the indoors carousel. . .	186

# Chapter 1

## Introduction

This chapter gives a general introduction to Airborne Wind Energy (AWE), discusses the motivation of this research, summarises the main contributions and outlines the structure of this thesis by giving a chapter-by-chapter overview.

This chapter first depicts the current energy crisis that leads to the necessity for cheap renewable energy technologies in Section 1.1. Airborne wind energy is proposed as a solution for this and is discussed in detail. In Section 1.2, the huge potential of AWE systems is shown. Section 1.3 gives an overview of prototypes that are developed by different groups around the world. Section 1.4 discusses some of the launch methods that are being used or investigated for these prototypes, and the rotation start, which is investigated in this thesis, is discussed in more detail in Section 1.5. Section 1.6 gives the objective and contributions of the thesis. Finally, Section 1.7 concludes with an overview of the remaining chapters of the thesis.

### 1.1 Introduction to airborne wind energy

One of the most urgent problems in today's society is the search for cheap renewable energy resources. The civilised society is almost completely dependent on fossil fuel sources for its energy needs, which is an uncomfortable and even scary fact. In Belgium, around 70% of the energy consumption in the period 2010–2014 is based on fossil fuels [90]. The three fossil fuels, oil, natural gas and coal, were formed millions of years ago from dead organisms that were buried and anaerobically decomposed. All fossil fuels are a finite energy resource. At

some point they are going to run out. Long before we reach that point, fossil fuels are going to become increasingly expensive. Fossil fuel sources are supplied by only a few producer countries, many of which united in a cartel known as OPEC whose decisions have considerable influence on international oil prices [75]. This situation gives rise to serious geopolitical and economic problems, affecting almost all of the world's countries.

Furthermore, the burning of fossil fuels contributes to climate change. Around 10% of the greenhouse gases emitted worldwide in 2012 come from the European Union [33]. In 2012 around 14% of the final energy consumption was generated from renewable sources in the EU. This is ahead of the planned trajectory to hit 20% renewable energy by 2020 in the EU2020 objectives [32]. These aim at, by the year 2020, reducing the greenhouse gas emissions by 20% compared to 1990, achieving an energy efficiency of 20 % and increasing the share of renewable energy in final energy consumption to 20%.

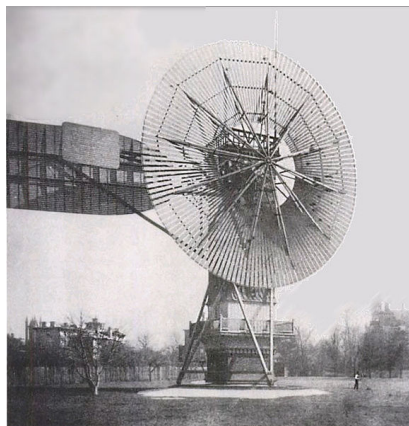
Another important energy source is nuclear energy. Under normal circumstances, approximately 54% of the electricity generated in Belgium comes from nuclear power plants, from in total 7 reactors; 4 in Doel and 3 in Tihange. In March 2015 however, two reactors, one in Doel and one in Tihange, are shut down due to small cracks in the reactor vessel [23] and another reactor in Doel was shut down in August 2014 due to an oil leak, presumably by sabotage [22]. Although nuclear energy has almost no carbon-emission and air pollution, opponents of nuclear energy contend it brings many threats to mankind and environment because of the nuclear waste that it creates, and also had hidden costs, for example when problems with the storage of the nuclear waste arise. After the earthquake and tsunami in Japan in 2011 struck the Fukushima nuclear power plant which resulted in the meltdown of 3 of its 6 reactors [95], worldwide concern about the safety of nuclear energy has grown. In Belgium, the current plan is to completely abolish the use of nuclear power by 2025. In the wake of the Fukushima disaster, Germany has closed 8 of its nuclear power plants, which conforms to the goals of the '*Energiewende*', Germany's ambition to completely move its energy sector towards renewable energy, energy efficiency and sustainable development. The final goal is the abolition of coal and other non-renewable energy sources [29].

Key points in all efforts towards a sustainable energy supply is reducing the energy usage by using more efficient technologies, reducing the energy demand and moving towards renewable energy resources such as hydropower, solar, wind, biomass and geothermal. In 2012 in Norway 97% of the installed electrical capacity was renewable energy, mainly hydropower [59], but this is exceptional and is not possible in every country. Worldwide, most major sites suited for hydropower are already being exploited. In most countries that do not have a large potential for hydropower such as Norway has, large investments are

needed to shift the electricity supply to renewables.

Focussing the attention on wind energy, it is interesting to see that this form of renewable energy has the potential to supply the global energy demand on its own [3, 60]. Global practical wind power is abundant and spatially distributed. Practical wind power locations, which are areas that meet all practical requirements for wind installations (sufficient wind, low elevation or water depth and compatible land use, with all system losses included), cover 30% of all land and near-shore areas outside of polar regions worldwide [4]. The potential of wind energy is known and has been exploited by mankind for many years. The wind has helped many ships sail around the world. Wind mills have ground grain and pumped water for many centuries. The first windmill to generate electric power arose in 1887, built by Prof. James Blyth of the Anderson's College Figure 1.1a shows Charles Brush' wind turbine, which was operated from 1886 until 1900, had a rotor 17 m in diameter, mounted on a 18 m tower and produced about 12 kW [20]. Figure 1.1b shows the Vestas V164. It is currently the world's most powerful turbine and has a power of 8 MW. It came online in January 2014. The first machine has been installed for testing at the Danish national wind turbine test centre at Osterild. It has a tower height of 140 m and 80 m long blades and a lightweight nacelle [81].

The problem with wind energy and most other renewable energy sources is that only a fraction of the huge potential can be harvested with current technologies and they need to rely on political or economic measures to reach the set goals.



(a) Charles Brush' wind turbine [20].



(b) Modern wind turbine [81].

Figure 1.1: Conventional wind turbines.

Today's wind turbines are more efficient than those from the 19th and beginning of the 20th century, but still operate at a height of only about 150 m, where wind flows are weaker and more variable than on higher altitudes. Even to reach these heights, they require a large construction due to the following reasons:

- A high tower is needed to exploit wind at higher altitudes, where it is stronger and more consistent.
- This tower needs to withstand a large bending moment caused by the force on the rotor, so it must be strong and have a good foundation.
- The turbine blades work like a wing. The force on a blade section scales quadratically with the effective wind speed as observed from this moving section. The outermost part of the rotating blades has the highest true wind speed and thus is most efficient. The inner part of the blades serves mostly to support the outer part.

A new method for harvesting wind energy that does not suffer from these issues is first proposed in [70] and is known as '*Airborne Wind Energy*'. The concept uses only the outer, most efficient part of a wind turbine, a tether, a generator and – compared to conventional wind turbines – a small base to start up the system. This lowers the amount of construction material needed and investment cost. The outer part of the wind turbine rotor is replaced by a kite, which can be either rigid or flexible, that flies in a crosswind direction. There are several possibilities to generate electricity with an AWE system. The two most important possibilities are listed here:

- In one option, the generator is ground based and connected to a winch that holds the tether. During the power generating phase, electricity is produced by flying the kite at a high speed in a crosswind direction, thus generating a high lift force and consequently a high traction force on the tether. By unrolling the tether, the ground based generator produces electricity. At the end of the power generating phase, when the tether is fully unrolled, the power consumption phase starts. During this phase, the kite is flown to generate a traction force as small as possible while still exerting a tensile force on the tether. Now the tether can easily be reeled in. Over the two phases combined, net electricity is produced. This cycle is known as the '*pumping cycle*'.
- In another option, the generators are on board of the aeroplane. These are driven by inverted propellers. These inverted propellers are driven by the true wind speed of the kite, which flies at a high altitude in a crosswind direction. The high cross-wind speeds result in the turbines

spinning the generators at high speeds. The energy is transferred to the ground through the electrical tether. This possibility has the advantage that there is no power consumption phase. This possibility is known as '*airborne wind turbines*'.

The airborne part can either be a soft, flexible wing such as a surfing kite or a rigid wing similar to an aeroplane. Compared to soft wings, rigid wings are easier to model and control. Modelling of soft kites involves complex multibody system dynamics with a lot of degrees of freedom [11] while a rigid kite can be modelled as a single body with a typical aeroplane model for the aerodynamics.

Unfortunately the benefits of airborne wind energy come at a cost. While a wind turbine only needs to be aimed towards the wind to operate, an AWE system needs to be constantly controlled to fly a certain crosswind trajectory. For this reason, AWE systems need an automatic control system [58, 14, 34], which in turn needs a reliable estimate of the system state.

## 1.2 Performance of an AWE system

Miles Loyd [70] is the first to derive a formula for the performance of a crosswind flying kite. The theoretical power such a system could deliver is given by:

$$P = \frac{4}{27} \frac{\rho v_w^3 A}{2} \frac{C_L^3}{C_D^2}, \quad (1.1)$$

with  $\rho$  the air density,  $v_w$  the wind speed,  $A$  the wing area of the kite and  $C_L$  and  $C_D$  the aerodynamic lift and drag coefficient of the system<sup>1</sup>. Dividing this theoretical power by the total available power in the wind passing through a unit area,  $P_w = \frac{\rho}{2} v_w^3$  and the surface area of the kite  $A$ , gives a performance factor

$$\zeta = \frac{4}{27} \frac{C_L^3}{C_D^2}. \quad (1.2)$$

The nondimensional performance metric  $\zeta$  is the amount of power a system can generate, as a multiple of the power which flows through a region with equal area to the wing. It is interesting to compare the power harvesting factor with the Betz limit, which limits the power that can be extracted from a given cross sectional area of the wind field. The Betz limit is given by  $\frac{16}{27}$ . For a wind turbine, the relation between the Betz limit and the  $\zeta$ -factor is the ratio

---

<sup>1</sup>The lift and drag coefficients are dimensionless coefficients representative for the lift and drag force of an aeroplane, the components of the aerodynamic force perpendicular and parallel to the relative wind velocity respectively.

between the surface area of the wind turbine blades and the swept area [92, 25]. Due to the higher lift and lower drag coefficients of rigid kites compared to soft kites [92], Equation (1.2) gives performance factors that are about 10 times higher for rigid kite systems compared to soft kite systems. This means that to get the same power output from a soft kite, about 10 times the surface area is needed of the equivalent hard kite.

Makani Power reports a total  $C_L$  of 1.7 and a total  $C_D$  of 0.25 for their ‘Wing 7’ prototype with a rated power of 20 kW, resulting in a  $\zeta$ -factor of 11.6 [92]. This results in a power of approximately 7.1 kW per square meter at a wind speed of  $10 \frac{\text{m}}{\text{s}}$ . The Vestas V164, the currently largest wind turbine, produces about 5 MW at a wind speed of  $10 \frac{\text{m}}{\text{s}}$ . Each blade has a surface area of approximately  $200 \text{ m}^2$  [73] resulting in a power of 4 kW per square meter and an equivalent  $\zeta$ -factor of 6.7. Larger airborne wind turbines have a higher  $\zeta$ -factor because the portion of the tether drag and the induced drag is lower for larger systems. A reduction of the drag by 20%, which can be expected from a multi-megawatt system, results in a  $\zeta$ -factor of 18.2. This means that such a system with a wing with the same size of one blade of the Vestas V164 produces the same amount of power as the complete turbine.

A large portion of the total drag coefficient of the system in Equation (1.2) is due to the tether drag. This is mainly true for smaller systems. For larger systems, the tether strength scales with the square of the tether diameter, while the drag only grows linearly with the tether diameter. As mentioned above, Makani Power reports a total  $C_D$  of about 0.25 for their Wing 7. This is the sum of a parasitic drag of 0.06, induced drag of 0.08 (assuming a low span efficiency of 0.7) and a tether drag of 0.11. The same system without tether drag would more than triple its  $\zeta$ -factor and thus efficiency, to about 36. Of course any AWE system always has some tether drag, but a way to reduce it uses two aeroplanes connected with two shorter tethers to one main tether and is known as ‘*balanced kites*’. Figure 1.2 gives a graphical impression of a balanced kites system. In a balanced kites system, two aeroplanes fly crosswind circles around each other. The two shorter tethers move at a high velocity and generate tether drag, but the long, main tether is close to stationary and creates almost no tether drag. A parametric study is done in [99] on the average generated power of a single aeroplane system compared to a balanced kites system in function of wing area. Both systems have the same total wing area and use on-board propellers to generate electricity, as is done in the Makani Power system. The balanced kites systems in this study thus consist of two aeroplanes with half the wing area of that of the single kites system. The average generated power for both the single kite and balanced kites systems is shown in Figure 1.3a and the ratio between the average generated power of a single kite system and a balanced kites system is shown in Figure 1.3b.

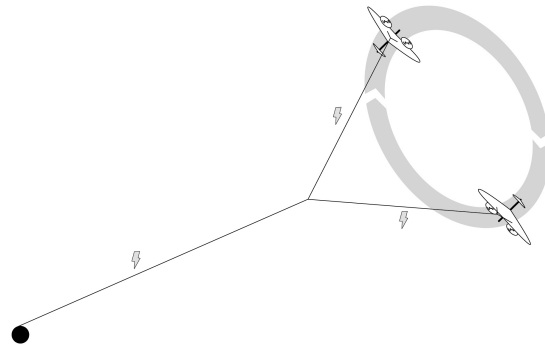
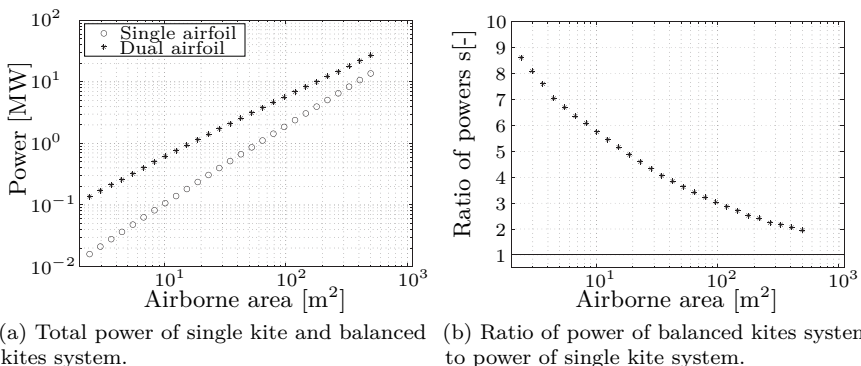


Figure 1.2: Graphical impression of a balanced kites system. Illustrated by R. Paelinck.



(a) Total power of single kite and balanced kites system. (b) Ratio of power of balanced kites system to power of single kite system.

Figure 1.3: Average power output as a function of wing surface of a balanced kites system compared to a single kite system for aeroplanes with a gliding ratio of 25 at a reference wind speed of  $10 \frac{\text{m}}{\text{s}}$  [99].

From Figure 1.3a, we see that for relatively small systems of e.g.  $10 \text{ m}^2$ , a power of about  $0.6 \text{ MW}$  can be obtained with a balanced kites system, which is 6 times more than what can be achieved with a single kite system. A grid scale system of  $100 \text{ m}^2$  can generate a power of approximately  $6 \text{ MW}$ , which is still 3 times more than what a single kite system of the same size can produce. Note that the values for a real-life system may be different from the ones presented in [99], but it does show the significant advantages a balanced kites system can provide.

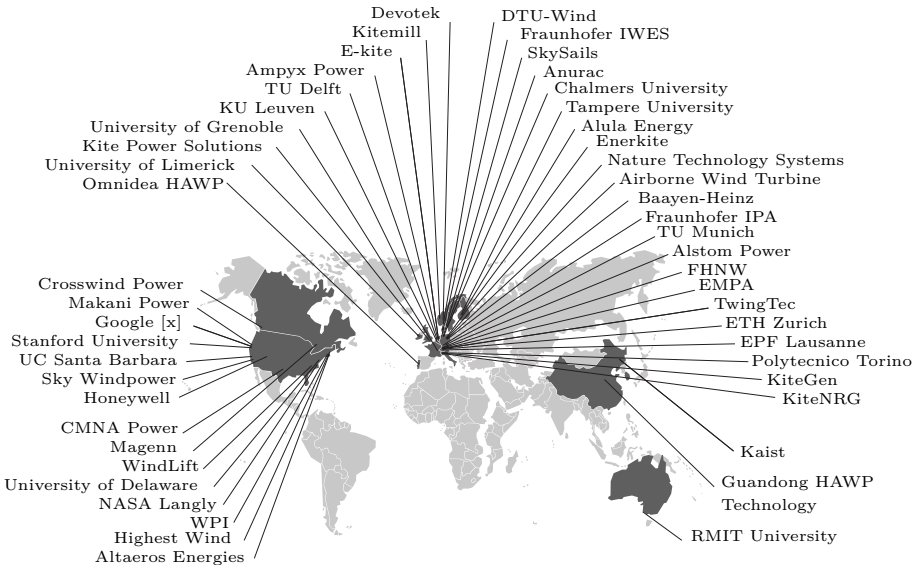


Figure 1.4: Airborne wind energy research and development activities by country and by team. Countries with academic or commercial activities in 2013 are coloured in dark grey [25].

### 1.3 Existing AWE prototypes

Inspired by the huge potential of airborne wind energy, several academic and commercial groups have been developing AWE systems and building working prototypes. Figure 1.4 maps the worldwide commercial and academic research and development activities on Airborne Wind Energy in 2013 [25]. The different groups can be split into two classes: groups who follow Loyd's paper and use crosswind flying kites to harvest the wind energy to produce electricity and groups that are developing different strategies.

In the first group, two main distinctions can be made between the different teams: teams that use hard kites versus teams that use soft kites and teams that do on-board generation versus teams that do ground-based generation.

Even though the  $\zeta$ -factor that is discussed in Section 1.2 for flexible kites is approximately an order of magnitude lower than that of hard kites, many groups are developing these kinds of systems. Compared to hard kites, they may be competitive due to a lower cost per square meter of wing area. They are also somewhat safer to operate and in the event of a crash, there is a chance the kite



(a) SkySails power system [87].



(b) KitePower system of TU Delft [91].



(c) EnerKite EK30 mobile demonstrator [30].



(d) KiteGen system [64].

Figure 1.5: AWE systems using soft kites.

is reusable. Some groups that are developing AWE systems using soft kites are the German company Skysails, TU Delft, the SwissKitePower team at FHNW and ETH Zurich, KiteGen at Polytechnico Torino, UC Santa Barbara and the University of Limerick. Some of these systems are shown in Figure 1.5

Perhaps commercially the most successful company is Skysails [86]. For several years they have been using flexible kites for towing large mercantile ships, with several installations on ships worldwide. They achieve a reduction of fuel consumption of about 30%. They are working on using their system for electricity production, shown in Figure 1.5a. Their system is similar to that of TU Delft, shown in Figure 1.5b. Both the systems of TU Delft and SkySails use a single main tether leaving the ground station that connects to an airborne



(a) In flight footage of Ampyx Power's '*Power Plane*'[1, 82].

(b) Makani Power's '*Wing 7*' [71].

Figure 1.6: AWE systems using hard kites.

control pod. From this control pod the steering lines go out to the kite. The control pod has servo motors on-board to vary the length of the steering lines to control the kite. The system of EnerKite and KiteGen, shown in Figure 1.5c and Figure 1.5d respectively, use multiple lines leaving the ground station to control the kite, having a lower airborne weight but more tether drag and the need to control the difference in line lengths with the heavy generators.

Systems that use hard kites are fewer, perhaps because of the higher investment needed to develop the airborne system. Two companies that are developing a hard kite AWE system are Ampyx Power and Makani Power. Their systems are shown in Figure 1.6. The system of Ampyx Power falls within the same category as the system developed in this thesis, a hard kite using the pumping cycle to generate electricity [82]. The system of Makani Power on the other hand uses on-board generators driven by propellers [92].

Other types of systems are shown in Figure 1.7. They include lighter-than-air systems illustrated in Figure 1.7a and Figure 1.7b. Lighter-than-air systems combine aerostatic and aerodynamic lift to keep the system aloft. They use a duct surrounding a wind turbine. In the system in Figure 1.7a, the duct is shaped a bit like a wing such that it not only provides aerostatic lift, or buoyancy, but also aerodynamic lift by the wind flowing over the duct. This decreases the '*blowdown*' of the system, which is the result of the aerodynamic drag on the system pulling it downwind and towards the ground. A system utilising the Magnus effect<sup>2</sup> to produce aerodynamic lift is shown in Figure 1.7c. A cylinder rotates about a horizontal axis transverse to the wind, producing a high force on the cable that connects the system to the ground. It performs a pumping motion to produce electricity.

<sup>2</sup>The Magnus effect is the effect in which a spinning ball or cylinder curves away from its principal flight path. It is responsible for the curve of a served tennis ball or a driven golf ball.



(a) System with wing-shaped duct [93].



(b) System relying solely on aerostatic lift [93].



(c) AWE system using the Magnus effect [77].



(d) Kite-Powered Water Pump during field testing [74].

Figure 1.7: Lighter-than-air systems and kite-powered water pump.

An interesting, humanitarian project is presented in [74]. They are developing a kite-powered water pump that can be used in developing countries. A very stable kite periodically moves a rocking arm up and down. This rocking arm is connected to a water pump that pumps up ground water.

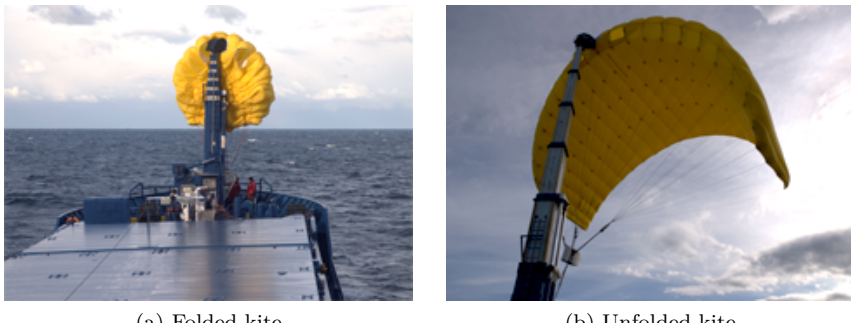


Figure 1.8: Skysails kite during launch [86].

## 1.4 Launch methods for AWE systems

For an AWE system to become operational, the kite first needs to be launched. Wind speeds are generally too low near the earth's surface to generate sufficient lift on the wing while the kite is stationary. Several projects all over the world use different approaches to harvest the high altitude winds. Depending on the type of system used, ranging from on-board or ground based power generation and rigid versus flexible kites, they differ in their launch and recovery possibilities.

The launching system of Skysails' ship propulsion system has a telescopic mast which lifts the kite by the leading edge to a certain height where the wind inflates and unfolds the kite to its full size, see Figure 1.8. The mast releases the kite by prolonging the towing rope that connects the leading edge of the kite to the mast. The wind at sea is strong and steady enough to lift the kite to its operating altitude, where it begins following a figure-eight trajectory to provide the traction force. For recovery, the kite flies into a steady position directly above the mast and the towing rope is reeled in until the kite is connected to the mast again.

KiteGen has proposed using two heavy duty air blowers to create artificial wind, see Figure 1.9. These blowers have two rotational degrees of freedom such that they can be actively aimed towards the flexible kite that hangs down from a tall mast [64].

A piggy-back chin docking of the flexible kite on an aerostat is proposed and tested in [10]. They propose to use a sort of zeppelin to lift the kite to its operational altitude where it is released. A benefit of this system is that it



(a) Blowers aimed towards kite. (b) Kite launched and flying crosswind.

Figure 1.9: Kitegen system using air blowers to launch the kite [64].



(a) Lighter than air zeppelin lifting kite. (b) Kite lifted to flying altitude.

Figure 1.10: Piggy-back chin docking of flexible kite on an aerostat [10].

possible to launch the flexible kite in zero-wind conditions. A downside is that heavy material wear is observed during their initial testing. Furthermore it used Helium to fill the blimp, which is expensive and impractical in its use. TU Delft also developed an upside-down launch style, similar to that of KiteGen [83].

A separate power generation and lift generation system is proposed in [97]. The lift system is lighter than air with lateral and longitudinal control. The power generating turbine is supported by this lifting system but it is totally independent, see Figure 1.11.

Other lighter-than-air systems are discussed in [93]. In these systems, the aerostatic lift helps launching the system when it is on the ground and keeping it aloft. They can easily be launched by prolonging the tether with which they are connected to the ground.

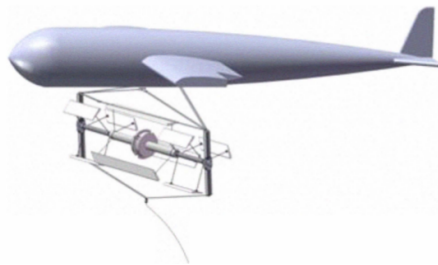
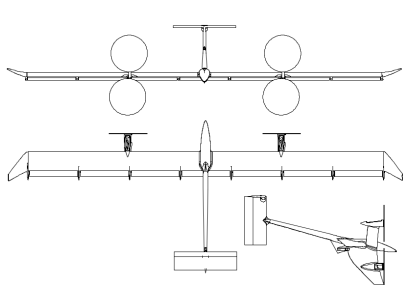


Figure 1.11: Lighter than air system supporting power generating turbine [97].



(a) Schematic representation of Makani Power aeroplane.



(b) Operational picture of Makani Power aeroplane.

Figure 1.12: The AWE system of Makani Power.

Makani Power, which is acquired by Google in 2013, develops an on-board power generating system. During launch and recovery the on-board turbines are used as propellers and the generators are operated as motors. Power is supplied to these motor from the ground via the conducting tether. This proposed system can be manoeuvred like a quadcopter to its operating zone [92]. [65] proposes a similar system. Figure 1.12 gives a schematic and picture of the Makani Power system.

We propose a novel approach for launch and recovery of rigid wing tethered aeroplanes, namely the rotation start, which is discussed in more detail in Section 1.5.

## 1.5 The rotation start

In the rotation start, an arm rotating about a central shaft brings the tethered aeroplane up to speed generating wind flow over the wing. Rotational forces keep the tether tension and ground clearance. Once passed the take-off speed of the aeroplane, the tether is reeled out allowing the aeroplane to gain altitude while being towed by the arm. Recovery of the aeroplane is done in a reverse order. The rotational start-up acts like a ground based propulsion. This eliminates the need for an on-board propulsion system for take-off and is particularly suited for a system consisting of rigid wings performing the pumping cycle, since for this kind of system no on-board propellers are needed.

A schematic representation of the rotation start is shown in Figure 1.13 as a top- and side-view.  $F_L$  and  $F_D$  are the aerodynamic lift and drag force of the aeroplane respectively,  $F_i$  is the rotational force,  $F_C$  is the force from the cable and  $L$  and  $r$  are the arm and tether length respectively. Due to the lag angle of the aeroplane with respect to the arm, defined as  $\phi$  in Figure 1.13, the arm performs work on the aeroplane allowing the aeroplane to overcome drag and gain energy. A scale analysis of the rotational start in zero-wind conditions can be performed with the help of Figure 1.13 [45]. In the depicted set-up an aeroplane is being towed around the main shaft. The centre of mass is at arm-level and for this analysis, we select an arbitrarily angle of  $45^\circ$  for the wings to make with the ground. The gravity of the aeroplane  $mg$  is balanced by the vertical component of the lift force  $F_L$  of the aeroplane:  $mg = F_L \cos(45^\circ)$ . The lift force equals  $F_L = \frac{1}{2}\rho v^2 A C_L$  in which  $\rho$  is the density of air,  $v$  is the speed of the aeroplane relative to the air,  $A$  is the surface area of the wings of the aeroplane and  $C_L$  is the lift coefficient of the aeroplane. This leads to a required nominal speed of

$$v = 2^{\frac{3}{4}} \sqrt{\frac{mg}{\rho A C_L}}. \quad (1.3)$$

This is effectively the take-off speed for the aeroplane at a  $45^\circ$  angle. Referring to Figure 1.13 the following can be formulated:

$$\begin{aligned} d^2 &= L^2 + 2 \cos(\phi) r L + r^2, && \text{cosine rule} \\ \sin(\psi) &= \sin(\phi) \frac{L}{d}, && \text{sine rule} \\ F_i &= m \frac{v^2}{d}, && \text{inertial force} \\ F_L &= A C_L \rho \frac{v^2}{2}, && \text{lift force} \\ F_D &= A C_D \rho \frac{v^2}{2}, && \text{drag force} \\ \tan(\psi) &= F_D / (F_i + \frac{F_L}{\sqrt{2}}). \end{aligned} \quad (1.4)$$

The above set can be seen to define a function  $\phi = f(\rho, A, C_D, C_L, m, r, L)$ , independent of  $v$ .  $\phi$  is a measure of how easy it is to tow the aeroplane. In the

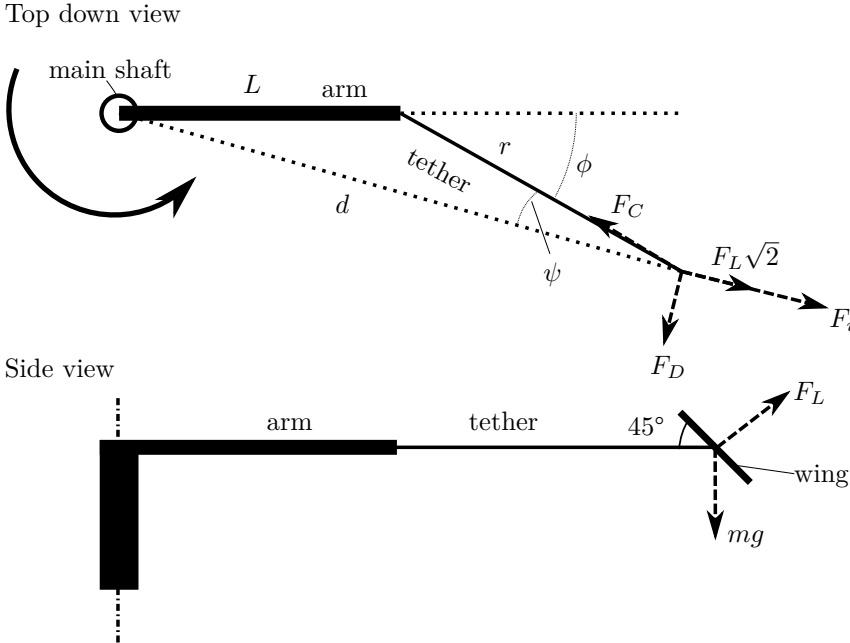


Figure 1.13: A schematic top view of the arm towing the aeroplane [45].

limit of  $\theta = 0$  the tether cannot deliver a force component to balance the drag force. Assuming that  $r > L$ , this situation happens for  $\phi = 0$  and  $\phi = 180^\circ$ .

Applying the Buckingham pi theorem for base units ( $L$  and  $m$ ) allows rewriting  $f$  in terms of dimensionless parameters  $\psi = g(C_L, C_D, L/r, A/r^2, \rho r^3/m)$ . This promises the existence of a limiting expression for  $L/r$ . Expanding the last equation of Equation (1.4), taking the first order Taylor series for  $L \rightarrow 0$  and choosing  $\hat{\phi} = \pi$ , which is the limit where towing the aeroplane by an arm becomes infeasible, gives:

$$\frac{r}{L} = \frac{r^2 C_L^2 A^2 \rho^2 - 8m^2}{C_D r^2 C_L A^2 \rho^2 \sqrt{2} - 4C_D m r A \rho}. \quad (1.5)$$

Taking the limit for  $r \rightarrow \infty$  towing gets more difficult with increasing tether length  $r$  and decreasing glide ratio  $C_L/C_D$ :

$$\frac{r}{L} \propto \frac{C_L}{C_D}. \quad (1.6)$$

It is observed that to power an aeroplane with long tethers, the length of the arm should also be increased.

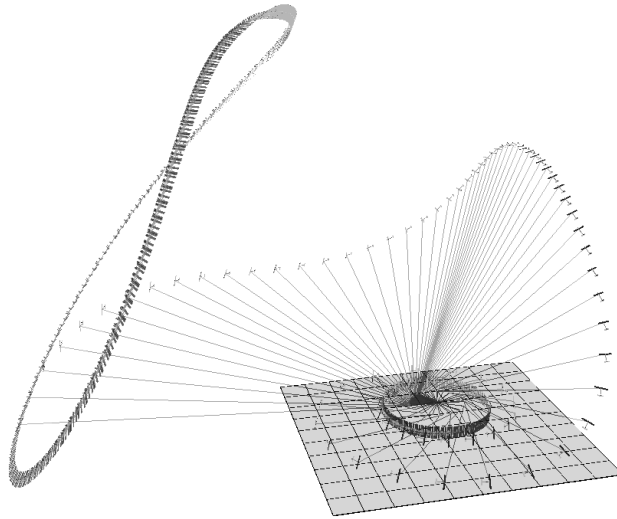
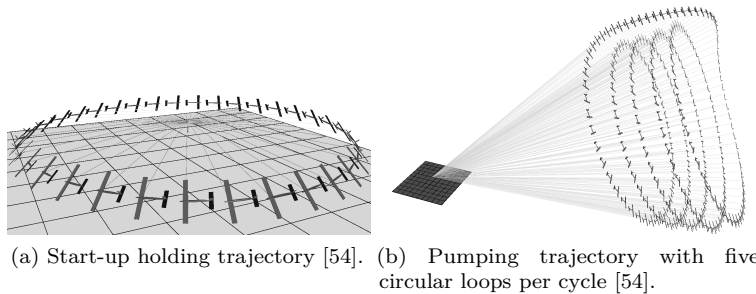


Figure 1.14: Transition trajectory for rotation start [54].



(a) Start-up holding trajectory [54]. (b) Pumping trajectory with five circular loops per cycle [54].

Figure 1.15: Example of a start-up and crosswind trajectory.

An example of a possible start-up trajectory can be found in [54] and is shown in Figure 1.14. It is the transition between a holding trajectory in which the aeroplane is flying a periodic, circular trajectory shown in Figure 1.15a and a power generating pumping cycle, of which an example is shown in Figure 1.15b. In this specific trajectory, the kite first gains altitude when it is flying against the wind. The aeroplane then comes down and gains speed when flying with the wind to make the transition to the power generating trajectory.

## 1.6 Objective and contributions of the thesis

### Thesis objective

This thesis is part of the ERC Highwind project (Project reference 259166) [31]. The main goals of the Highwind project are mathematical modelling, computer simulation and optimisation studies for AWE systems, accompanied by small scale experiments for model and control system validation. The project distinguishes four work packages:

- WP1: Mathematical modelling of aeroplane and tether
- WP2: Optimal control and stability optimisation
- WP3: Embedded control algorithms
- WP4: Small scale experiments

At the end of the project, a small scale, automatically flying prototype shall be realised, accompanied by validated and scalable mathematical models and a toolbox of efficient computational methods for simulation and multidisciplinary optimisation of high altitude wind power systems. If successful, the project will help to establish this new type of wind power generator that may provide electricity more cheaply than fossil fuels and is deployable at considerably more sites than conventional windmills. The Highwind project thus simultaneously pushes forward the state-of-the-art in development and applications of mathematical modelling, simulation and optimisation tools and promotes a technology that helps to significantly reduce carbon dioxide emissions worldwide. The choice is made in the project to use rigid kites because they are easier to model and because of their higher power output per wing area, which means a smaller aeroplane can be used which has the same power output of a larger, soft wing system. Furthermore the choice is made to use the pumping cycle such that the airborne part of the setup can be kept relatively light and inexpensive.

This thesis focuses on WP3 and WP4. Within WP4, this thesis presents the development of experimental test set-ups on which small scale experiments can be carried out to experimentally validate the algorithms developed within the Highwind project. Within WP3, this thesis presents the development of estimation methods to reliably estimate the position and orientation of the aeroplane.

## Main contributions

- The continued development of the indoors experimental test set-up, including improvements to the stereo vision system by the installation of new cameras, the addition of an IMU and on-board electronics to the aeroplane, the installation of a small winch on top of the carousel and the development and implementation of the software system.
- A theoretical design of a balanced-kites set-up, which forms the basis for the design and development of the outdoors single kite test set-up. The outdoors set-up will be used to perform outdoors flight experiments with larger aeroplanes. This set-up consists of a carousel and winch, which are designed in detail and realised.
- The development of a moving horizon estimator based on a kinematic model that fuses measurements of the aeroplane's acceleration and angular velocity with measurements of the stereo vision system consisting of two cameras observing three markers on the aeroplane. The developed estimator is robust against faulty detections of the marker positions in the camera images.
- The development of a moving horizon estimator based on a dynamic model of the system that offers a better estimation performance than an estimator based on a kinematic model and a comparison of the developed estimation approach with traditional methods.
- The development of an alternative to dead reckoning. In dead reckoning, measurements of acceleration and angular velocity of the aeroplane are kinematically integrated to provide state estimates at a high frequency. The proposed approach uses a dynamic model of the system and uses moving horizon estimation. It gives a better estimation performance than dead reckoning for long prediction times.
- The presentation of closed-loop control experiments, in which the optimisation based estimation and control algorithms developed in this thesis are applied on the indoors test set-up.

## 1.7 Thesis outline

This thesis is split into two parts. The development of the experimental set-ups is discussed in Part I. Part II of this thesis discusses estimation algorithms that can be used to estimate the position and orientation of the aeroplane which are required to control the aeroplane.

In Part I, Chapter 2 gives a description of the indoors set-up that is partly developed during the master thesis of K. Geelen and J. Gillis [45]. Chapter 3 outlines the development of the outdoors carousel that is partly developed in collaboration with M. Clinckemaillie, J. Stuys and W. Vandermeulen during their master theses [16, 88]. First the requirements the set-up has to meet are given. Then a design for a balanced kites set-up is proposed which forms the basis for the design of the single kite set-up that is designed in detail and built.

In Part II, Chapter 4 presents estimation techniques used in the subsequent chapters. First, the full information filter is discussed, followed by an overview of the Kalman filter and some of its nonlinear variations such as the extended and unscented Kalman filter. Next, moving horizon estimation is presented as an estimation technique to better handle nonlinear models that can be implemented in the ACADO Code Generation Tool. Chapter 5 presents a moving horizon estimator that fuses all available measurements using a kinematic model which does not consider the causes of motion of the aeroplane. Robustness against outliers in the measurements is obtained using appropriate penalty functions. Chapter 6 presents a moving horizon estimator based on a dynamic model of the system which does take into account the causes of motion of the aeroplane and does a comparative study with the kinematic approach and with other estimation techniques, based both on simulations and experimental data. An alternative to dead reckoning is presented in this chapter, an approach in which measurements of acceleration and angular velocity are kinematically integrated to provide fast updates of the state. The proposed approach uses a moving horizon estimator to combine the acceleration and angular velocity measurements with a dynamic model and is shown to improve the estimation performance for long prediction times when compared to dead reckoning. Control experiments performed on the indoors carousel using a simplified version of the developed moving horizon estimator and model predictive control show it is possible to perform closed-loop control experiments on the indoors set-up.

## **Part I**

# **Test devices for AWE**



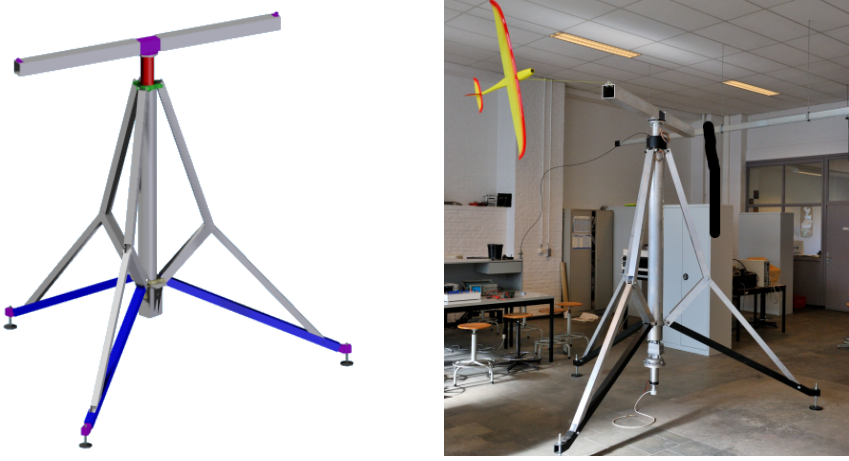
# Chapter 2

## Description of the indoors test set-up

### 2.1 Introduction

The aim of this chapter is to outline the design and development of the indoors set-up. The indoors experimental test set-up is designed and built in [45]. The goal of the indoors set-up is to perform the first phase of the rotation start of a tethered aeroplane. Developed estimation and control strategies can be tested and validated on this set-up. It is not the purpose of the set-up to perform the complete pumping cycle and generate electricity using the pumping cycle, which is not possible indoors. One of the advantages of a rotational start-up is that only limited space is required to speed up the aeroplane to high velocities. This allows the experiments to be done indoors, in a controlled environment, without wind disturbances and at any time, independent of the weather conditions.

The set-up consists of a carousel that rotates the aeroplane. The design of the carousel is discussed in Section 2.2. A small winch that is capable of controlling the tether length is discussed in Section 2.3. Section 2.4 discusses the aeroplane that is used for the indoors experiments. The measurement system that is developed for this set-up is outlined in Section 2.5. The purpose of the measurement system is to provide measurements that allow estimating the position and orientation of the aeroplane which are needed to control the aeroplane. The data acquisition system that collects the data of all sensors is discussed in Section 2.6. The underlying software architecture is described in Section 2.7. The software provides a component based framework in which the



(a) Carousel design.

(b) Carousel realisation.

Figure 2.1: The final design and realisation of the carousel.

measurements can be retrieved and developed algorithms can be implemented. Section 2.8 concludes the chapter.

## 2.2 Carousel design

The most significant part determining the general layout of the test platform is the mechanical structure of the carousel. Its purpose is to perform the rotation start by rotating the arm to which the aeroplane is attached. The final design and realisation is shown in Figure 2.1. It consists of a central axis that is supported by three legs. On top of the central axis is the arm that tows the aeroplane. The arm is symmetrical to keep the system balanced. Most parts are standard aluminium bars which are available off-the-shelf. The carousel is designed for high stiffness, such that the forces on the aeroplane have minimum influence on the structure of the carousel. The design force is 800 N exerted on the end of the arm in a direction perpendicular to the arm. The axis is supported by two bearings, one at the top and one at the bottom. The three legs have a kink in the outer bar such that there is more room for the hanging aeroplane compared to when it would be one straight bar. This construction with two smaller triangles also creates a more rigid construction compared to a construction with only one large triangle for each leg.

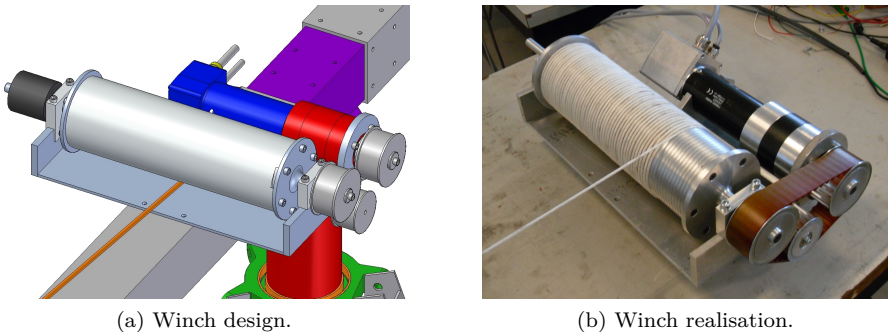


Figure 2.2: The final design and realisation of the winch.

The available indoor space is  $81 \text{ m}^2$  and it is enclosed by nets for safety reasons. This space limits the arm length to be 1 m. The carousel is designed with a provision to increase the arm length and hence increase the towing length of the tether, as shown in Section 1.5. The height of the room is 4 m. The height of the set-up is chosen to be 2.5 m, allowing both ground and ceiling clearance for the aeroplane. The carousel is driven by an Electrocraft S-19 3 motor controlled by an E-motion DA4709 controller. It has a nominal power of 300 W at a nominal speed of 3000 rpm. A gearbox with a reduction of 32.8:1 from Bonfiglioli converts this to a nominal rotation speed of 90 rpm. A vibrational analysis in [45] revealed the first eigenmode to be a torsion mode of the central axis at a frequency of about 16 Hz, which is ten times higher than the rotation frequency, so no excitation problems are expected from this mode.

## 2.3 Winch and tether

A winch to control the tether length is designed and built in [17] and is placed on the top centre of the carousel. Its function is not to generate power using the pumping cycle since this is not possible indoors, but merely to allow experiments with different and varying tether lengths. The function of the tether is to connect the aeroplane to the carousel and to transmit power and communication signals to the aeroplane. Figure 2.2 shows the design and realisation of the winch. The winch is powered by an EC 60 brushless DC 400 W motor from Maxon Motor. The maximum reel-in/out speed is  $5 \frac{\text{m}}{\text{s}}$  at a tether force of 80 N. The tether is guided on the drum by grooves in the drum hull.

The tether used in this AWE setup contains 3 pairs of insulated copper wires.

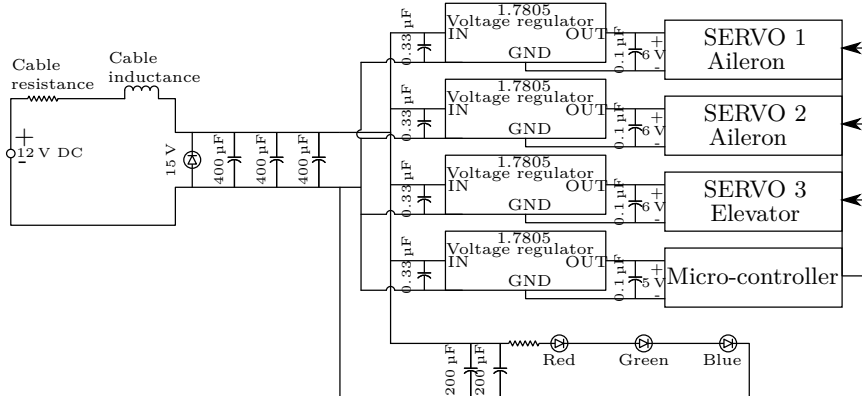


Figure 2.3: Cable interaction and on-board power electronics [47].

Two pairs are used for the communication between the micro-controller inside the aeroplane and the ground computer. The third pair is used to provide 12 V DC at maximum 5 A. The copper pairs are enclosed in a sheath of braided Kevlar that takes the mechanical tension. It has a tensile strength of about 1600 N which is more than sufficient to take the loads of the aeroplane. The outer diameter of the cable is 3.6 mm.

## 2.4 Aeroplane

The aeroplane that is used for the experiments is a standard model aircraft called the Ariane P5. It has a wingspan of 1 m, a surface area of  $0.1 \text{ m}^2$  and a mass of 0.6 kg when fully equipped with all sensors and actuators. It has a carbon fibre reinforced composite structure, such that it can withstand the high wing loadings due to rotational and aerodynamic forces. This aeroplane has ailerons to control the lateral dynamics and an elevator to control the longitudinal dynamics [76]. The angles of the control surfaces are controlled by KDS N300 metal gear digital servo motors that deliver a maximum torque of 0.3 N m and a speed of 0.06 s/60°.

Due to space limitations inside the plane and the need to deal with a voltage drop in the tether, a custom on-board power distribution circuit is used to power the on-board instrumentation. Four linear regulators are used for stepping down the voltage from 12 V to 6 V and 5 V respectively. A bank of capacitors with a total capacitance of  $1600 \mu\text{F}$  is used to handle current load spikes when all servos are actuated concurrently, see Figure 2.3.



Figure 2.4: Analog Devices ADIS16367 IMU.

## 2.5 Measurement system

To be able to do closed-loop control of the aeroplane, measurements are needed that allow estimating the position and orientation of the aeroplane. An IMU is typically used in unmanned aeroplanes to provide measurements of the acceleration and angular velocity of the aeroplane at a high sampling frequency. The measurements of an IMU are '*relative measurements*', meaning they are only useful in combination with a previous estimate of the position and orientation. On their own, the position and orientation estimates provided by IMU measurements drift due to the integration of noisy signals. An IMU is therefore typically accompanied with a measurement system that provides '*absolute measurements*' of the position and possibly also of the orientation. A stereo vision system is developed for this purpose in [45].

To measure the angle of the carousel, an incremental encoder with a resolution of 2048 ticks per revolution is mounted on the motor. Combined with the reduction ratio of the gearbox of 32.8, this results in a resolution of  $0.005^\circ$ , which is more than sufficient.

Stringent selection criteria for the selection of the IMU are the reach of the accelerometer, accelerations of up to 18 g, the reach of the gyroscopes, rotation speeds of up to  $540 \frac{^\circ}{s}$ , and the physical dimensions. Many military systems meet these requirements, but there are only a few commercially available IMUs. Two options are listed in Table 2.1. The ADIS16367 from Analog Devices, shown in Figure 2.4, is selected due to its better specifications for bandwidth and sampling frequency, smaller size and lower price. It is mounted inside the fuselage of the aeroplane near the centre of mass.

This IMU is interfaced to a microcontroller (Texas Instruments LM3S9B92) which also controls the servo motors that control the angles of the control surfaces of the aeroplane.

A stereo vision system is developed for the set-up because it has a light weight,

	Unit	Xsens MTX	Analog ADIS16367
Bandwidth	Hz	30	330
Sampling frequency	Hz	512	1200
Interface		RS422	serial
Dimensions	mm	21x38x53	23x32x38
Price	euro	1750	700

Table 2.1: Two available Inertial Measurement Units.

is relatively inexpensive and by using at least 3 markers, it offers measurements of both position and orientation. By placing the cameras on the rotating part of the carousel, the highest velocity component of the aeroplane, the radial velocity, is eliminated. This allows the cameras to have a clear image of the aeroplane, while the surroundings are blurred. The stereo vision system initially consisted of two Unibrain Fire-i digital cameras with a resolution of 640x480 pixels and a maximum frame rate of 15 Hz. These cameras were later updated to two Flea3 cameras from Point Grey with a resolution of 1600x1200 pixels at a maximum frame rate of 15 Hz, offering a higher accuracy and higher quality lenses that better approach the ideal pinhole camera, which is discussed in Section 5.3. They further have the advantage that they have an external hardware trigger, allowing better synchronisation of the images. The cameras observe three coloured markers (red, green and blue LEDs) mounted on the underside of the aeroplane. The markers are mounted as far apart as possible; two markers are placed near the wing tips and the third marker is placed on the tail of the aeroplane. They are detected by means of colour filtering algorithms. Calibration of the cameras is needed to know the intrinsic and extrinsic parameters of the cameras. The intrinsic parameters depend on the focal length, image sensor format, and principal point of the camera and are discussed in more detail in Section 5.3. The extrinsic parameters are the position and orientation of the camera. Calibration is done using a white-black chequerboard with a known position and orientation. By observing the relative size and distortion of the chequerboard squares, the intrinsic and extrinsic parameters can be derived.

Table 2.2 gives an overview of the sensors available on the set-up and their accuracies.

Sensor	Measurement	Unit	Accuracy
Encoder	Carousel angle	°	0.005
IMU	Aeroplane's acceleration	$\frac{\text{m}}{\text{s}^2}$	0.1
	Aeroplane's angular velocity	$\frac{\text{rads}}{\text{s}}$	5
Stereo vision system	Aeroplane's pose	pixels	20

Table 2.2: Sensors on indoors set-up.

## 2.6 Data acquisition system

The function of the data acquisition system is to gather the data from all sensors in a central location such that they can be used by the control system to estimate and control the state of the aeroplane. Central in the data acquisition system is a MXC-6300 fanless computer from ADLink Technologies with an Intel core i7-3610qe processor running at 2.3 GHz. It is mounted at the top of the carousel on the rotating arm. This is done such that the high speed firewire connection of the cameras of the stereo vision system does not need to pass through a slip ring. The carousel encoder, motor controller and external trigger of the cameras are connected to an EtherCAT box which is in turn connected to the central computer. The microcontroller of the aeroplane is connected to this computer via a TCP/IP connection. The winch controller uses a CAN-bus to connect to the central computer.

The data acquisition of the measurements is carried out by an EtherCAT box that connects to the carousel encoder, the motor controller and external trigger of the cameras. This EtherCAT box is connected to the central computer. The cameras, microcontroller and the winch controller are also connected to this computer.

## 2.7 Software

An important part of the test set-up is the software architecture used to control it. The chosen ‘Open Robot Control Software’ (Orocos) Toolchain [12] is an open source software framework for real time control of robotic and mechatronic systems. The key feature of Orocos is the Real-Time Toolkit, a C++ programming framework that is able to provide hard real time data-flow programming. Furthermore, a variety of drivers for common sensors and actuators are available that are pre-packaged as Orocos components. Every sensor, actuator, and algorithm in our system is wrapped in an Orocos component. Each component typically has multiple inputs and outputs, and the

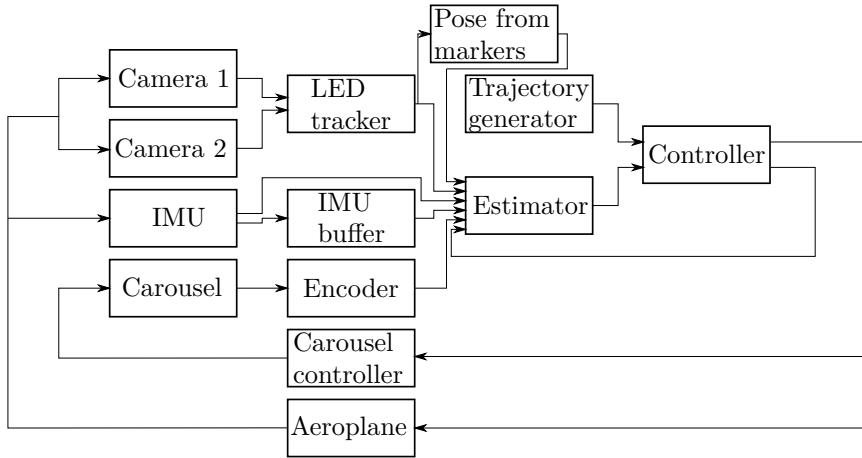


Figure 2.5: Software overview.

components are then linked together at runtime, forming a closed loop system. Figure 2.5 shows the layout of all Orocosp components in the current closed loop system.

The *Camera* components are responsible for triggering the cameras to take an image. At the same time, the *IMU* and the *encoder*, that operate at a higher frequency, are triggered to take a measurement, such that the measurements are synchronised in time. Once the camera images are transferred to the computer, they are processed by the *LEDTracker*, which finds the positions of all LEDs in both images. The *IMU Buffer* component stores the IMU measurements over 1 period and outputs the average at the same sampling rate at which the cameras are running, which is needed for some estimators. The *Pose from markers* component computes the position and orientation (pose) of the aeroplane directly from the marker positions. This pose estimate can be used for initialisation of the state estimator. The task of the *estimator* component is to form an estimate of the state of the aeroplane by combining all measurements. Part II discusses different types of estimators that are possible. The state estimate is passed to the *Controller*, along with the trajectory that we want to track from the *Trajectory generator*. This controller computes the desired control action and passes it to the *aeroplane's* control surfaces and the *Carousel controller* which controls the carousel speed.

Whenever a measurement becomes available, e.g. from the IMU, it is stored internal in the system in arrays that have the appropriate size for the total number of measurements that are expected for the Estimator. As time evolves,

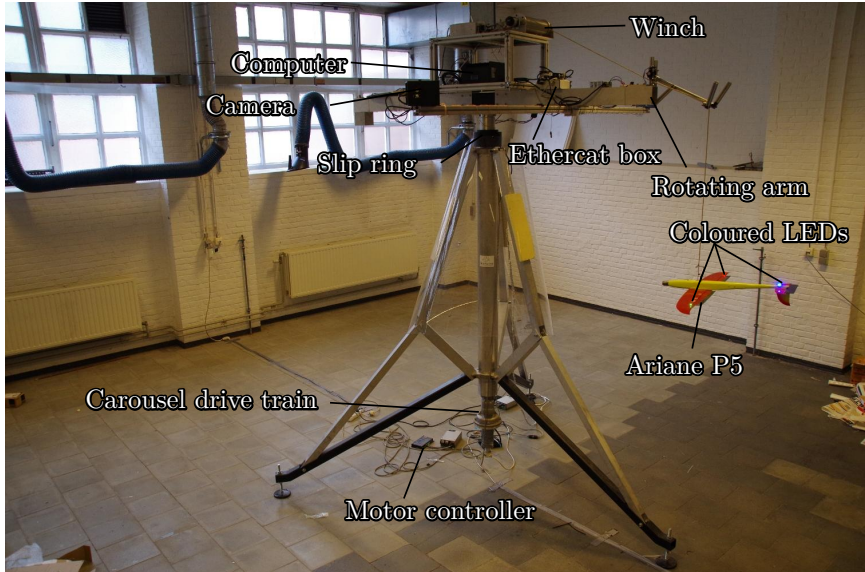


Figure 2.6: The carousel in its current configuration.

these arrays are filled in with all data that arrives. When all data needed by the Estimator is received, the Estimator performs its task. When completed the Estimator sends its state estimate to the Controller that computes the desired control action, which is then applied to the system.

Figure 2.6 gives an overview of the complete indoors set-up with all its components discussed in the previous sections.

## 2.8 Conclusion

This chapter gives an overview of the indoors carousel, a test set-up for rotational start-up for an AWE system, which is designed and built at KU Leuven. It consists of a large aluminium tripod with a 2 m rotating arm at the top. A small winch with a power of 400 W on top of this arm can control the tether length. The aeroplane used on the set-up is the Ariane P5 which has a wing span of 1 m. A custom on-board power-distribution circuit is used to power the on-board instrumentation. This includes servo motors that vary the angles of the aeroplane's control surfaces, three coloured LEDs and an IMU. The IMU measures the acceleration and angular velocity of the aeroplane. The LEDs are used in a stereo vision system that provides measurements of the aeroplane's

position and orientation. A closed loop system is implemented in the Orocosp Toolchain consisting of several components with possibly multiple inputs and outputs working together to control the aeroplane.

# Chapter 3

## Design and development of the outdoors test set-up

### 3.1 Introduction

The aim of this chapter is to outline the design and development of the outdoors set-up. The outdoors set-up is partly developed in collaboration with M. Clinckemaillie, J. Stuyts and W. Vandermeulen during their master theses [16, 88].

The goal of the outdoor set-up is to be able to complete all phases of a power generating cycle, including the launch, pumping cycle and landing. One of the objectives of the ERC Highwind project is the realisation of a balanced kites set-up. Although initially the outdoors set-up will be used to launch a single aeroplane, this intent should be kept in mind during the design of the set-up.

To allow the use of larger aeroplanes, the outdoors set-up is larger and more powerful than the indoors set-up that is outlined in Chapter 2. The motor that drives the rotation of the carousel is more powerful to allow better towing capabilities such that larger aeroplanes can be started. Similarly to allow power generation with larger aeroplanes, the winch motor is more powerful. Larger aeroplanes than the 1 m wingspan Ariane P5 used on the indoors carousel are needed to be able to carry a larger payload, including batteries and sensors needed for crosswind flight, and to be able to produce a meaningful amount of power. Furthermore the outdoors carousel is installed on a mobile platform to allow testing on remote locations.

This chapter is organised as follows: Section 3.2 gives the requirements the outdoors carousel has to meet, Section 3.3 describes the design of the balanced kites set-up which forms the basis of the single kite set-up that is built and is described in Section 3.4. Section 3.5 concludes the chapter.

## 3.2 Requirements

The set-up must be able to perform an automated rotation start of a tethered aeroplane with a wing span of 2-3 m. As is mentioned in Chapter 1, the choice is made to use the pumping cycle to generate electricity to keep the airborne part light and inexpensive. A winch is thus needed on the set-up that is capable of performing the pumping cycle.

To allow future use of the set-up as a balanced kites setup, the carousel has to be able to launch and land two aeroplanes with only small modifications. The main use of the set-up is outdoors. Therefore it has to be weather proof and thus have suitable protection against rain, wind and dust. To be able to perform experiments on remote locations and to allow indoor storage when not in use, the set-up has to be installed on a mobile platform, which may pose some constraints on the design of the set-up. A major focus in the ERC Highwind project is on the automation of the start, crosswind flight and landing. The set-up therefore has to be equipped with the appropriate sensors, actuators and communication systems to control the aeroplane(s), carousel and winch.

During the initial planning of the set-up, the aeroplanes that would be used on the set-up were to have a wingspan of 2 m. Eventually an aeroplane with a wing span of 3 m and a wing area of  $1 \text{ m}^2$  is chosen. The forces the aeroplane exerts on the carousel structure consist of two main forces. During start-up, the rotational forces dominate the behaviour of the aeroplane and during crosswind flight the aerodynamic force dominates. During start-up, it is safe to say the rotational acceleration of the aeroplane does not exceed 20 g, since this already exceeds the range of most accelerometers, and the aeroplane does not survive such high accelerations. With an estimated mass of 5 kg for the fully equipped aeroplane, this amounts to a centrifugal force of about 1000 N. At a maximum flight velocity of  $45 \frac{\text{m}}{\text{s}}$  with a maximum lift coefficient of 1.5, the aerodynamic force the aeroplane can exert on the structure is approximately 1850 N. Since the maximum centrifugal force and the maximum aerodynamic force do not occur at the same time, the carousel does not need to be able to withstand the sum of them. The tether force is highest during crosswind flight. The design force for the mechanical structure is therefore taken at 2000 N.

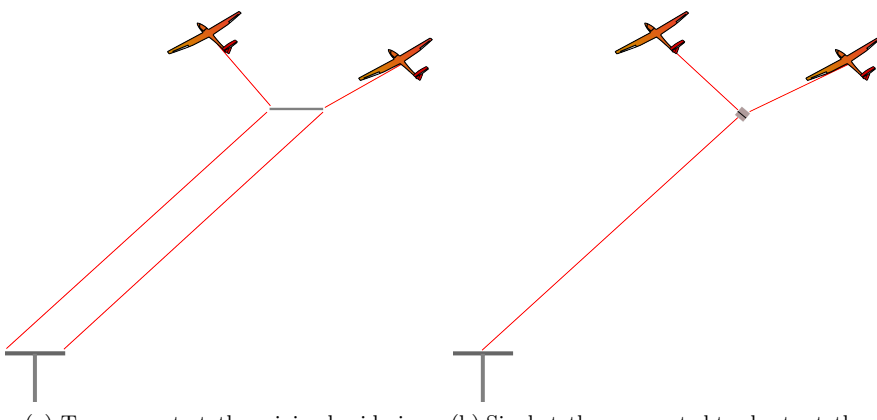


Figure 3.1: Two configurations for the balanced kites set-up [16].

### 3.3 Balanced kites set-up

Although initially the set-up is used to launch a single kite, it may be used to launch balanced kites later in the project. Therefore it is useful to first look at how such a balanced kite set-up may look like. Necessary design decisions can then be incorporated in the design of the single kite set-up such that it can be adapted to launch and land two aeroplanes without major adaptations.

Two possibilities for the balanced kite set-up are considered. One option, displayed in Figure 3.1a, uses a separate tether for each aeroplane which are connected mid-air by an airborne rod and is discussed in Section 3.3.1. The other option, displayed in Figure 3.1b, uses one single tether that is connected to two shorter tethers that go out to both aeroplanes and is discussed in Section 3.3.2.

#### 3.3.1 Double tether

The double tether balanced kites system uses two tethers that go out to both aeroplanes from the carousel and are connected mid-air. They can for example be connected by a simple rod with a clamping mechanism at the end, which is discussed later in this section. The bar is held in place on the carousel during start-up, and when both tethers have reached the desired length, the clamping mechanism is closed and grips the tethers. From this moment on, the rod climbs together with the tethers and serves as the airborne connection between

both tethers. During landing, the tethers are reeled in simultaneously until the connecting rod is caught and reattached to the arm.

Because there are two tethers in this system that are spinning around each other instead of one single tether, this type of system has a larger tether drag compared to a balanced kite system with a single tether. The carousel also needs to keep rotating such that both tethers do not intertwine when the aeroplanes spin around each other. Two separate powerful winches would have to be used to control the length of both tethers independently, which complicates the routing of the tethers to not have them intertwine.

Figure 3.2 shows a possible solution for the positioning of the winches. The drums of the winches are mounted in line with the carousel shaft. To avoid obstruction of the upper winch for the tether of the lower winch, the tether of the lower winch is guided through the centre of the drum of the upper winch. Note that the motors are positioned statically with respect to the carousel, but the guidance mechanism for the tether rotates along with the carousel. The connection between the shaft and the drums consists of bearings, providing an independency in the rotating speeds of the drums and of the carousel. The winches and the carousel each have their own motor and the tether length can be controlled by varying the difference in rotation speed between the drum and carousel. When they rotate at the same velocity, the tether length remains constant. When a winch spins faster than the carousel its tether is reeled out and vice versa and when it spins slower its tether is reeled in. A downside of the set-up is that for the tether length to remain constant, the winch motor must continuously rotate the drum at the same speed as the carousel is spinning.

Figure 3.3 shows a clamping mechanism for the connecting rod. When the clamps are open, the tether can be reeled out to the desired length, at which point the clamps are closed and grip the tethers and the rod becomes the airborne connection. The clamping force can be delivered by a spring mechanism to avoid the need for actuators on the airborne rod. The actuators to open the clamps can be mounted on the carousel. In e.g. ski lifts comparable gripping mechanisms can be found. They are used to secure the gondola to the steel cable that runs up the mountain. The main tether of the system is made with Dyneema® fibres woven around a pair of copper conductors. Dyneema® is a synthetic polyethylene fibre with a high tensile strength (3.5 GPa) and a low weight ( $970 \frac{\text{kg}}{\text{m}^3}$ ). It is also resistant to abrasion, sunlight (UV), (sea)water, chemicals and micro-organisms, properties that are needed for an AWE set-up. The conductors are used to provide power to the aeroplane and communication between the aeroplane and the ground station. To avoid too much wear on the tether from the clamping, the pressure on the cable should be limited and distributed over a certain length. To increase the grip on the tether the surface of the clamp can be ribbed as in Figure 3.3.

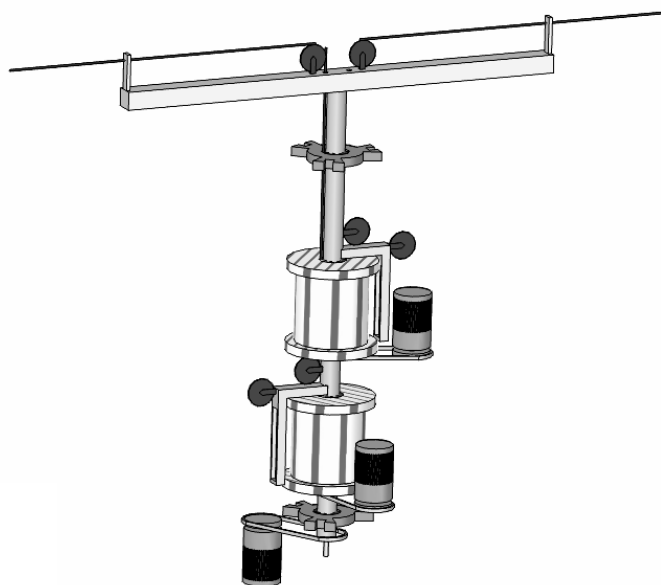


Figure 3.2: The winch drums mounted concentric with the carousel shaft but with an independent rotation speed [16].

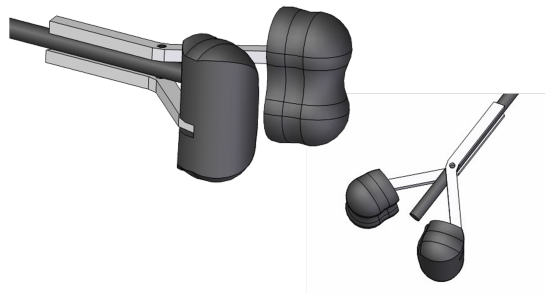


Figure 3.3: Conceptual drawing of a tether clamping mechanism [16].

### 3.3.2 Single tether

The single tether balanced kites system uses a single tether which leaves the carousel and splits mid-air into two separate tethers that go to both aeroplanes. The challenge here lies in realising the splitting point. First of all, the two aeroplanes likely spin around each other, causing the tether to twist. One

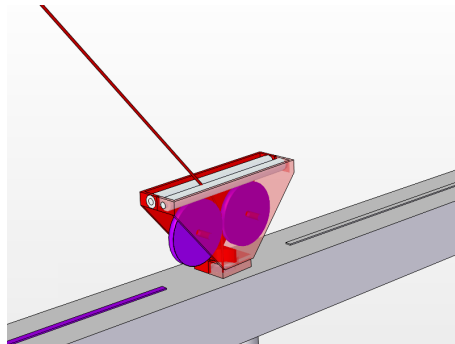


Figure 3.4: Pulley assembly at top of the arm that support tether in all directions [16].

possible solution to this problem is to have the winch rotate simultaneously with the aeroplanes, for example by mounting it on the carousel and rotating the carousel synchronously with the aeroplanes. Another alternative is to incorporate a swivelling joint in the splitting point, in combination with a slip ring to transfer power and signals.

Another challenge lies in releasing and reconnecting the short tethers that connect the aeroplanes to the main tether. During start-up, the rotation start requires those tethers to be connected to the end points of the arm to be able to drive the aeroplanes. When these tethers are unrolled to their desired length, they should be released such that the splitting point can become airborne. For landing, the short tethers need to be reattached to the arm.

A third challenge is the point where the tether leaves the carousel. The tether should be guided towards the winch at this point. Since the aeroplane can be flying in any direction with respect to the carousel, depending on the wind, the support must be able to guide the tether in all directions. Figure 3.4 shows a conceptual design of this support. Two pulleys equipped with bearings keep friction losses and tether wear to a minimum. These pulleys are mounted in a housing that allows them to rotate around the vertical axis. Above these two pulleys, rollers are mounted that, when the tether changes directions, turns the pulleys to realign with the tether.

An advantage of this single tether option is that only one powerful winch is needed for the power production phase. This winch can be static when a swivel is used. The single tether option also has less tether drag compared to the double tether option. Its challenges lie in realising the launch and mainly the landing, where the two shorter tethers need to be reattached to the arm.

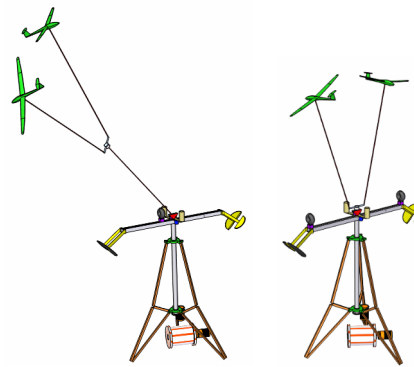


Figure 3.5: Step 1: landing the airborne connection [16].

### 3.3.3 Selected configuration and conceptual design

Both the single and the double tether configuration have their advantages and disadvantages. For both, mainly the landing phase is insecure. In the double tether configuration the connecting rod needs to be caught during landing, in the single tether configuration the splitting point and two shorter tethers need to be reattached to the carousel. Since the double tether configuration has more tether drag and has a larger airborne weight to make the connection between both tethers, the single tether configuration is further investigated. Another reason to choose for the single tether configuration is that it only needs a single winch, and the system can easily be used with a single kite. The winch can either be rotating with the carousel, or can be placed static next to the carousel when a good swivelling joint is used. In what follows, the landing of the balanced kites is described. The figures used are purely conceptual.

In the descending phase, the main tether is continuously reeled in until the swivelling joint landed on the central support point, as Figure 3.5 shows.

Up to this point, the aeroplanes are driven by the reeling in of the tether. With the swivelling joint landed they are no longer driven by the carousel. In [16] a rough estimate is made that within 10 seconds the next action must be completed or they will likely crash on the ground if the aeroplanes lack an on-board propeller. Since also during start-up the aeroplanes cannot be powered after the shorter tethers have been released, a balanced kites system will likely need to use some on-board propulsion.

The next action is to catch the short tethers and fix them to the ends of the arms of the carousel. From that point on, the aeroplanes are again driven by

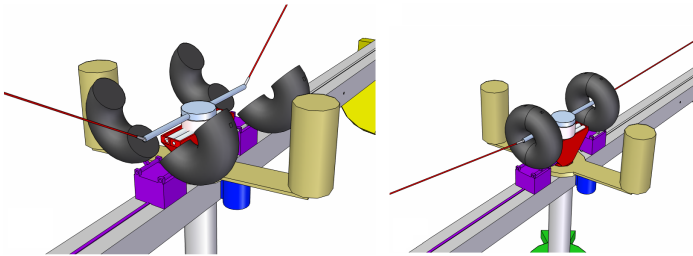


Figure 3.6: Step 2: gripping the short tethers [16].

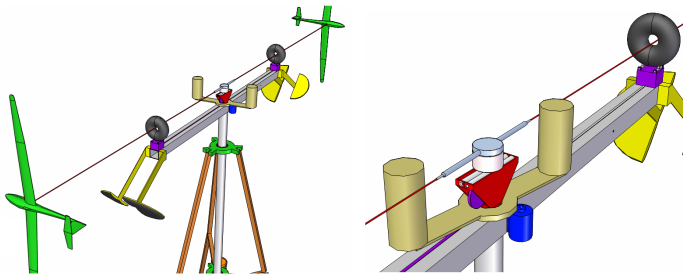


Figure 3.7: Step 3: Bringing the attachment points to the end of the arm, reeling in the tethers and landing the kites [16].

the carousel until they land on their cradle. Figure 3.6 shows a possible way to catch the short tethers. The short tethers are connected to two short rods that extend out the side of the swivelling joint. The advantage here is that the rods have a fixed orientation with respect to the swivelling joint in contrast with the free moving tethers. The torus shaped grippers are opened until the rods are in position and are then closed. The grippers are now moved outwards to the end of the arm.

With the grippers at the end of the arm, the aeroplanes are driven by the carousel. The next action is to reel in the short tethers. This requires a winch on which the tethers are wound. This winch is interpreted as two upstanding cylinders, see Figure 3.7. By rotating the cylinders around the centre of the carousel, the short tethers are reeled in with every rotation until they are reeled in completely.

## 3.4 Single kite set-up

This section presents the design of the single kite set-up that is used for the outdoors flight experiments in the ERC Highwind project. Although a goal of the ERC Highwind project is the development of a balanced kites set-up, initially a set-up that is capable of the rotation start of a single kite is developed, which is already a challenging task on its own. This set-up can later be expanded to a balanced kites set-up. The two main components of the set-up are the carousel and the winch, which are described in detail in Section 3.4.1 and Section 3.4.2 respectively. The aeroplane that is used for the outdoors flight experiments is shortly described in Section 3.4.3. The electrical design of the motors that power the carousel and winch is outlined in Section 3.4.4. The line angle sensor that measures the angle between the tether and the carousel arm, and also serves as the tether attachment point, is discussed in Section 3.4.5.

### 3.4.1 Carousel

The carousel is responsible for towing the aeroplane during the rotation start. Figure 3.8 shows the designed and built outdoors carousel. The winch is mounted underneath the carousel hanging from the central shaft of the carousel. It rotates together with the carousel and is discussed in detail in Section 3.4.2. The tether is guided by a level wind mechanism which leads it up through the central shaft. At the top of the pulley the tether makes a 90° angle and heads to the end of the arm.

The frame of the carousel is mounted on a trailer. Similar to the indoors carousel, it consists of a truss-like frame surrounding the central shaft. It consists of square extruded aluminium tubes that are inexpensive, corrosion resistant and easy to machine. They are connected to each other using bolts and nuts put through holes in the tube wall. This way of connecting the tubes, that is also used for the indoors carousel, does not require extra components to connect the different tubes. It does require different size profiles to fit together. As can be seen from Figure 3.8, the carousel has four legs instead of three because this allows easier mounting on a trailer. On the trailer a space of 2 by 4 m is available, but some space should be left over for the electrical cabinets and storage space. The height of the carousel on the trailer cannot exceed 4 m because of road regulations. The trailer has a height of 0.7 m, limiting the height of the structure to 3.3 m. The space underneath the structure needed for the winch is estimated to be approximately minimum 0.9 m wide and 1.3 m high. To be able to provide sufficient space, an extra triangle is added to the legs between the two larger triangles when compared to the indoors carousel.



Figure 3.8: The designed and built outdoors carousel.

The sizing of the central shaft is stiffness driven such that the end point of the arm does not move too much under influence of the forces of the aeroplane. To keep the angular displacement of the arm when the tether pulls radially on the arm under  $2^\circ$ , a tube with an outer diameter of 10 cm and a wall thickness of 10 mm is used.

The central shaft is supported by two bearings. They have to support the weight of the arm, central shaft and winch that give an axial force and the tether force that gives an axial and radial force, depending on the direction of the tether. A combination of a tapered roller bearing at the top and a deep groove ball bearing at the bottom is chosen for this load. The tapered roller bearing can take a high axial and radial load such that the lower ball bearing is only loaded radially. Because the outer diameter of the extruded aluminium shaft is hard to precisely machine, needed for mounting the bearings, the bearings are mounted

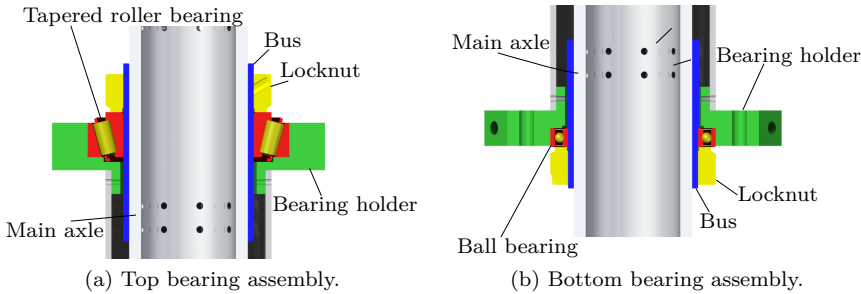


Figure 3.9: Top and bottom bearing assemblies.

on buses. The outer diameter of these buses can be easily machined to fit the tolerances needed for the bearings, and the inner diameter can be easily adjusted to fit around the main shaft. The bearings are placed in machined aluminium bearing holders and are held in place by locknuts that screw onto a threaded part of the buses and push on the inner part of the bearings. Figure 3.9 gives an impression of the two bearing assemblies.

The diameter of the arm is chosen to be 4 m, which is twice that of the indoors carousel. This longer arm length provides more clearance for the aeroplane from the carousel, limits the rotation speed needed to reach the same aeroplane velocity and it increases the towing capabilities as is shown in Section 1.5. The arm must also be easy to remove, for example when the set-up has to be moved over a long distance. It consists of a hollow square aluminium profile connected to an ITEM-profile that serves as the connection to the main shaft. The bending moment the tether can exert on the arm is determining for the arm dimensions and a profile of 100x100x10 mm is suited to handle the loads. If needed, the arm can be easily replaced by a longer one since it only requires drilling a few holes in the extruded aluminium profile.

To assert the stresses and displacements of the structure remain within acceptable levels, static and dynamic loading analyses are done in [16]. The lowest eigenfrequency of the structure is found at 8 Hz. Since the loads are expected to vary at a frequency around 1 Hz, the maximum rotating frequency of the carousel, this poses no problem.

This carousel is mounted on a trailer equipped with four support legs such that during operation, the trailer can be lifted from its tires which would otherwise introduce large oscillations. Even with these support legs, the trailer adds additional oscillations to the system. A dynamic analysis of the carousel mounted on the trailer in [16] found a first natural frequency around 4 Hz. This

should still be acceptable, but if needed, additional measures such as adding extra supports, can be taken. The technical drawings of all components used to build the carousel can be found in Appendix A.

### 3.4.2 Winch

The winch is a key component in the set-up since it converts the mechanical work exerted by the aeroplane on the tether into electric power. The winch is mounted underneath the carousel, hanging from the central shaft. The tether has to be guided through this central shaft to the top of the arm where it makes a 90° angle towards the end of the arm, from which it goes out to the aeroplane.

A reel-out speed of  $6 \frac{\text{m}}{\text{s}}$  at a tether force of 1800 N is required for the generator-mode resulting in a power of approximately 10 kW. A reel-in speed of  $8 \frac{\text{m}}{\text{s}}$  at a tether force of 500 N is required for the motor-mode. At least 100 m of tether with a diameter of 3 mm should fit on the winch drum. The drum must have a diameter larger than 10 cm to avoid a large decrease of the tether life time or damage to the copper conductors. For a steel cable, the advice is to keep the radius of curvature above 30 times the tether diameter. The Dyneema® tether is not as stiff as a steel cable, but to avoid wear it is wise to maintain the same minimal curvature.

The winch consists of a few key components that are connected through the winch frame. The two most important components are the winch motor and the winch drum. They are connected via a timing belt and pulleys that transfer the power between the drum and the motor. A level wind mechanism is also part of the winch construction. It ensures even winding of the tether as it gets reeled in and out. A slip ring is mounted on the drum shaft to provide power and communication to the aeroplane via the tether. These different components are discussed in more detail below. Figure 3.10 shows the completed design of the winch as it is mounted under the carousel in different side views with some of the components annotated.

The winch frame is constructed using a front plate, visible in Figure 3.10a, connected to aluminium item profiles that allow fast manufacturing and easy assembly. Although all components have at least an IP54 rating, a Plexiglas housing around the winch frame offers some extra weather protection and keeps the tether clean and dry.

The winch motor is mounted on the front plate. Section 3.4.4 discusses the details of this motor. A timing pulley is mounted on the motor shaft. One side of the shaft on which the drum is mounted is also mounted on the front plate via a pillow block bearing with spherical races. The spherical races allow



Figure 3.10: Side views of winch.

up to  $2^\circ$  misalignment such that the assembly of the winch can be done by hand. The other side of the drum shaft is connected to the back plate, visible in Figure 3.10b, which is in turn connected to the frame of item profiles. A

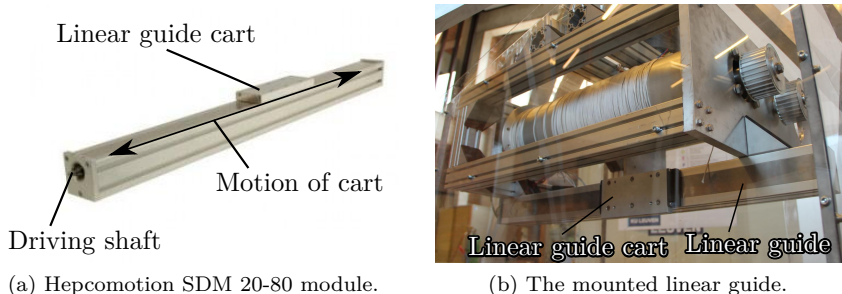


Figure 3.11: Linear guide of level wind mechanism.

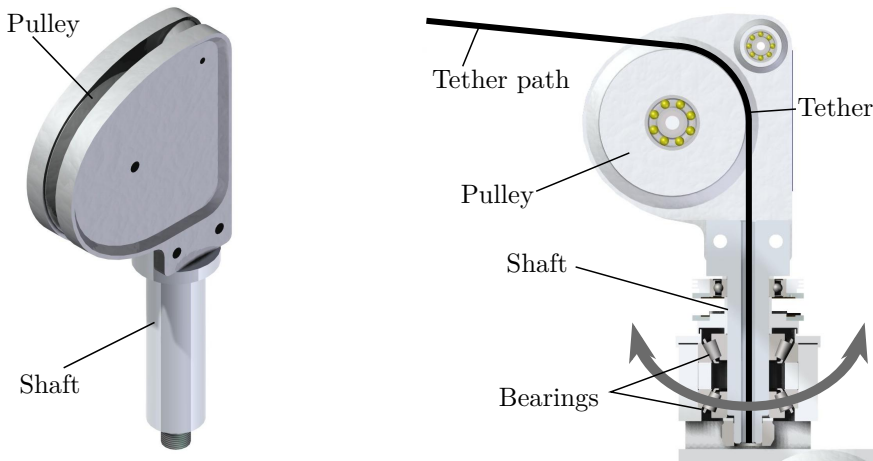
timing belt is used to transfer the power between the motor and the drum. This timing belt does not require tight positioning of the motor and drum and allows a misalignment between the drum and motor shaft of up to  $0.5^\circ$ . This offers a margin of about 15 mm for the positioning of the back plate of the drum. A tensioning pulley, visible in Figure 3.10a is used to preload the belt such that there is no slipping of the belt.

The winch drum of the indoors carousel uses grooves to guide the even winding of the tether. This method is not very robust and prone to bad winding. The drum of the outdoors carousel therefore has a smooth surface, and a level wind mechanism that ensures even winding of the tether. Similarly to the carousel structure, the drum material is aluminium because it is light, easy to machine and corrosion resistant. The winch drum has a diameter of 200 mm and a length of 615 mm and is capable of holding 128 m of tether on a single winding.

A level wind mechanism is needed to ensure the tether is wound up evenly. It consists of a pulley mechanism mounted on a linear guide. The linear guide is a Hepcomotion SDM 20-80 unit and is shown in Figure 3.11a. It has a length of 950 mm and a pitch of 5 mm. This means that one rotation of the driving shaft of the linear guide moves the cart by 5 mm. The linear guide is mounted on the underside of the winch frame as shown in Figure 3.11b.

The linear guide is driven by the rotation of the drum, meaning that if the drum rotates, the linear guide cart moves accordingly. They are connected via a timing belt at the back side of the drum, as shown in Figure 3.10b. By properly selecting the ratio between the pulley on the drum and the pulley on the linear guide, level winding of the tether is assured. For a tether diameter of 3 mm, a ratio of 5 : 3 is needed such that the cart moves 3 mm for one rotation of the drum. This passive way of driving the linear guide is easy in use compared to using a separate motor to drive the mechanism. Once installed and outlined, no further action is required for the driving of the linear guide. Several pulley ratios are available to allow a change of tether diameter. A downside of driving the linear guide passively is that only one winding is possible this way. If in a later stage multiple windings are needed, a motor can still be installed.

To guide the tether from the central shaft to the drum, a pair of two swivelling pulleys is used. A rendered view such a pulley is shown in Figure 3.12a. It consists of a pulley with a diameter of 100 mm mounted in between two plates. These plates are mounted on a hollow shaft. The pulley is positioned tangential to the shaft such that the tether coming of the pulley is sent through the hollow shaft. Figure 3.12b shows a cross section of the pulley as it is mounted in two bearings. Because the tether goes through the centre of the shaft around which the bearings are mounted, the pulley assembly can rotate without interference of the tether, as indicated by the arrow in Figure 3.12b.



(a) Rendered view of swivelling pulley.

(b) Cross section of swivelling pulley.

Figure 3.12: Swivelling pulley used for level wind mechanism.

A pair of two such swivelling pulleys is mounted on the winch as shown in Figure 3.13. One of the pulleys (the pulley on the left in the figure) is mounted on the linear guide cart via two bearings and is aligned such that the tether leaves the shaft tangential to the drum. The other pulley (the pulley on the right in the figure) has its shaft aligned with the central shaft of the carousel. The path of the tether is indicated by the thick black line in Figure 3.13. The tether force keeps the pulleys facing each other as the linear guide moves back and forward. At the top of the carousel, a fixed pulley guides the tether from the central shaft to the end of the arm.

The connection between the winch and the central shaft is shown in Figure 3.14 (the central shaft goes through the centre of the black carousel slip ring visible in this figure). It is done in a way that allows adapting the position of the winch during construction such that the centre of mass can be aligned with the central shaft of the carousel. The connection plate is able to move along the two item profiles that span across the winch, as indicated by the arrows in the Figure 3.14. These item profiles are in turn able to move along the other direction, allowing adjustments of the position of the centre of mass of the winch in both directions.

To provide the aeroplane with power and for data communications, the tether carries electrical conductors. Therefore a slip ring is mounted on the drum shaft as indicated in Figure 3.10c. Although normally only two conductors are

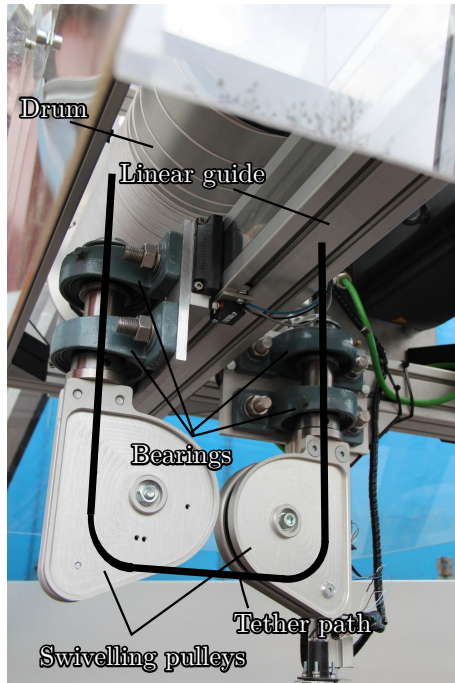


Figure 3.13: Swivelling pulleys as mounted on the winch.

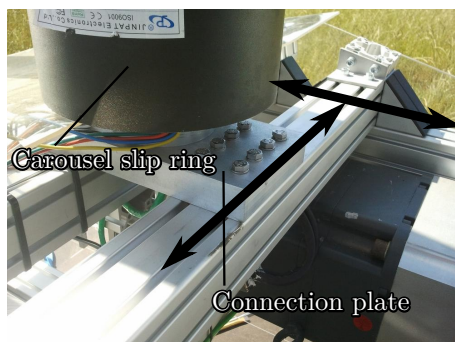


Figure 3.14: Connection between the winch and the carousel.

needed, the slip ring can transfer up to six power (up to 5 A at 400 V) or data connections for possible future usage. The technical drawings of all components used to build the winch can be found in Appendix B.

### 3.4.3 Aeroplane

The aeroplane that is used for the outdoors set-up is the X-models Sting ray heavy slope version [98]. It has a wing span of 2.9 m and a total wing area of 1 m<sup>2</sup>. It is a glass-fibre model aeroplane with carbon fibre reinforcements in the wing. It has a large fuselage that offers enough space for all actuators, electronics and sensors that are needed on-board the aeroplane. Development of the aeroplane started in [63] but is not the further subject of this thesis.

### 3.4.4 Electrical design

The electrical design of the set-up comprises the selection of the motors, converters and power electronics. The selection and design is discussed in more detail in the master thesis of J. Stuyts and W. Vandermeulen [88].

As mentioned in Section 3.4.2, the winch should be able to deliver a force of about 1000 N at a reel-out speed of  $6 \frac{\text{m}}{\text{s}}$  and be able to reel in at  $8 \frac{\text{m}}{\text{s}}$  with a force of 500 N. With a drum diameter of 0.2 m, this results in a nominal torque of 100 N m and a maximum rotation speed of 764 rpm. Since holding torque is required at low speeds during the rotation start, external cooling is required. Because the winch is mounted underneath the carousel, a lightweight motor is preferred. To have a fast control of the tether, a dynamic motor is required. A Permanent Magnet Synchronous Machine (PMSM) is a suitable option that fits all of these requirements. It is lightweight, efficient and dynamic at the same time.

The requirements for the carousel motor are less stringent. [16] derived that a power of 1 kW at a rotation speed of 60 rpm is needed to drive the carousel. To launch two aeroplanes in a balanced kites set-up, 2 kW is thus needed. To allow the use of bigger aeroplanes in the future, a nominal power of 4 kW is chosen. This motor should preferably be simple and robust. An induction machine (IM) is a suitable option.

Based on the requirements, a solution of Siemens best suits our requirements. Figure 3.15 gives a schematic overview of the Siemens proposal.

For the winch motor a permanent magnet synchronous machine (PMSM) with a nominal power of 8.2 kW is selected. It weighs 51.6 kg (with brake and gearbox) and has a 91 % efficiency at full load (with gearbox) [84]. With a gearbox with ratio of 3, the nominal outgoing rotational speed of the motor is 1000 rpm. If needed, the motor can go faster, being limited by the gearbox's input speed of 1600 rpm. An additional holding brake is included to block the winch when the motor is not powered. A resolver is used to provide position feedback. The

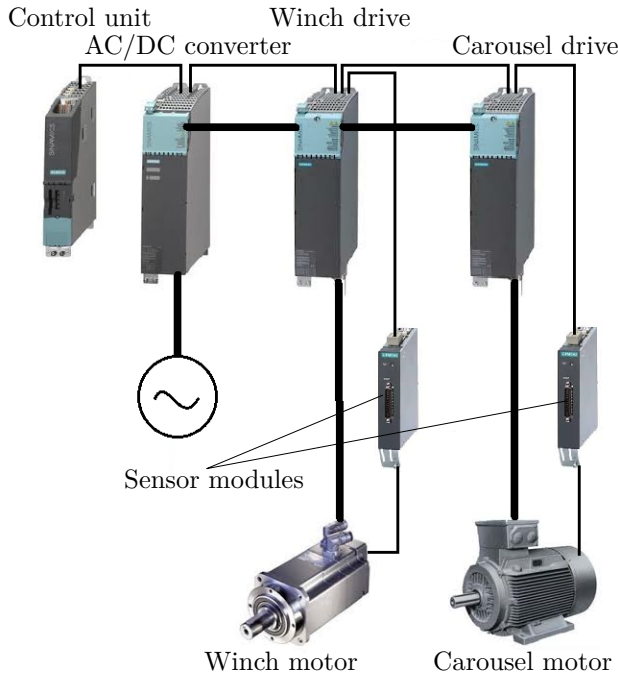


Figure 3.15: Siemens proposal for electrical drive system.

signal of a resolver is supposed to be more robust than an incremental encoder against noise the slip ring would introduce. The proposed winch motor is not capable of delivering the required nominal torque at the required rotational speed. With gearbox the nominal output torque is 78 N m, which is lower than the estimated required 100 N m. A PMSM however is capable of overloading [40] and since the required nominal values are an overestimation, this is not considered a problem. It is rated IP64, which means it is dust tight and can handle splashing water. This offers enough protection for the circumstances the motor has to work in. It is further more protected by the Plexiglas housing around the winch frame.

For the carousel motor a 4-pole induction machine of 4 kW is selected. It weighs 52 kg (with gearbox) and has an 86.6 % efficiency at full load (with gearbox). An incremental encoder provides position feedback. The proposed carousel motor is easily capable of delivering the required torque at the required rotational speed with a gearbox with a reduction ratio of 14.68. The IM is also robust

enough and should be able to slow the carousel down, as the power can be sent back to the grid and to an additional braking resistor. It is rated IP55, which means it is dust protected and can handle water jets. This higher protection against water is desirable since it is not protected by a housing, as is the case for the winch motor, and it may be subject to rain during experiments, but also during moving of the set-up when the rain may have more impact.

To power and control the drives, an active rectifier builds up a 600 V DC bus from the three-phase net connection. This DC bus is connected to the two motor modules. Each motor module is connected to its motor with a power cable. The encoder/resolver signals from the motors are sent to sensor modules, which are connected to the appropriate motor module as well. All modules are controlled by a single control unit.

Communication with the drives goes via a Programmable Logic Controller (PLC). The PLC is connected to the control unit via ProfiNet. Communication between the PC, on which the control and estimation software runs, goes over TCP/IP. An advantage of a PLC is that part of the logic can be implemented on this device. The PLC would then e.g. be able to do the start-up procedure of the drive via a simple start command. This means that the communication part on the PC can be kept very basic and e.g. only speed references need to be sent. The PLC is also used to interface other components, such as the limit switches of the linear guide and relays. The logic behind the limit switches is then implemented in the PLC.

### 3.4.5 Line angle sensor

Measurements of the position of the aeroplane are needed to be able to control it. For this purpose, the stereo vision system is developed on the indoors set-up. This system is not usable for the outdoors set-up because the sun and higher illumination of the surroundings make it hard to properly detect the markers. The larger distance between the aeroplane and the carousel also increases the difficulty of detecting the markers, and it decreases the accuracy of the measurements. Therefore we propose to use a line angle sensor to provide measurements of the position of the aeroplane. The sensor measures the azimuth (horizontal angle) and elevation (vertical angle) of the tether with respect to the carousel arm. An advantage of a line angle sensor compared to the vision system used on the indoors set-up is that it does not rely on an external signal and is independent of changing circumstances such as varying illumination. It can also deliver measurements at a fast sampling rate without any meaningful delay such that synchronising the measurements forms less of an issue. A downside is that, for longer tether lengths, the accuracy of the line angle sensor decreases

because the tether is not straight but sags due to gravity and the wind blowing on the tether. A model can be used to describe the deformation of the tether, but will never completely capture this complex behaviour. On the plus side, the position accuracy needed when flying on a long tether is lower than when flying on a shorter tether. If the accuracy of the line angle sensor for long tether lengths becomes a problem, an alternative system such as GPS can be used. The line angle sensor then only provides accurate measurements during the rotation start, when the aeroplane is performing high acceleration aerobatic manoeuvres and GPS would not work.

The line angle sensor also has a second function. It namely also serves as the pulley mechanism at the end of the arm that serves as the tether attachment point. It thus needs to be strong enough to take the force of the tether.

For the azimuth angle, a range of  $360^\circ$  continuous rotation is required to allow the carousel to be rotating when the aeroplane is flying crosswind. For the elevation, almost  $180^\circ$  is required. A margin of about  $20^\circ$  is allowed for vertically up and vertically down, since the aeroplane does not fly so low or so high. A low friction of the sensor is required to limit the effect of the sensor on the tether.

A challenge in the design of the line angle sensor is the continuous  $360^\circ$  azimuth range, since it complicates how to transfer the elevation information through the azimuth rotation axis. An IP rated slip ring to transfer an encoder signal introduces high friction. A wireless connection still requires power, either wired over a slip ring, or with batteries which are unreliable because they may run out during an experiment and need to be replaced regularly.

Figure 3.16a shows a rendered figure of the developed line angle sensor. The sensor is mounted at the end of the arm via the two U-profiles. The tether comes from the centre of the carousel and is guided upwards via a pulley in between the two U-profiles. The tether then goes through the same type of swivelling pulley used for the linear guide of the winch. Mounted on this swivelling pulley is a 1 m long '*guidance rod*', annotated in Figure 3.16a, with at the end a small tether guide through which the tether is routed. The idea is that the guidance rod increases the moment arm of the tether when the swivelling pulley is not aligned with the tether such that the swivelling pulley closely follows the azimuth of the tether. The elevation of the guidance rod closely follows the elevation of the tether. The tether path is schematically shown in Figure 3.17. The swivelling pulley is mounted in a housing that holds two bearings such that it can swivel around the vertical axis to follow the azimuth of the tether. A pair of two back-to-back tapered roller bearings is used such that both radial and axial forces can be supported. The guidance rod is mounted on the swivelling pulley via a '*guidance bracket*', annotated in Figure 3.16a and Figure 3.17. This guidance bracket is in turn mounted on a bearing, as indicated in Figure 3.16b,

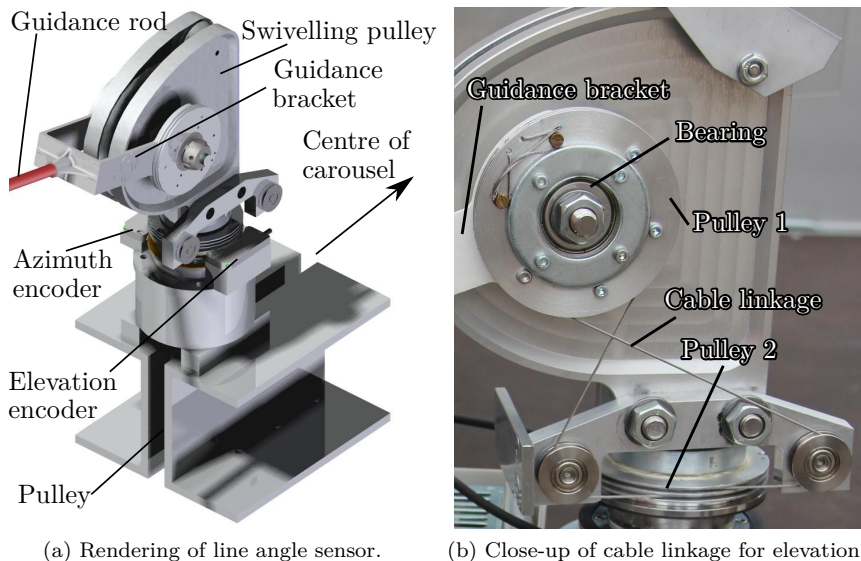


Figure 3.16: Line angle sensor.

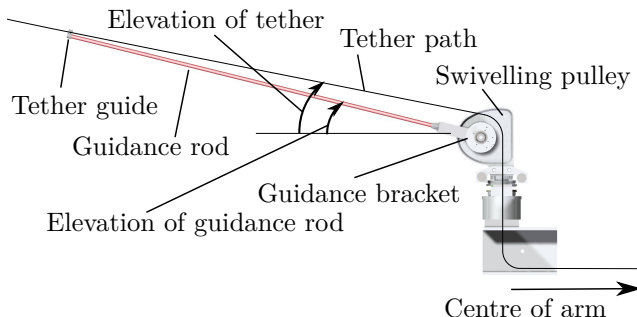


Figure 3.17: Schematic representation of tether path through line angle sensor.

such that it can rotate around the centre of the swivelling pulley. At the end of the guidance rod is a small tether guide through which the tether is routed such that the guidance rod follows the motion of the tether. Figure 3.18 shows the tether guide, which is spiralled rather than having a simple hole in it such that the tether can be looped through it and the aeroplane does not need to be detached to connect the tether to the sensor.



Figure 3.18: Tether guide at end of guidance rod with spirals such that the tether can be looped through.

To measure the azimuth of the tether, a non-contact absolute magnetic encoder ring is mounted on the shaft of the swivelling pulley right above the bearing housing. Since the encoder is contactless, it introduces no friction, and because it is an absolute encoder, no homing procedure each time the set-up is started is needed.

To measure the elevation of the tether, the elevation of the guidance rod can be measured. Note that the elevation of the guidance rod is not exactly equal to the elevation of the tether, as indicated in Figure 3.17, but it is proportional to it. To measure the elevation of the guidance rod without the need for slip rings or wireless encoders, a cable linkage can be used. Figure 3.16b shows a close-up of this cable linkage. It consists of a cable and two pulleys that are mounted on bearings, annotated as pulley 1 and pulley 2 in Figure 3.16b. Pulley 1 is connected to the guidance bracket and thus follows the elevation of the guidance rod. Pulley 2 is mounted on a bearing around the shaft of the swivelling pulley such that it can rotate independently of the swivelling pulley. The cable links the two pulleys, such that if pulley 1 rotates, pulley 2 also rotates. Now when the tether elevation changes, the guidance rod moves up or down along with the tether, causing pulley 1 to rotate. This in turn causes pulley 2 to rotate. The angle of pulley 2 can then be measured similar to how the azimuth angle is measured. For this purpose, the same type of magnetic encoder is mounted on pulley 2, as annotated in Figure 3.16a. Note that when swivelling pulley rotates, both the azimuth and elevation encoder rotate together. The actual elevation is the difference in the angle between both encoders.

The developed mechanism to measure the elevation angle without the use of slip rings could also be used in other applications, for example in a system where instead of measuring the angles, a rod needs to be actuated. The encoders could be replaced by two motors, allowing in this case full 360° rotation of the rod without the need to place a motor on the rotating part.

### 3.5 Conclusion

This chapter outlined the design and development of the outdoors test set-up that will be used for the outdoors flight experiments. An analysis of the requirements of a balanced kites system is done, resulting in a possible design for such a system. The option in which one main tether splits mid-air into two shorter tethers is selected and conceptually designed.

Based on the design of the balanced kites set-up, a single-kite set-up is developed consisting of a carousel to perform the rotation start and a powerful winch that can perform the pumping cycle. It is installed on a trailer such that it can be driven to remote locations. The carousel's rotation is driven by a powerful 4 kW induction motor. The winch motor is an 8.2 kW permanent magnet synchronous machine that is capable of overloading to reach the maximum required torque.

The set-up is equipped with a line angle sensor that measures the horizontal and vertical angle between the tether and the arm and at the same time serves as the tether attachment point on the carousel. The sensor is capable to measure the horizontal angle in a continuous 360° rotation without the need for slip rings or wireless communication for the vertical angle due to a clever cable linkage that transfers the vertical rotation to a horizontal rotation. Two contactless magnetic encoders measure both angles.



## **Part II**

# **MHE with application to AWE**



# Chapter 4

## State estimation

### 4.1 Introduction

This chapter gives a theoretical background of state estimation which is needed to understand the developments in Chapter 5 and Chapter 6. State estimation covers the topic of combining information gathered from multiple sensors, previous information and system knowledge to provide an estimate of the state of the system. Typically not all states can be directly measured, because doing so would be too costly or simply impossible. The measurements that are available are typically noisy. Usually the states and outputs are interconnected by the model equations, but they in turn are imperfect. It is the task of the state estimator to form a state estimate that best fuses these different information sources taking into account their trustworthiness.

This chapter is organised as follows: Section 4.2 presents the general formulation of a system and measurement model, Section 4.3 discusses the full information estimation problem, Section 4.4 discusses recursive state estimators in the form of the Kalman filter and some of its nonlinear modifications, and Section 4.5 discusses Moving Horizon Estimation (MHE). Section 4.6 concludes the chapter.

### 4.2 Model representation

To present different estimation techniques, we first define the format of the two models that represent the system; the system dynamics and the measurement

model. The following continuous time system model is proposed:

$$\mathbf{0} = \mathbf{f}(\mathbf{x}(t), \dot{\mathbf{x}}(t), \mathbf{u}(t), \mathbf{w}(t)), \quad (4.1)$$

which in general can be a differential algebraic equation (DAE), but can often be simplified to an ordinary differential equation (ODE). The variable  $\mathbf{x}(t)$  is the system state,  $\mathbf{u}(t)$  is the control input and  $\mathbf{w}(t)$  is the process noise. Equation (4.1) is often needed in a discretised form, which can be written as:

$$\mathbf{x}_{k+1} = \mathbf{F}(\mathbf{x}_k, \mathbf{u}_k, \mathbf{w}_k), \quad (4.2)$$

in which  $\mathbf{F}$  is an integrator that integrates the continuous time model  $\mathbf{f}$  over one sampling period  $T_s$  and where  $\mathbf{x}_k = \mathbf{x}(t_k)$  and  $t_{k+1} = t_k + T_s$ . The control input  $\mathbf{u}_k$  and the process noise  $\mathbf{w}_k$  are assumed constant over the sampling period.

Parameters that are unknown and need to be estimated can be handled by treating them as additional state variables [52] that evolve according to:

$$\dot{\mathbf{p}}(t) = \mathbf{w}_p(t) \quad \text{in continuous time,} \quad (4.3a)$$

$$\mathbf{p}_{k+1} = \mathbf{p}_k + \mathbf{w}_{p_k} \quad \text{in discrete time,} \quad (4.3b)$$

with  $\mathbf{w}_p(t)$  and  $\mathbf{w}_{p_k}$  additional disturbances.  $\mathbf{p}(t)$  and  $\mathbf{p}_k$  are then included in  $\mathbf{x}(t)$  and  $\mathbf{x}_k$  respectively.

The measurement model of a system can in general be written as:

$$\mathbf{y}(t) = \mathbf{h}(\mathbf{x}(t), \mathbf{u}(t), \mathbf{v}(t)), \quad (4.4)$$

in which  $\mathbf{y}(t)$  is the measurement at time  $t$  and  $\mathbf{v}(t)$  is the measurement noise. In a discretised form, the measurement function reads:

$$\mathbf{y}_k = \mathbf{h}(\mathbf{x}_k, \mathbf{u}_k, \mathbf{v}_k). \quad (4.5)$$

Unless otherwise stated, it is assumed that the disturbances  $\mathbf{w}(t)$  and  $\mathbf{v}(t)$  have a Gaussian distribution with zero-mean and covariance  $Q(t)$  and  $R(t)$  respectively. This yields Gaussian distributions for the discrete-time disturbances  $\mathbf{w}_k$  and  $\mathbf{v}_k$  as well with covariances  $Q_k$  and  $R_k$  that are related to their continuous-time equivalents by:

$$Q_k = Q(t_k)T_s, \quad (4.6a)$$

$$R_k = R(t_k). \quad (4.6b)$$

### 4.3 Full information estimation

When the complete measurement history of the system is available until the current time, the estimation problem is called a full information problem and the estimator that uses the complete measurement history is referred to as the full information estimator. The full information estimator has the best theoretical properties in terms of stability and optimality [72]. The full information problem aims at estimating the state trajectory  $\mathbf{x}(t)$  from all measurements obtained from the starting time  $t = 0$  until the current time  $t = t_c$ .  $\mathbf{x}(t_c)$  is the state at the current time. For systems where the disturbances have a Gaussian distribution, the full information problem is formulated as a least-squares problem as:

$$\begin{aligned} \underset{\mathbf{x}(\cdot), \mathbf{w}(\cdot), \mathbf{v}(\cdot)}{\text{minimise}} \quad & \|\mathbf{x}(0) - \bar{\mathbf{x}}_0\|_{P_0^{-1}}^2 + \\ & \int_0^{t_c} \|\mathbf{w}(t)\|_{Q(t)^{-1}}^2 dt + \int_0^{t_c} \|\mathbf{v}(t)\|_{R(t)^{-1}}^2 dt \quad (4.7) \end{aligned}$$

subject to  $\mathbf{0} = \mathbf{f}(\mathbf{x}(t), \dot{\mathbf{x}}(t), \mathbf{u}(t), \mathbf{w}(t))$ ,

$$\mathbf{y}(t) = \mathbf{h}(\mathbf{x}(t), \mathbf{u}(t), \mathbf{v}(t)),$$

where  $\bar{\mathbf{x}}_0$  is the a priori knowledge about the system state with corresponding covariance  $P_0$ . The first term in the objective of Problem (4.7) is the cost related to the a priori knowledge. The second term is the cost related to the process noise  $\mathbf{w}(t)$  and the third term the cost related to the measurement noise  $\mathbf{v}(t)$ . Note that, although most commonly used, the 2-norm is not the only possible penalty function for the different noise terms. It yields the maximum likelihood estimate when  $\mathbf{w}$  and  $\mathbf{v}$  are normally distributed with zero mean. When the noise is non-Gaussian, other penalty functions can be used. Solving Problem (4.7) yields the optimal state trajectory  $\mathbf{x}(t)$ , with  $\mathbf{x}(t_c)$  the estimate of the state at the current time.

Since typically measurements and control inputs are only obtained and applied on discrete points in time, problem (4.7) is normally given in a discretised form as:

$$\begin{aligned} \underset{\mathbf{x}, \mathbf{w}, \mathbf{v}}{\text{minimise}} \quad & \|\mathbf{x}_0 - \bar{\mathbf{x}}_0\|_{P_0^{-1}}^2 + \\ & \sum_{k=0}^{N_c-1} \|\mathbf{w}_k\|_{Q_k^{-1}}^2 + \sum_{k=0}^{N_c} \|\mathbf{v}_k\|_{R_k^{-1}}^2 \quad (4.8) \end{aligned}$$

subject to  $\mathbf{x}_{k+1} = \mathbf{F}(\mathbf{x}_k, \mathbf{u}_k, \mathbf{w}_k)$ ,

$$\mathbf{y}_k = \mathbf{h}(\mathbf{x}_k, \mathbf{u}_k, \mathbf{v}_k),$$

where  $N_c$  is the number of measurements taken until the current time, and thus  $N_c T_s = t_c$ . The number of optimisation variables in Problem (4.8) is equal to  $n_o = (N_c + 1)(n_x + n_v) + N_c n_w$ , with  $n_x$ ,  $n_v$  and  $n_w$  the size of  $\mathbf{x}$ ,  $\mathbf{v}$  and  $\mathbf{w}$  respectively.

Because more and more measurements are obtained as time evolves, the number of optimisation variables grows and the computational burden to solve the full information problem increases and it quickly becomes impossible to solve the problem in a limited time. In case of linear system and measurement models and zero mean Gaussian noise, the full information problem can be formulated recursively in the form known as the Kalman filter. When the system or measurement models are nonlinear, suboptimal generalisations to the Kalman filter such as the extended Kalman filter (EKF) and the unscented Kalman filter (UKF) can be used. Recursive state estimation techniques such as the Kalman filter and several of its nonlinear variations are discussed in Section 4.4.

A different estimation approach is known as Moving Horizon Estimation. It uses a set of the most recent measurements, and summarises the information contained in previous measurements in the a priori knowledge. It is discussed in more detail in Section 4.5.

## 4.4 Recursive state estimation

The most popular tool for online state estimation is the Kalman filter. It is developed by R.E. Kálmán in 1960 [62] and gives the maximum likelihood estimate in a recursive form to the full information problem for linear systems with Gaussian noise. It is discussed in Section 4.4.1. For nonlinear systems, the Kalman filter is used as an approximation and several variants exist that approximate it in different ways. The extended Kalman filter is the most commonly used variation that linearises the system and measurement model and then uses the same equations as the Kalman filter. It is discussed in Section 4.4.2. The unscented Kalman filter is often used for estimation of the position and orientation of moving targets and is discussed in Section 4.4.3. Other variants such as the iterated extended Kalman filter and the linear regression Kalman filter exist. An overview of these different variants can be found in [68] but are not the subject of this thesis.

#### 4.4.1 Kalman filter

The Kalman filter algorithm consists of 2 steps; a prediction and a correction step. In the prediction step, estimates of the state and covariance for the current time are made. The Kalman filter assumes the state evolves according to a linear model given by:

$$\mathbf{x}_k = F\mathbf{x}_{k-1} + B\mathbf{u}_{k-1} + G\mathbf{w}_{k-1}. \quad (4.9)$$

Measurements of the system are made according to the linear model given by:

$$\mathbf{y}_k = H\mathbf{x}_k + \mathbf{v}_k. \quad (4.10)$$

Given  $\mathbf{x}_{k-1|k-1}$ <sup>1</sup> and  $P_{k-1|k-1}$ , the state estimate and covariance at time  $k-1$  given all measurements up to that time, the prediction step, or time update, is given by:

$$\mathbf{x}_{k|k-1} = F\mathbf{x}_{k-1|k-1} + B\mathbf{u}_{k-1} \quad (4.11a)$$

$$P_{k|k-1} = FP_{k-1|k-1}F^T + GQ_kG^T. \quad (4.11b)$$

The correction step, or measurement update, reads:

$$S_k = HP_{k|k-1}H^T + R_k, \quad (4.12a)$$

$$K_k = P_{k|k-1}H^T S_k^{-1}, \quad (4.12b)$$

$$\mathbf{x}_{k|k} = \mathbf{x}_{k|k-1} + K_k(\mathbf{y}_k - H\mathbf{x}_{k|k-1}), \quad (4.12c)$$

$$P_{k|k} = P_{k|k-1} - K_kHP_{k|k-1}, \quad (4.12d)$$

in which  $\mathbf{y}_k - H\mathbf{x}_{k|k-1}$  is the measurement residual and is known as the innovation,  $S_k$  is the innovation covariance,  $K_k$  is the Kalman gain and  $\mathbf{x}_{k|k}$  is the updated state estimate with corresponding covariance  $P_{k|k}$ . Note that, although typically used alternating, each step may be applied several times in succession. For example the prediction step may be applied more than once when no measurement is taken, and when multiple measurements are available at the same time, the correction step may be applied several times in succession.

#### Null space Kalman filter

The set of Equations (4.12) is only applicable if the state covariance  $P$  is positive definite and thus invertible. When the considered system has to satisfy

---

<sup>1</sup>The format  $\mathbf{x}_{k|l}$  represents the estimate of  $\mathbf{x}$  at time  $k$  given all information until time  $l$ .

constraints, there is no uncertainty in the directions perpendicular to these constraints. An example of constraints a system needs to satisfy is invariants that are present when a non-minimal coordinate system is used. For example when using Cartesian coordinates to model a simple pendulum rather than angular coordinates. At a moment when the pendulum is in a vertical downward attitude, there is only uncertainty on the position of the pendulum in the horizontal direction, and the vertical position is perfectly known. At every time there is only uncertainty in the direction tangential to the pendulum.

If the constraint function reads

$$D\mathbf{x} = \mathbf{d}, \quad (4.13)$$

the lack of uncertainty in certain directions means that the null space of  $P$  contains the components of the transpose of  $D$ . This forms a problem in the measurement update formula of the standard Kalman filter, since it requires the inverse of  $P$ . To overcome this problem, instead of working in the full space, we can work in the null space of  $D$ , as is e.g. proposed in [53]. If at a certain time point  $k$  we have a state estimate  $\mathbf{x}_{k|k-1}$  that satisfies the constraints, adding an increment  $\Delta\mathbf{x}_k$  to  $\mathbf{x}_{k|k-1}$  to obtain  $\mathbf{x}_{k|k}$  may result in the constraints being violated. If however  $\Delta\mathbf{x}_k$  lies in the null space of  $D$ ,  $\mathbf{x}_{k|k-1} + \Delta\mathbf{x}_k$  also satisfies the constraint. If we call  $Z$  a null space of  $D$ , we can express  $\Delta\mathbf{x}_k$  as:

$$\Delta\mathbf{x}_k = Z\Delta\mathbf{z}_k, \quad (4.14)$$

with  $\Delta\mathbf{z}_k$  an increment in the null space. To alter the Kalman filter equations to update  $\mathbf{x}_{k|k-1}$  with covariance  $P_{\mathbf{x}_{k|k-1}}$  with measurement  $\mathbf{y}_k$  to work in the null space of  $D$ , we first split  $\mathbf{x}_{k|k-1}$  into a part that is spanned by  $D$  and a part that is spanned by  $Z$ :

$$\mathbf{z}_{k|k-1} = Z^+ \mathbf{x}_{k|k-1}, \quad (4.15a)$$

$$\bar{\mathbf{x}}_{k|k-1} = \mathbf{x}_{k|k-1} - Z\mathbf{z}_{k|k-1}, \quad (4.15b)$$

in which  $Z^+$  denotes the pseudo-inverse of  $Z$ . Figure 4.1 graphically represents these steps for a system where the state is constrained on a line. Because of the invariants, there is no uncertainty in the direction of  $D$  and all uncertainty lies in the directions perpendicular to the space spanned by  $D$ , called the null space of  $D$ . There is thus no uncertainty on  $\bar{\mathbf{x}}_{k|k-1}$  and all uncertainty is on  $\mathbf{z}_{k|k-1}$ . The covariance of  $\mathbf{z}_{k|k-1}$  is given by:

$$P_{\mathbf{z}_{k|k-1}} = \mathbb{E}(\mathbf{z}_{k|k-1}\mathbf{z}_{k|k-1}^T) = \mathbb{E}(Z^+ \mathbf{x}_{k|k-1} \mathbf{x}_{k|k-1}^T Z^{+T}) = Z^+ P_{\mathbf{x}_{k|k-1}} Z^{+T}. \quad (4.16)$$

The innovation covariance is now computed as:

$$S_k = H Z P_{\mathbf{z}_{k|k-1}} (HZ)^T + R_k, \quad (4.17)$$

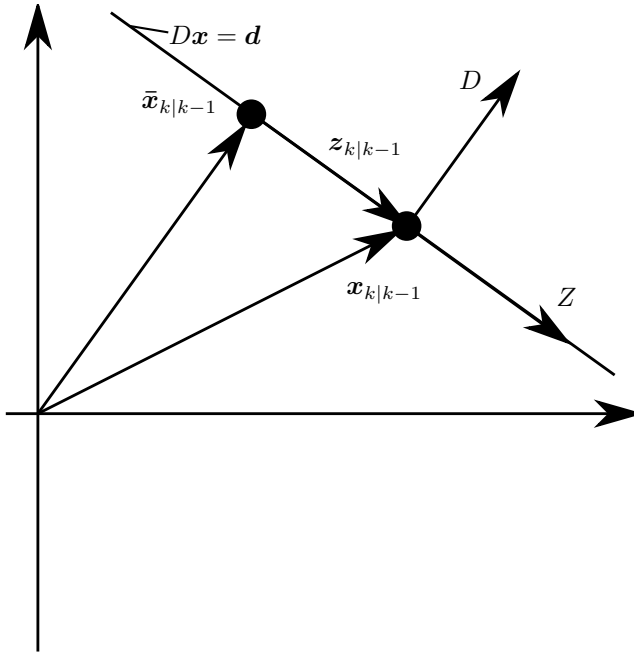


Figure 4.1: Graphical representation of null space decomposition.

and the Kalman gain in the null space is given by:

$$K_k = P_{z_{k|k-1}} (ZH)^T S_k^{-1}. \quad (4.18)$$

$z_{k|k-1}$  can now be updated with measurement  $y_k$ :

$$z_{k|k} = z_{k|k-1} + K_k (y_k - H x_{k|k-1}). \quad (4.19)$$

We also update the covariance in the null space:

$$P_{z_{k|k}} = P_{z_{k|k-1}} - K_k H Z P_{z_{k|k-1}}. \quad (4.20)$$

$z_{k|k}$  is now added to  $\bar{x}_{k|k-1}$  to update the state in the full space:

$$x_{k|k} = \bar{x}_{k|k-1} + Z z_{k|k}, \quad (4.21)$$

and we project the covariance back to the full space:

$$P_{x_{k|k}} = Z P_{z_{k|k}} Z^T. \quad (4.22)$$

#### 4.4.2 Extended Kalman filter

In case the system or measurement model is nonlinear, the standard Kalman filter formulation cannot be used. Suppose the system model is given by:

$$\mathbf{x}_k = \mathbf{F}(\mathbf{x}_{k-1}, \mathbf{u}_{k-1}, \mathbf{w}_{k-1}), \quad (4.23)$$

and the measurement model is given by:

$$\mathbf{y}_k = \mathbf{h}(\mathbf{x}_k) + \mathbf{v}_k. \quad (4.24)$$

The extended Kalman filter is a nonlinear version of the Kalman filter that linearises the nonlinear models around the current state estimate. It uses the linearisation to propagate a linear approximation of the error covariance. The normal Kalman filter equations for the state update are modified to:

$$\mathbf{x}_{k|k-1} = \mathbf{F}(\mathbf{x}_{k-1|k-1}, \mathbf{u}_{k-1}), \quad (4.25a)$$

$$P_{k|k-1} = F_k P_{k-1|k-1} F_k^T + G_k Q_k G_k^T, \quad (4.25b)$$

with  $F_k = \frac{\partial \mathbf{F}}{\partial \mathbf{x}}(\mathbf{x}_{k-1|k-1}, \mathbf{u}_{k-1}, 0)$  and  $G_k = \frac{\partial \mathbf{F}}{\partial \mathbf{w}}(\mathbf{x}_{k-1|k-1}, \mathbf{u}_{k-1}, 0)$ . The correction step, or measurement update, is modified as:

$$S_k = H_k P_{k|k-1} H_k^T + R_k, \quad (4.26a)$$

$$K_k = P_{k|k-1} H_k^T S_k^{-1}, \quad (4.26b)$$

$$\mathbf{x}_{k|k} = \mathbf{x}_{k|k-1} + K_k (\mathbf{y}_k - \mathbf{h}(\mathbf{x}_{k|k-1})), \quad (4.26c)$$

$$P_{k|k} = P_{k|k-1} - K_k H_k P_{k|k-1}, \quad (4.26d)$$

with  $H_k = \frac{\partial \mathbf{h}}{\partial \mathbf{x}}(\mathbf{x}_{k-1|k-1})$ .

#### Null space extended Kalman filter

When a nonlinear invariant  $\mathbf{d}(\mathbf{x}) = \mathbf{0}$  is present in the system, Equations (4.14)–(4.22) can be modified to use the linearisation of the invariant.  $D$  in Equation (4.13) is replaced by  $D_k = \frac{\partial \mathbf{d}}{\partial \mathbf{x}}(\mathbf{x}_{k|k-1})$  and  $\mathbf{d}$  from Equation (4.13) is replaced by  $\mathbf{d}_k = -\mathbf{d}(\mathbf{x}_{k|k-1})$  (the minus sign is needed because  $\mathbf{d}$  is on the right-hand-side in Equation (4.13)). Note that, because in this case the state update happens in the linearised constraint, the nonlinear constraint may be violated after the state has been updated. It is therefore advisable to reproject the state to the constraint function by solving the problem:

$$\begin{aligned} & \underset{\bar{\mathbf{x}}}{\text{minimise}} && \|\mathbf{x}_k - \bar{\mathbf{x}}_k\|_2^2 \\ & \text{subject to} && \mathbf{d}(\bar{\mathbf{x}}_k) = \mathbf{0}, \end{aligned} \quad (4.27)$$

which finds the closest point  $\bar{\mathbf{x}}_k$  to the updated state  $\mathbf{x}_k$  that satisfies the constraint. Solving Problem (4.27) to full convergence may not be desirable and performing one (or multiple) steps of the linearised problem given by

$$\begin{aligned} \text{minimise}_{\bar{\mathbf{x}}} \quad & \| \mathbf{x}_k - \bar{\mathbf{x}}_k \|_2^2 \\ \text{subject to} \quad & D_k(\bar{\mathbf{x}}_k - \mathbf{x}_k) + \mathbf{d}_k = \mathbf{0}, \end{aligned} \quad (4.28)$$

may be better suited. Problem (4.28) can be explicitly written as:

$$\bar{\mathbf{x}}_k = \mathbf{x}_k - D_k^T (D_k D_k^T)^{-1} \mathbf{d}_k, \quad (4.29)$$

which can be applied several times in a row to reproject the updated state estimate to the constraint manifold. Note that for each step the constraint function has to be relinearised.

#### 4.4.3 Unscented Kalman filter

When the system and measurement models are highly nonlinear, the EKF can give poor estimation performance and it may even diverge for some systems, see e.g. [51]. This is because the covariance is propagated through the linearised models. The UKF addresses this problem by using a deterministic sampling approach in which the covariance is propagated by means of a set of carefully chosen sigma points, which capture the true mean and covariance of the state. The sigma points are independently propagated through the nonlinear models. The propagated and updated covariance matrices are then computed from the updated sigma points. The UKF is capable of estimating the posterior means and covariance matrices accurately to a high order [96].

To select the sigma points, the state and covariance estimates are augmented with the mean and covariance of the process noise:

$$\mathbf{x}_{k-1|k-1}^a = \begin{bmatrix} \mathbf{x}_{k-1|k-1}^T & \mathbb{E}[\mathbf{w}_{k-1}^T] \end{bmatrix}^T, \quad (4.30a)$$

$$P_{k-1|k-1}^a = \begin{bmatrix} P_{k-1|k-1} & 0 \\ 0 & Q_k \end{bmatrix}, \quad (4.30b)$$

where the mean of the process noise  $\mathbb{E}[\mathbf{w}_{k-1}]$  is usually zero. A set of  $2L_p + 1$  sigma points is derived from the augmented state and covariance with  $L_p = 2(n_x + n_w) + 1$ , in which  $n_x$  is the dimension of the state vector  $\mathbf{x}$  and  $n_w$  the

dimension of the process noise  $\mathbf{w}$ :

$$\boldsymbol{\chi}_{k-1|k-1}^0 = \mathbf{x}_{k-1|k-1}^a, \quad (4.31a)$$

$$\boldsymbol{\chi}_{k-1|k-1}^i = \mathbf{x}_{k-1|k-1}^a + \left( \sqrt{(L_p + \lambda) P_{k-1|k-1}^a} \right)_i, \quad i = 1, \dots, L_p, \quad (4.31b)$$

$$\boldsymbol{\chi}_{k-1|k-1}^i = \mathbf{x}_{k-1|k-1}^a - \left( \sqrt{(L_p + \lambda) P_{k-1|k-1}^a} \right)_i, \quad i = L_p + 1, \dots, 2L_p, \quad (4.31c)$$

with  $(\sqrt{A})_i$  the  $i$ th column of the square root matrix of  $A$  which can be computed using a blocked Schur Algorithm [24]. The time update equations of the UKF are as follows [96]:

$$\boldsymbol{\chi}_{k|k-1}^i = \mathbf{F}(\boldsymbol{\chi}_{k-1|k-1}^{i,x}, \mathbf{u}_{k-1}, \boldsymbol{\chi}_{k-1|k-1}^{i,w}), \quad i = 0, \dots, 2L_p, \quad (4.32a)$$

$$\mathbf{x}_{k|k-1} = \sum_{i=0}^{2L_p} W_s^i \boldsymbol{\chi}_{k|k-1}^i, \quad (4.32b)$$

$$P_{k|k-1} = \sum_{i=0}^{2L_p} W_c^i [\boldsymbol{\chi}_{k|k-1}^i - \mathbf{x}_{k|k-1}] [\boldsymbol{\chi}_{k|k-1}^i - \mathbf{x}_{k|k-1}]^T, \quad (4.32c)$$

where  $\boldsymbol{\chi}_{k-1|k-1}^{i,x}$  and  $\boldsymbol{\chi}_{k-1|k-1}^{i,w}$  are the first  $n_x$  and last  $n_w$  components of  $\boldsymbol{\chi}_{k-1|k-1}^i$  respectively.

For the measurement update, the state is augmented as:

$$\mathbf{x}_{k|k-1}^a = \begin{bmatrix} \mathbf{x}_{k|k-1}^T & \mathbb{E}[\mathbf{v}_{k-1}^T] \end{bmatrix}^T, \quad (4.33a)$$

$$P_{k|k-1}^a = \begin{bmatrix} P_{k|k-1} & 0 \\ 0 & R_k \end{bmatrix}. \quad (4.33b)$$

Similarly to the state propagation, a set of  $2L_u + 1$  is derived from the augmented state and covariance, with  $L_u = n_x + n_v$  in which  $n_v$  is the dimension of the measurement noise:

$$\boldsymbol{\chi}_{k|k-1}^0 = \mathbf{x}_{k|k-1}^a, \quad (4.34a)$$

$$\boldsymbol{\chi}_{k|k-1}^i = \mathbf{x}_{k|k-1}^a + \left( \sqrt{(L_u + \lambda) P_{k|k-1}^a} \right)_i, \quad i = 1, \dots, L_u, \quad (4.34b)$$

$$\boldsymbol{\chi}_{k|k-1}^i = \mathbf{x}_{k|k-1}^a - \left( \sqrt{(L_u + \lambda) P_{k|k-1}^a} \right)_i, \quad i = L_u + 1, \dots, 2L_u, \quad (4.34c)$$

and the measurement update equations read as [96]:

$$\boldsymbol{\gamma}_k^i = \mathbf{h}(\boldsymbol{\chi}_{k|k-1}^{i,x}) + \boldsymbol{\chi}_{k|k-1}^{i,v}, \quad (4.35a)$$

$$\bar{\mathbf{y}}_k = \sum_{k=0}^{2L_u} W_s^i \boldsymbol{\gamma}_k^i, \quad (4.35b)$$

$$P_{y_k y_k} = \sum_{k=0}^{2L_u} W_c^i [\boldsymbol{\gamma}_k^i - \bar{\mathbf{y}}_k] [\boldsymbol{\gamma}_k^i - \bar{\mathbf{y}}_k]^T, \quad (4.35c)$$

$$P_{x_k y_k} = \sum_{k=0}^{2L_u} W_c^i [\boldsymbol{\chi}_{k|k-1}^i - \mathbf{x}_{k|k-1}] [\boldsymbol{\gamma}_k^i - \bar{\mathbf{y}}_k]^T, \quad (4.35d)$$

$$K_k = P_{x_k y_k} P_{y_k y_k}^{-1}, \quad (4.35e)$$

$$\mathbf{x}_{k|k} = \mathbf{x}_{k|k-1} + K_k (\mathbf{y}_k - \bar{\mathbf{y}}_k), \quad (4.35f)$$

$$P_{k|k} = P_{k|k-1} - K_k P_{z_k z_k} K_k^T, \quad (4.35g)$$

in which  $\boldsymbol{\chi}_{k|k-1}^{i,v}$  denotes the last  $n_v$  components of  $\boldsymbol{\chi}_{k|k-1}^i$ .

The weights  $W_c$  and  $W_s$  in Equations (4.32) and (4.35) are defined as:

$$W_s^0 = \frac{\lambda}{L + \lambda}, \quad (4.36a)$$

$$W_c^0 = \frac{\lambda}{L + \lambda} + (1 - \alpha^2 + \beta), \quad (4.36b)$$

$$W_s^i = W_c^i = \frac{1}{2(L + \lambda)}, \quad (4.36c)$$

in which  $\lambda = \alpha^2(L + \kappa)$  is a scaling parameter, with  $L$  replaced by  $L_p$  and  $L_u$  accordingly. The spread of the sigma points is determined by  $\alpha$  which is usually set to a small positive value, e.g.  $10^{-3}$ ,  $\kappa$  is a secondary scaling factor that is usually set to 0 and  $\beta$  is used to incorporate prior information on the distribution of  $\mathbf{x}$  and is optimally 2 for Gaussian distributions [96].

### Null space unscented Kalman filter

Similar to the standard Kalman filter, the propagation and measurement update steps can be used independently and one of the steps may be applied several times in a row.

When the system has to satisfy constraints, and in particular when invariants are present in the model, we can select the sigma points in the null space of the Jacobian of the constraint, similar to what is done in the Null space Kalman filter. For the time update, the sigma points are calculated as follows:

$$\mathbf{z}_{k-1|k-1} = Z_k^+ \mathbf{x}_{k-1|k-1}, \quad (4.37a)$$

$$\bar{\mathbf{x}}_{k-1|k-1} = \mathbf{x}_{k-1|k-1} - Z_k \mathbf{z}_{k-1|k-1}, \quad (4.37b)$$

$$\mathbf{z}_{k-1|k-1}^a = Z_k^+ \mathbf{x}_{k-1|k-1}, \quad (4.37c)$$

$$\mathbf{z}_{k-1|k-1}^a = \begin{bmatrix} \mathbf{z}_{k-1|k-1}^T & \mathbb{E}[\mathbf{w}_{k-1}^T] \end{bmatrix}^T, \quad (4.37d)$$

$$P_{z_{k-1|k-1}}^a = \begin{bmatrix} Z_k^+ P_{k-1|k-1} Z_k^{+T} & 0 \\ 0 & Q_k \end{bmatrix}, \quad (4.37e)$$

$$\boldsymbol{\chi}_{z_{k-1|k-1}}^0 = \mathbf{z}_{k-1|k-1}^a, \quad (4.37f)$$

$$\boldsymbol{\chi}_{z_{k-1|k-1}}^i = \mathbf{z}_{k-1|k-1}^a + \left( \sqrt{(L_z + \lambda) P_{z_{k-1|k-1}}^a} \right)_i, \quad i = 1, \dots, L_z, \quad (4.37g)$$

$$\boldsymbol{\chi}_{z_{k-1|k-1}}^i = \mathbf{z}_{k-1|k-1}^a - \left( \sqrt{(L_z + \lambda) P_{z_{k-1|k-1}}^a} \right)_i, \quad i = L_z + 1, \dots, 2L_z, \quad (4.37h)$$

with  $Z$  a null space of the Jacobian of the constraint function and  $L_z = n_z + n_w$  with  $n_z$  the dimension of  $\mathbf{z}$ . These null space sigma points are projected onto the full space:

$$\boldsymbol{\chi}_{k-1|k-1}^i = \bar{\mathbf{x}}_{k-1|k-1} + Z_k \boldsymbol{\chi}_{z_{k-1|k-1}}^i, \quad (4.38)$$

and the normal update formulas (4.32) can be applied. For the measurement update, the sigma points can similarly be selected in the null space. Note that because the Jacobian of the constraint function is needed, this form of UKF is no longer derivative free.

## 4.5 Moving Horizon Estimation

All of the Kalman filters described in Section 4.4 estimate the state based on the propagation of a Gaussian random variable. For nonlinear systems, this propagation is based on an approximation, resulting in a suboptimal state estimate. This propagation of a Gaussian random variable is not present in the full information problem discussed in Section 4.3. However, the computational

burden of solving the full information problem grows as more measurements become available. A technique known as moving horizon estimation solves the computational burden of the full information problem by considering only a finite number of the most recent measurements.

### 4.5.1 Problem formulation

In moving horizon estimation the state estimate is determined by considering only a finite horizon of the latest  $T$  seconds. When a new measurement arrives, the horizon is shifted and the new problem is formulated and solved again to determine the new estimate of the state. An MHE problem for a system with Gaussian noise is typically formulated as the following optimal control problem (OCP):

$$\begin{aligned} \text{minimise}_{\mathbf{x}(\cdot), \mathbf{w}(\cdot), \mathbf{v}(\cdot)} \quad & \| \mathbf{x}(t_c - T) - \bar{\mathbf{x}}_a \|_{P_a^{-1}}^2 + \\ & \int_{t_c - T}^{t_c} \| \mathbf{w}(t) \|_{Q(t)^{-1}}^2 dt + \int_{t_c - T}^{t_c} \| \mathbf{v}(t) \|_{R(t)^{-1}}^2 dt \quad (4.39) \\ \text{subject to} \quad & \mathbf{0} = \mathbf{f}(\mathbf{x}(t), \dot{\mathbf{x}}(t), \mathbf{u}(t), \mathbf{w}(t)), \\ & \mathbf{y}(t) = \mathbf{h}(\mathbf{x}(t), \mathbf{v}(t)), \end{aligned}$$

to yield the optimal trajectories  $\mathbf{x}(t)$ ,  $\mathbf{v}(t)$  and  $\mathbf{w}(t)$  over the estimation horizon from time  $t_c - T$  to the current time  $t_c$ , with  $T$  the length of the estimation horizon. The first term in Problem (4.39) is the arrival cost, which summarises all information prior to the horizon in  $\bar{\mathbf{x}}_a$  and is weighted through the covariance matrix  $P_a$ . The second term is the cost related to the process noise  $\mathbf{w}(t)$  weighted with covariance matrix  $Q(t)$  and the third term the cost related to the measurement noise  $\mathbf{v}(t)$  weighted with covariance matrix  $R(t)$ . Figure 4.2 illustrates the MHE approach for a simple system. In a typical closed loop system, the measurements come at discrete sampling times, and the controls are applied on the same sampling times. Therefore Problem (4.39) can be discretised with a multiple shooting discretisation [8] as:

$$\begin{aligned} \text{minimise}_{\mathbf{x}, \mathbf{w}, \mathbf{v}} \quad & \| \mathbf{x}_{N_c - N} - \bar{\mathbf{x}}_a \|_{P_a^{-1}}^2 + \sum_{k=N_c - N}^{N_c - 1} \| \mathbf{w}_k \|_{Q_k^{-1}}^2 + \sum_{k=N_c - N}^{N_c} \| \mathbf{v}_k \|_{R_k^{-1}}^2 \\ \text{subject to} \quad & \mathbf{x}_{k+1} = \mathbf{F}(\mathbf{x}_k, \mathbf{u}_k, \mathbf{w}_k), \\ & \mathbf{y}_k = \mathbf{h}(\mathbf{x}_k, \mathbf{v}_k), \quad (4.40) \end{aligned}$$

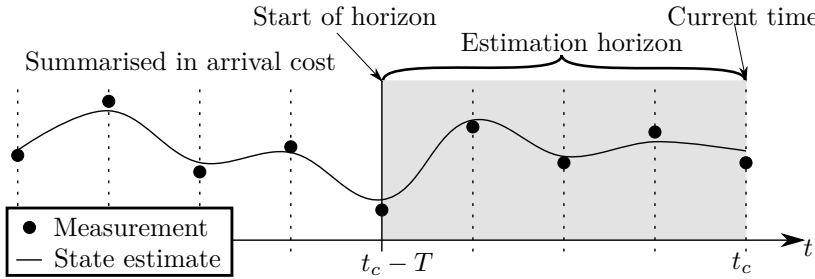


Figure 4.2: Illustration of MHE for system with one state and measurements of that state.

in which  $\mathbf{x}_k$  is the state at time  $kT_s$  with  $T_s$  the sampling time and  $N_c T_s = t_c$ , the current time.  $N = \frac{T}{T_s}$  is the horizon length. The number of optimisation variables in Problem (4.40) is equal to  $n_o = (N + 1)(n_x + n_v) + Nn_w$

### 4.5.2 Solution method

The complexity of problem (4.40) makes it hard to meet the stringent real time requirements needed for estimation and control of fast mechanical systems. Solving problem (4.40) using a generic-purpose OCP solver requires an iterative procedure. By the time the solver has reached convergence, the state estimate may be irrelevant.

Given the specific least squares structure of the objective function, Problem (4.40) can be efficiently solved by means of the real time iteration (RTI) scheme with Gauss-Newton Hessian approximation [26], which is implemented in the ACADO Code Generation Tool [94].

In the real time iteration scheme, only a single full Newton-type iteration per sampling time is performed. The solution of this single step is then used to initialise the problem on the next sampling time. The state is thus estimated as the optimiser converges such that low sampling times are possible. To limit the latency, the time between the point at which the measurement is taken and the state estimate is provided, the problem is split into a '*preparation phase*' and a '*feedback phase*'. In the preparation step, which is performed before the measurement is available, the most computationally expensive operations such as integrating the system together with computing the sensitivities and condensing of the problem are performed. After the measurement becomes available, the feedback step is performed, which only consists of solving the condensed QP. The RTI scheme is described in more detail in [27, 26, 57]. The

philosophy behind this strategy is that is better to provide an approximate solution to Problem (4.40) shortly after the measurement is taken than to wait until the solver converges.

Stability of the RTI scheme assumes the shifting of the horizon introduces sufficiently small disturbances to the optimisation procedure [28]. The last shooting node can be initialised simulating the system over the last interval using the control input sent to the system.

The ACADO Code Generation Tool implements the real time iteration scheme. The tool exports C code tailored for a specific problem. It exploits problem structure and dimensions together with sparsity patterns to remove all unnecessary computations and remove the need for dynamic memory allocation [57, 37, 39, 94].

### 4.5.3 Benefits of MHE

For linear systems with Gaussian noise, MHE provides the same state estimates as the Kalman filter. For nonlinear systems however, MHE may provide faster convergence and better estimation performance compared to EKF, see e.g. [51] and Chapter 6 of this thesis.

Another benefit of MHE is that other than Gaussian distributions can be handled by using appropriate norms in the objective function. For example, Chapter 5 uses the Huber penalty function to provide robustness against outliers in the measurements.

While a null space method is needed for the Kalman filter and its variants to handle constraints such as model invariants, this is not needed for MHE since it can directly incorporate these constraints in the formulation. Physical constraints on the state and possibly on parameters can also be imposed.

The main benefit of the recursive state estimation techniques is the lower computational cost, but both algorithmic advances and faster computers are making MHE more competitive and real time feasible, even for complex nonlinear models such as those of an AWE system, as Chapter 6 shows.

## 4.6 Conclusion

This chapter presented two classes of state estimators suitable for real time applications: the recursive approaches such as the Kalman filter and different variants of it, discussed in Section 4.4 and the moving horizon estimation,

discussed in Section 4.5. Implementation issues and (dis)advantages of the approaches are discussed. This chapter serves as background information for Chapter 5 and Chapter 6, in which the application and validation of state estimation based on EKF, UKF and MHE for real time estimation of the position and orientation of the aeroplane on the indoors carousel is discussed in detail.

# Chapter 5

## Moving horizon estimation with a kinematic model

### 5.1 Introduction

This chapter is based on [48]. It presents a Moving Horizon Estimator (MHE) that robustly fuses the IMU measurements with the camera measurements using a kinematic model. The IMU provides measurements of linear acceleration and angular velocity. Since these quantities are measured in the coordinate frame of the aeroplane and need some previous estimate of the aeroplane's position and orientation, we describe these measurements as *relative measurements*.

While the cameras provide *absolute measurements* of the aeroplane's position and orientation that are easily related to the world coordinate frame, the camera measurements are captured at a much lower frequency than the IMU measurements and, alone, are not fast enough to directly capture the dynamics of the system. Furthermore, the vision system has the potential to be influenced by illumination and objects in the scene and may occasionally produce faulty measurements (or *outliers*).

Algorithms based on extended and unscented Kalman filters, particle filters<sup>1</sup> and MHEs have been developed to fuse IMU measurements with absolute

---

<sup>1</sup>The particle filter is an estimation technique that does not need any assumptions on the disturbance probability distributions, but instead approximates the probability distributions via Monte Carlo sampling. Its major drawback is the curse of dimensionality, making it only suited for systems with a small state space.

measurements to estimate position and orientation [69, 15, 80, 19]. In particular, [44] applied the extended Kalman filter to the system considered in this thesis. This Kalman filter is used as the baseline to compare the results obtained in this chapter. Robustness of the estimator against outliers in the absolute measurements is obtained using appropriate penalty functions. To limit the number of optimisation variables, the IMU measurements in the intervals between camera frames are modelled as samples of a superposition of orthonormal polynomial basis functions.

This chapter is organised as follows: Section 5.2 presents a kinematic model of the system, Section 5.3 presents the measurement models for the stereo vision system, Section 5.4 describes the estimation problem, Section 5.5 shows how to discretise the problem, Section 5.6 introduces least-squares and robust MHE formulations, Section 5.7 and Section 5.8 show simulation and experimental results respectively, and Section 5.9 concludes the chapter. All results in this chapter are obtained using the tool CasADi.

## 5.2 Kinematic model for AWE system

### 5.2.1 State definition

To define the system state, we start with defining the frames in space that are used to represent the state of the system. Then the state definition is given. Figure 5.1 illustrates the frame definitions given below.

The **world frame** is a right-handed inertial frame that is fixed to the static part of the carousel. The origin lies on the intersection of the axis of rotation of the carousel and the ground on which the setup stands. The  $x$ -axis is aligned with the mean wind vector. If there is no wind, like in the indoor-setup, the orientation of the  $x$ -axis is chosen arbitrarily. The  $z$ -axis points down and is aligned with the main shaft of the carousel.

The **carousel frame** is located at the top of the carousel, at the same height as the top of the arm and it rotates together with the carousel. Its  $z$ -axis is aligned with the  $z$ -axis of the world frame. Its  $x$ -axis is aligned with the arm. The angle between the  $x$ -axis of the carousel frame and the  $x$ -axis of the world frame is denoted by  $\delta$ .  $\dot{\delta}$  denotes the angular velocity of the carousel frame with respect to the world frame.

The **arm frame** has the same orientation as the carousel frame but its origin coincides with the tether attachment point on the carousel at a distance  $r_{\text{Arm}}$  from the carousel frame. The  $x$ -axis points radially outwards.

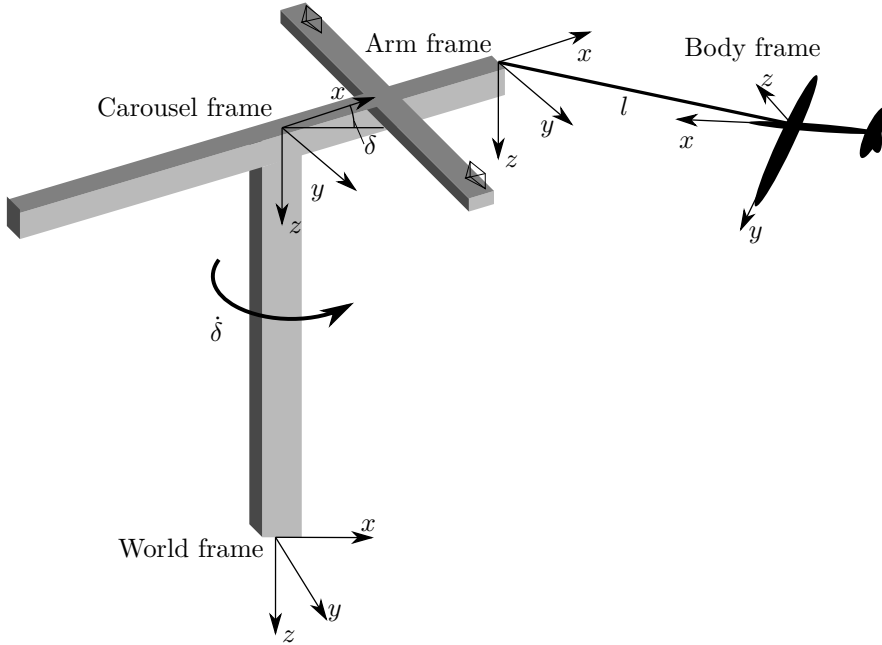


Figure 5.1: Frame definitions.

The **body frame** is attached to the aeroplane according to the north-east-down convention<sup>2</sup>, with the  $x$ -axis pointing forward and the  $z$ -axis pointing down with respect to the aeroplane, perpendicular to the bottom plane of the aeroplane. Its origin coincides with the centre of mass of the aeroplane.

The **IMU frame**, not shown in Figure 5.1, is attached to the IMU that is mounted inside the aeroplane. The rotation matrix that transfers vectors from the IMU frame to body frame coordinates is denoted by  $R_{\text{IMU}}$ .

A complete overview of the state and control vector of the kinematic model is given in Table 5.1 and Table 5.2 respectively. A more detailed description of some of the components is given below.

The position of the aeroplane is defined as the position of its centre of mass expressed in the arm frame. Several options are available. In [45] it is proposed to use spherical coordinates in the arm frame to define the position of the aeroplane. In [49] however, the proposal is made to use natural coordinates

<sup>2</sup>In the north-east-down convention, the  $x$ -axis points forward (north), the  $y$ -axis points to the right of the aeroplane (east) and the  $z$ -axis points down.

State variable	Defines	unit
$r$	Position of aeroplane in arm frame	m
$\dot{r}$	Velocity of aeroplane w.r.t. arm frame	$\frac{m}{s}$
$q$	Quaternion that represents orientation of aeroplane w.r.t. arm frame	—
$\delta$	Carousel angle	rad
$\ddot{\delta}$	Angular velocity of carousel	$\frac{rad}{s}$

Table 5.1: State definition for kinematic model.

Control variable	Defines	unit
$a_{IMU}$	Acceleration of the aeroplane measured by the IMU	$\frac{m}{s^2}$
$\omega_{IMU}$	Angular velocity of the aeroplane measured by the IMU	$\frac{rad}{s}$
$\ddot{\delta}$	Angular acceleration of carousel	$\frac{rad}{s^2}$

Table 5.2: Control definition for kinematic model.

by using Cartesian coordinates  $r = [x \ y \ z]^T$  in the arm frame to define the position of the aeroplane. Similarly, the velocity of the aeroplane is also expressed in Cartesian coordinates as the velocity of the aeroplane with respect to the arm frame.

The orientation of the aeroplane is defined as the orientation of the body frame with respect to the arm frame, expressed in the arm frame. Again, several options are possible. Most commonly used are a set of Euler angles and in particular roll-pitch-yaw angles when it comes to modelling flight dynamics. However, any representation of orientation based on Euler angles has singularities. For an AWE system where all orientations are likely to be visited this adds extra difficulties. The most popular, non-singular, representation of the orientation is the quaternion  $q$  and is used for the kinematic model in this chapter. The quaternion uses 4 elements to represent orientation and it is defined as  $q = [q_1 \ q_2 \ q_3 \ q_4]^T = [e_x \sin(\theta) \ e_y \sin(\theta) \ e_z \sin(\theta) \ \cos(\theta)]^T$  where  $[e_x, e_y, e_z]^T$  and  $\theta$  are the Euler axis and angle of rotation that represent the orientation of the body frame with respect to the arm frame. It is clear that the quaternion should satisfy the constraint  $\|q\|_2^2 = 1$ . An overview of the definition and use of quaternions can be found in [69].

The angular velocity of the aeroplane  $\omega$  is the angular velocity vector of the body frame with respect to the world frame, expressed in arm frame coordinates. The angular velocity of the aeroplane is not considered as part of the state vector in the kinematic model. Instead, the angular velocity measurement from the IMU is used as an input to the model. The acceleration of the aeroplane as measured by the IMU is also an input to the kinematic model.

In total, the kinematic model has a state vector with size  $n_x = 12$ , of which the 4 components of the quaternion are linked via the unit norm constraint, a control vector of size  $n_u = 7$  and a process noise vector of size  $n_w = 7$ .

### 5.2.2 Model equations

A kinematic model of a system describes the motion of the system without consideration of the causes of this motion. From an estimation perspective, kinematic models can be interesting when a physical model is hard or impossible to obtain. For the system considered in this thesis, the kinematic relation is exact, and is not influenced by unmodelled or neglected dynamics of the system. It further does not depend on any of the system's characteristics such as mass, shape, moments of inertia and aerodynamics of the aeroplane.

When an IMU is available on the system, the measurements of the IMU can be used as an input to the kinematic model to provide updates on a previously known position and orientation. For the system considered in this thesis, the kinematic relation between the acceleration measured by the IMU, and the acceleration of the aeroplane expressed in the arm frame is given by:

$$\ddot{\mathbf{r}} = \text{Rot}(\mathbf{q})R_{\text{IMU}}(\mathbf{a}_{\text{IMU}} - \mathbf{b}_a) + \dot{\delta}^2 \begin{bmatrix} x + r_{\text{Arm}} \\ y \\ 0 \end{bmatrix} - 2\dot{\delta} \begin{bmatrix} -\dot{y} \\ \dot{x} \\ 0 \end{bmatrix} - \ddot{\delta} \begin{bmatrix} -y \\ x + r_{\text{Arm}} \\ 0 \end{bmatrix} + \begin{bmatrix} 0 \\ 0 \\ g \end{bmatrix}, \quad (5.1)$$

in which  $\mathbf{a}_{\text{IMU}}$  is the acceleration measurement of the IMU,  $\mathbf{b}_a$  is the bias on the acceleration measurement,  $\text{Rot}(\mathbf{q})$  is the rotation matrix that depends on the quaternion  $\mathbf{q}$  and describes the transformation from arm frame coordinates to body frame coordinates.  $g$  is the gravitational constant. The kinematic relation between the angular velocity measured by the IMU and time derivative of the quaternion that represents the orientation of the aeroplane is given by:

$$\dot{\mathbf{q}} = \frac{1}{2}\Omega(R_{\text{IMU}}(\boldsymbol{\omega}_{\text{IMU}} - \mathbf{b}_\omega) - \text{Rot}(\mathbf{q})^T [0 \ 0 \ \dot{\delta}]^T)\mathbf{q}, \quad (5.2)$$

with  $\boldsymbol{\omega}_{\text{IMU}}$  the angular velocity measurement of the IMU and  $\mathbf{b}_\omega$  the bias on the angular velocity measurement.  $\Omega(\cdot)$  is the  $4 \times 3$  quaternion matrix, which for a vector  $\mathbf{s} = [s_0 \ s_1 \ s_2]^T$  is given by [13]:

$$\Omega(\mathbf{s}) = \begin{bmatrix} 0 & -s_2 & s_1 \\ s_2 & 0 & -s_0 \\ -s_1 & s_0 & 0 \\ -s_0 & -s_1 & -s_2 \end{bmatrix}. \quad (5.3)$$

Process noise for the kinematic model is considered to be the noise on the IMU measurements and a noise term on  $\ddot{\delta}$ . The noise on the IMU measurements is not process noise in the typical sense, since it is measurement noise. This way of introducing noise into the system is justified since when the IMU measurements are noise-free, the kinematic relation for position and orientation is exact.

### 5.3 Measurement model for stereo vision system

The stereo vision system provides information about the position and orientation of the aeroplane by tracking the position of three markers on the aeroplane in the camera images at a sampling frequency of 12.5 Hz. The measurement function for the camera system is based on a pinhole camera model. The pinhole camera model is a simple model which describes the mathematical relationship between the coordinates of a point in 3D and its projection onto the image plane of an ideal pinhole camera. In a pinhole camera model, the camera aperture is described as a point. No lenses are used to focus light in a pinhole camera. The model does not include, for example, geometric distortions or blurring of unfocused objects caused by lenses and finite sized apertures. Neither does it take into account that most practical cameras have only discrete image coordinates. This means that the pinhole camera model can only be used as a first order approximation of the mapping from a 3D scene to a 2D image. Its validity depends on the quality of the camera and, in general, decreases from the centre of the image to the edges as lens distortion effects increase. The pinhole camera model is given by:

$$\begin{bmatrix} u^* \\ v^* \\ s \end{bmatrix}_{ij} = [P_{c_i}] [R_{c_i}^T] (\mathbf{r}_{c_i} + \mathbf{r}_{m_j}^{\text{ref}}), \quad (5.4)$$

with  $u = u^*/s$  and  $v = v^*/s$  the pixel coordinates of the marker in the camera image,  $s$  the homogeneous scaling factor,  $\mathbf{r}_{m_j}^{\text{ref}}$  the position of marker  $j$  in the arm frame and  $P_{c_i}$  the matrix of intrinsic parameters of camera  $i$  given by:

$$P_{c_i} = \begin{bmatrix} f_x & 0 & c_x \\ 0 & f_y & c_y \\ 0 & 0 & 1 \end{bmatrix}, \quad (5.5)$$

with  $(c_x, c_y)$  the principal point of the camera that is normally at the image centre and  $(f_x, f_y)$  the focal lengths, expressed in pixel-related units. Figure 5.2 clarifies this. If an image from a camera is scaled by some factor, all of these parameters should be scaled by the same factor. The matrix of intrinsic parameters does not depend on the scene viewed and, once estimated, can be

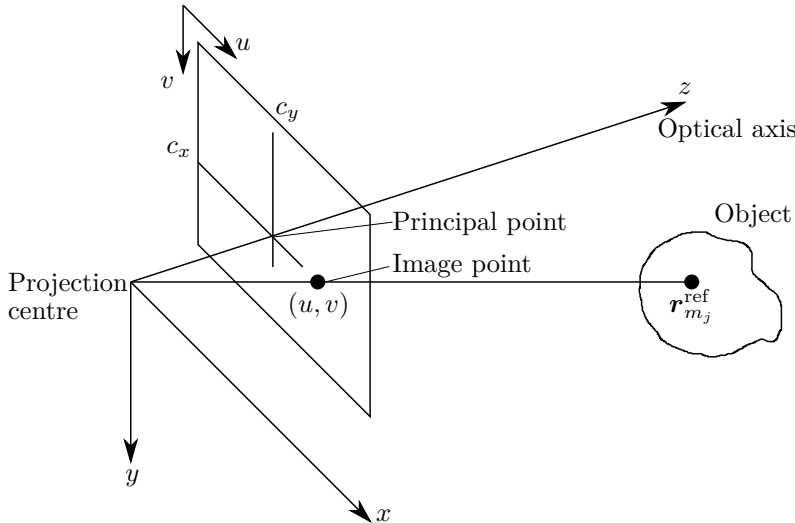


Figure 5.2: Representation of pinhole camera.

re-used, as long as the focal length is fixed, which is not the case when a zoom lens is used.  $\mathbf{r}_{ci}$  is the position of the camera in the arm frame and  $R_{ci}$  is the rotation matrix that transfers camera frame coordinates to body frame coordinates. They are used to describe the camera motion around a static scene, or vice versa, rigid motion of an object in front of a still camera. That is, it transforms coordinates of a point to some coordinate system fixed with respect to the camera. The relationship between the position of marker  $i$  and the position and orientation of the aeroplane in the arm frame is given by:

$$\mathbf{r}_{mj}^{\text{ref}} = \mathbf{r} + R\mathbf{r}_{mj}^{\text{body}}, \quad (5.6)$$

where  $\mathbf{r}_{mj}^{\text{body}}$  is the position of marker  $j$  in the body frame. Equations (5.4) and (5.6) combined give the relation between the pose of the aeroplane and position of a marker in a camera. The camera measurement function can now be written by:

$$\mathbf{y}_{c_{ij}} = \mathbf{h}_{c_{ij}}(\mathbf{x}, \mathbf{v}_{c_{ij}}) = \begin{bmatrix} u \\ v \end{bmatrix} + [\mathbf{v}_{c_{ij}}], \quad (5.7)$$

with  $\mathbf{v}_{c_{ij}}$  the noise on the camera measurement.

The measurement function for the carousel encoder is straightforward since it is a direct measurement of  $\delta$ . The length of the complete measurement vector, and since we consider only additive noise also of the measurement noise vector, is  $n_v = 13$ , consisting of 12 measurements from the stereo vision system (3 markers in 2 camera images), and the carousel encoder measurement.

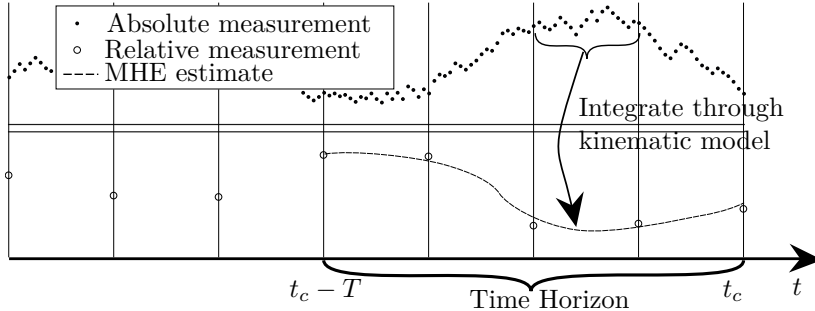


Figure 5.3: Illustration of the measurements.

## 5.4 Estimation problem

To define the estimation problem, we first recapitulate the standard form of a moving horizon estimator, Equation (4.39), but without the arrival cost, and with additive measurement noise  $\mathbf{y}(t) = \mathbf{h}(\mathbf{x}(t)) + \mathbf{v}(t)$  such that  $\mathbf{v}(t)$  can be eliminated from the optimisation variables:

$$\underset{\mathbf{x}(\cdot), \mathbf{w}(\cdot)}{\text{minimise}} \quad \int_{t_c - T}^{t_c} \|\mathbf{w}(t)\|_{Q(t)^{-1}}^2 + \|\mathbf{y}(t) - \mathbf{h}(\mathbf{x}(t))\|_{R(t)^{-1}}^2 dt \quad (5.8)$$

$$\text{subject to } \mathbf{0} = \mathbf{f}(\mathbf{x}(t), \dot{\mathbf{x}}(t), \mathbf{u}(t), \mathbf{w}(t)).$$

The nature of our sensors introduces more complexity into the formulation. The IMU measurements are captured at a sampling rate that is 50 to 100 times higher than the sampling rate of the camera measurements. The standard discretisation method using multiple shooting, as in Problem (4.40), cannot be employed since this introduces too much optimisation variables in the problem. This is different from Kalman filtering methods, where the measurement update can simply be applied whenever a measurement is available. We therefore use a discrete formulation for the camera measurements and a continuous time formulation for the IMU measurements. This is illustrated in Figure 5.3. Also, the statistics of the absolute measurements are far from Gaussian as there probably are outliers due to false marker detections, so we may have to use non-quadratic penalties that better handle these outliers. With these changes,

the optimisation problem to be solved becomes:

$$\begin{aligned}
 \underset{\mathbf{x}(\cdot), \mathbf{w}(\cdot), b}{\text{minimise}} \quad & \sum_{k=N_c-N}^{N_c} \Psi(\mathbf{y}_{\text{abs},k} - \mathbf{h}_{\text{abs}}(\mathbf{x}(t_k))) \\
 & + \sum_{k=N_c-N}^{N_c-1} \int_{t_k}^{t_{k+1}} \| \mathbf{y}_{\text{rel}}(t) - \mathbf{s}(t) \|_{Q(t)^{-1}}^2 dt \\
 & + \| \mathbf{b} - \bar{\mathbf{b}} \|_B^2
 \end{aligned} \tag{5.9}$$

$$\text{subject to } \mathbf{0} = \mathbf{f}(\mathbf{x}(t), \dot{\mathbf{x}}(t), \mathbf{s}(t), \mathbf{b}),$$

$$g(\mathbf{x}(t_c)) = \mathbf{0},$$

where  $\Psi(\cdot)$  is a penalty function,  $\mathbf{s} = [\mathbf{a}, \mathbf{\omega}]^T$  are the estimates of acceleration and angular velocity,  $\mathbf{y}_{\text{rel}} = [\mathbf{a}_{\text{meas}}, \mathbf{\omega}_{\text{meas}}]^T$  are the relative measurements (i.e. coming from the IMU),  $\mathbf{y}_{\text{abs}}$  are the absolute measurements (i.e. the locations of the markers in the images from the stereo vision system),  $N_c$  is the number of measurements taken until the current time  $t_c$ ,  $N$  is the horizon length containing  $N + 1$  absolute measurements,  $Q$  is the covariance matrix of the noise on the relative measurements,  $\mathbf{b} = [\mathbf{b}_a \mathbf{b}_\omega]^T$  is the estimate for the bias on the acceleration and angular velocity measurements,  $\bar{\mathbf{b}}$  is a previous estimate of the bias, and  $B$  is a weighting matrix. The bias  $\mathbf{b}$  is assumed to be constant over the horizon, since the time scale at which it varies is much bigger than the length of the horizon.

The first term in Problem (5.9) is thus the mismatch between the predicted and actual absolute measurements, the second term is the mismatch between the predicted and actual relative measurements, and the last term slows the evolution of the bias estimation. Strategies for updating  $\bar{\mathbf{b}}$  and  $B$  are discussed in e.g. [66] but are not the subject of this chapter. The absolute measurement function  $\mathbf{h}_{\text{abs}}(\mathbf{x})$  is the pinhole camera model discussed in Section 5.3. In the constraints,  $g(\mathbf{x}) = \| \mathbf{q} \|_2^2 - 1$  enforces the quaternion norm constraint at the end of the horizon. The kinematic model ensures that  $\mathbf{q}$  keeps its unit norm throughout the horizon when it has a unit norm at some point in the horizon, which is why it only needs to be enforced on one point in the horizon.

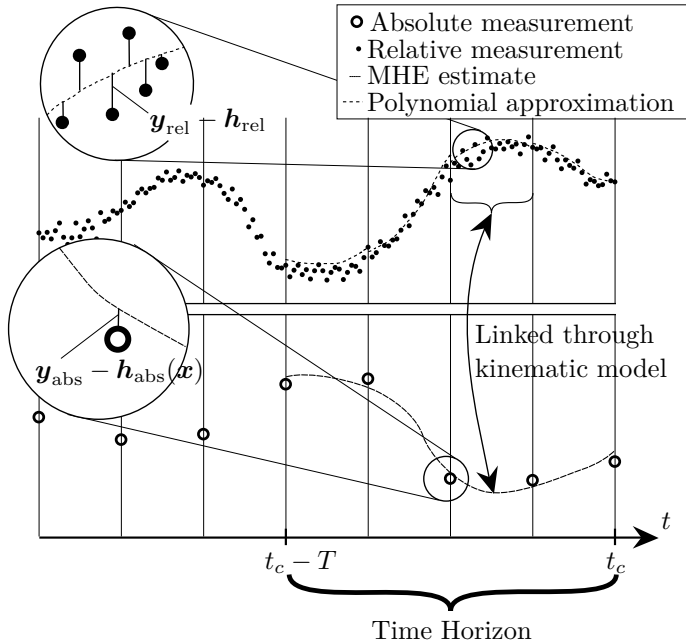


Figure 5.4: The relative measurements are projected on a polynomial basis and then used in MHE. These polynomials are also affected by the absolute measurements through the kinematic model.

## 5.5 Discretisation of continuous problem

Problem (5.9) is still an infinite-dimensional optimal control problem because of the continuous time functions for the IMU measurements. One way to deal with this is to discretise the unknown input  $s$  with the same grid as the actual relative measurements  $y_{\text{rel}}$ . In our context this results in a very large-scale optimisation problem, since the relative measurements are densely sampled.

For this reason, we developed an approach in which the relative measurements are approximated by a polynomial basis of degree  $m$ . Figure 5.4 illustrates this. The polynomial coefficients, denoted by  $p$ , are then the optimisation variables for the optimisation problem. Each set of relative measurements between two absolute pose measurements is represented by a polynomial. In our case, we thus have a polynomial for  $a_x, a_y, a_z, \omega_x, \omega_y$  and  $\omega_z$  for each frame in the horizon. A frame in the context of our MHE formulation is defined to be the window between two absolute measurements. The parameterisation for the

estimates for acceleration and angular velocity in time becomes:

$$\tilde{\mathbf{s}}(t; \mathbf{p}_k) = \begin{bmatrix} \tilde{a}_x(t) \\ \tilde{a}_y(t) \\ \tilde{a}_z(t) \\ \tilde{\omega}_x(t) \\ \tilde{\omega}_y(t) \\ \tilde{\omega}_z(t) \end{bmatrix} = \sum_{i=0}^m L_i(t - t_k) \mathbf{p}_k^{(i)}, \quad (5.10)$$

where  $L_i$  is the polynomial of order  $i$  in the polynomial basis, and  $\mathbf{p}_k^{(i)} = [p_1^{(i)} \ p_2^{(i)} \ p_3^{(i)} \ p_4^{(i)} \ p_5^{(i)} \ p_6^{(i)}]^T$  are the coefficients for the polynomial of order  $i$  for frame  $k$ . The indices  $\{1, \dots, 6\}$  indicate the type of relative measurement (i.e. acceleration or angular velocity in  $x$ ,  $y$  or  $z$  direction).

To discretise  $\mathbf{f}(\mathbf{x}(t), \dot{\mathbf{x}}(t), \mathbf{s}(t), \mathbf{b})$ , we use a multiple shooting parameterisation with multiple shooting nodes on each time where there is an absolute measurement. To go from  $\mathbf{x}(t_k)$  to  $\mathbf{x}(t_{k+1})$ , the kinematic model (5.1–5.2) is numerically integrated using the polynomials for frame  $k$  as input. Note that the integrator can take much larger steps than the sampling rate of the IMU. The state, integrated between two multiple shooting nodes, is denoted by  $\mathbf{F}(\mathbf{x}_k, \mathbf{p}_k, \mathbf{b})$ . The MHE problem thus becomes:

$$\begin{aligned} \text{minimise}_{\mathbf{x}, \mathbf{p}, \mathbf{b}} \quad & \sum_{k=N_c-N}^{N_c} \Psi(\mathbf{y}_{\text{abs},k} - \mathbf{h}_{\text{abs}}(\mathbf{x}_k)) \\ & + \sum_{k=N_c-N}^{N_c-1} \int_{t_k}^{t_{k+1}} \| \tilde{\mathbf{s}}(t - t_k, \mathbf{p}_k) - \mathbf{y}_{\text{rel}}(t) \|_{Q(t)^{-1}}^2 dt \\ & + \| \mathbf{b} - \bar{\mathbf{b}} \|_B^2 \end{aligned} \quad (5.11)$$

subject to  $\mathbf{x}_{k+1} = \mathbf{F}(\mathbf{x}_k, \mathbf{p}_k, \mathbf{b})$ ,

$$g(\mathbf{x}_{N_c}) = 0,$$

where  $\mathbf{p}_k = [\mathbf{p}_k^{(0)T} \ \mathbf{p}_k^{(1)T} \ \dots \ \mathbf{p}_k^{(m)T}]^T$ , a vector of all polynomial coefficients for all IMU measurements of frame  $k$ . In practice, due to the high but finite sampling rate of the IMU, we replace the integrals in the objective function by

sums. The corresponding term in Problem (5.11) becomes:

$$\begin{aligned} & \int_{t_k}^{t_{k+1}} \| \tilde{\mathbf{s}}(t - t_k, \mathbf{p}_k) - \mathbf{y}_{\text{rel}}(t) \|_{Q(t)^{-1}}^2 dt \\ & \approx \sum_{j=0}^{N_{\text{rel}}-1} \| \tilde{\mathbf{s}}(t_k + j\Delta t, \mathbf{p}_k) - \mathbf{y}_{\text{rel}}(t_k + j\Delta t) \|_{Q_k^{-1}}^2, \end{aligned} \quad (5.12)$$

where  $\Delta t$  is the sampling period of the relative measurements and where  $N_{\text{rel}}$  is the number of relative measurements between two absolute measurements.  $Q_k$  is the covariance of each single relative measurement as instructed by the IMU producer. Since the noise of the different components of the IMU measurements are independent,  $Q_k$  is diagonal and constant in time. It can thus be written as:

$$Q_k = \begin{bmatrix} \sigma_1^2 & \cdots & 0 \\ \vdots & \ddots & \vdots \\ 0 & \cdots & \sigma_6^2 \end{bmatrix}. \quad (5.13)$$

We can define a function

$$\mathbf{h}_{\text{rel},j}(\mathbf{p}_{k,j}, t_k)_j = \begin{bmatrix} \tilde{\mathbf{s}}(t_k; \mathbf{p}_{k,j})_j \\ \tilde{\mathbf{s}}(t_k + \Delta t; \mathbf{p}_{k,j})_j \\ \tilde{\mathbf{s}}(t_k + 2\Delta t; \mathbf{p}_{k,j})_j \\ \vdots \\ \tilde{\mathbf{s}}(t_k + (N_{\text{rel}} - 1)\Delta t; \mathbf{p}_{k,j})_j \end{bmatrix}, \quad (5.14)$$

in which the index  $j \in \{1, \dots, 6\}$  refers to the type of the relative measurement that is represented (i.e. acceleration or angular velocity in one of the directions). The function  $\mathbf{h}_{\text{rel},j}$  thus evaluates the polynomial for a specific type of relative measurement at all time points there is a relative measurement. It is linear in the polynomial coefficients, and can be written as:

$$\mathbf{h}_{\text{rel},j}(\mathbf{p}_{k,j}, t_k)_j = \Gamma \mathbf{p}_{k,j}, \quad (5.15)$$

where  $\Gamma$  is a matrix that corresponds to the polynomial basis, and  $\mathbf{p}_{k,j}$  refers to the polynomial coefficients for frame  $k$  of the relative measurements denoted by  $j$ . Equation (5.12) hence becomes:

$$\sum_{j=0}^{N_{\text{rel}}-1} \| \tilde{\mathbf{s}}(t_k + j\Delta t, \mathbf{p}_k) - \mathbf{y}_{\text{rel}}(t_k + j\Delta t) \|_{Q_k^{-1}}^2 = \sum_{j=1}^6 \sigma_j^{-2} \| \Gamma \mathbf{p}_{k,j} - \mathbf{y}_{\text{rel},k,j} \|_2^2, \quad (5.16)$$

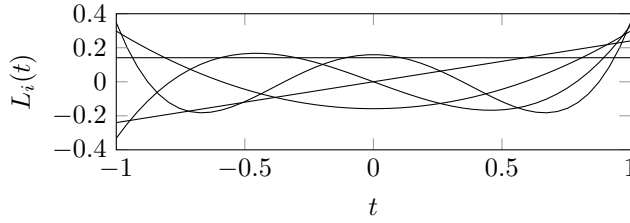


Figure 5.5: The Gram polynomials up to order 4 for a grid of 50 nodes.

where  $\mathbf{y}_{\text{rel},k,j}$  is a vector containing all relative measurements in one frame for the specific type of relative measurements denoted by  $j$ . It can be shown by expansion of terms that Equation (5.16) is equivalent to:

$$\sum_{j=1}^6 \sigma_j^{-2} \| \Gamma \mathbf{p}_{k,j} - \mathbf{y}_{\text{rel},k,j} \|_2^2 = \sum_{j=1}^6 \sigma_j^{-2} \| \mathbf{p}_{k,j} - \tilde{\mathbf{p}}_{k,j} \|_{\Gamma^T \Gamma}^2 + C, \quad (5.17)$$

where  $C$  is a constant term that has no influence on the optimisation, and where

$$\tilde{\mathbf{p}}_{k,j} = (\Gamma^T \Gamma)^{-1} \Gamma^T \mathbf{y}_{\text{rel},k,j}, \quad (5.18)$$

which is the solution of the unconstrained linear least squares problem. By using this formulation, the relative measurements can be discarded after having solved the unconstrained linear least squares problem by the matrix-vector multiplication 5.18, which saves memory and computation time of the objective function. This solution is also used to initialise the MHE.

The polynomials that we choose for our MHE are the ‘Gram polynomials’ [7]. They are orthonormal on an equidistant grid on the interval  $[-1, 1]$ , i.e. they satisfy the property

$$\sum_{k=0}^{N_{\text{rel}}} L_i(t_k) L_j(t_k) = \begin{cases} 1, & i = j \\ 0, & i \neq j \end{cases}, \quad t_k = -1 + \frac{2k}{N_{\text{rel}}}, \quad (5.19)$$

and thus form a matrix  $\Gamma$  that is orthonormal, meaning that  $\Gamma^T \Gamma = \mathbb{I}$ , the identity matrix. Figure 5.5 shows the Gram polynomials up to order 4 for a grid containing 50 nodes. Equation (5.18) now simplifies to:

$$\tilde{\mathbf{p}}_{k,j} = \Gamma^T \mathbf{y}_{\text{rel},k,j}, \quad (5.20)$$

and Equation (5.17) becomes:

$$\sum_{j=1}^6 \sigma_j^{-2} \| \mathbf{p}_{k,j} - \tilde{\mathbf{p}}_{k,j} \|_{\Gamma^T \Gamma}^2 = \sum_{j=1}^6 \sigma_j^{-2} \| \mathbf{p}_{k,j} - \tilde{\mathbf{p}}_{k,j} \|_2^2. \quad (5.21)$$

By choosing an orthonormal polynomial basis, Problem (5.11) can now be formulated as:

$$\begin{aligned}
 \underset{\mathbf{x}, \mathbf{p}, \mathbf{b}}{\text{minimise}} \quad & \sum_{k=N_c-N}^{N_c} \Psi(\mathbf{y}_{\text{abs},k} - \mathbf{h}_{\text{abs}}(\mathbf{x}_k)) \\
 & + \sum_{k=N_c-N}^{N_c-1} \sum_{j=1}^6 \sigma_j^{-2} \|\mathbf{p}_{k,j} - \tilde{\mathbf{p}}_{k,j}\|_2^2 \\
 & + \|\mathbf{b} - \bar{\mathbf{b}}\|_B^2 \\
 \text{subject to} \quad & \mathbf{x}_{k+1} = \mathbf{F}(\mathbf{x}_k, \mathbf{p}_k, \mathbf{b}), \\
 & g(\mathbf{x}_{N_c}) = 0,
 \end{aligned} \tag{5.22}$$

in which  $\mathbf{h}$  is the pinhole camera model given by Equation (5.4), with the encoder measurement added to it,  $\mathbf{F}$  is the discrete form of Equations 5.1 and 5.2 and  $g$  is the quaternion norm constraint.

Problem (5.22) should be solved every time a new absolute measurement is available. After the problem is solved, the state is propagated by integrating the kinematic model (5.1–5.2) using the IMU measurements, corrected with the bias estimate  $b$ , as input to this model. This is known as ‘dead reckoning’. This is done until a new absolute measurement is available.

## 5.6 Choices for penalty function

The penalty function  $\Psi$  for the absolute measurements is not yet specified. We consider two choices for  $\Psi$ : a least-squares penalty function using the  $\ell_2$ -norm and a robust penalty function using the Huber penalty function.

### 5.6.1 Least Squares Estimation

A first choice for the penalty function  $\Psi$  for the residues of the absolute measurements is the  $\ell_2$ -norm:

$$\Psi_{\text{LS}}(\mathbf{y}) = \|\mathbf{y}\|_{R^{-1}}^2, \tag{5.23}$$

where  $R$  is the covariance matrix for the absolute measurements. Problem (5.22) hence becomes:

$$\begin{aligned}
 \underset{\mathbf{x}, \mathbf{p}, \mathbf{b}}{\text{minimise}} \quad & \sum_{k=N_c-N}^{N_c} \| \mathbf{y}_{\text{abs},k} - \mathbf{h}_{\text{abs}}(\mathbf{x}_k) \|_{R^{-1}}^2 \\
 & + \sum_{k=N_c-N}^{N_c-1} \sum_{j=1}^6 \sigma_j^{-2} \| \mathbf{p}_{k,j} - \tilde{\mathbf{p}}_{k,j} \|_2^2 \\
 & + \| \mathbf{b} - \bar{\mathbf{b}} \|_B^2 \\
 \text{subject to} \quad & \mathbf{x}_{k+1} = \mathbf{F}(\mathbf{x}_k, \mathbf{p}_k, \mathbf{b}), \\
 & g(\mathbf{x}_{N_c}) = 0.
 \end{aligned} \tag{5.24}$$

The number of optimisation variables in Problem (5.24) is equal to  $n_o = (N+1)(n_x + n_v) + Nn_p + n_b$ , with  $n_x = 12$  and  $n_v = 13$ .  $n_b = 6$  is the number of bias terms and  $n_p$  is the number of polynomial coefficients, equal to  $n_p = 6(m+1)$  with  $m$  the polynomial order. With an horizon length of 6 and second order polynomial approximations, as is done in Section 5.7 and Section 5.8, this results in a total of 289 optimisation variables.

### 5.6.2 Robust Estimation

The algorithm that detects the marker positions in the image does not always converge to the correct solution due to disturbances present in the image. This causes outliers present in the absolute measurements. To increase the robustness of the MHE to such outliers, the Huber penalty function can be used as penalty function for the absolute measurements. The Huber penalty function for a scalar input is given by:

$$\Psi_{\text{Huber}}\left(\frac{y}{\rho}\right) = \begin{cases} \left(\frac{y}{\rho}\right)^2 & |y| \leq \rho, \\ \rho(2\left|\frac{y}{\rho}\right| - \rho) & |y| > \rho. \end{cases} \tag{5.25}$$

It is thus equal to an  $\ell_2$ -norm for small errors, but acts like the  $\ell_1$ -norm as soon as the errors are bigger than a certain threshold, and thus is much less sensitive to outliers than the  $\ell_2$ -norm. Figure 5.6 graphically presents the Huber penalty function for  $\rho = 5$ . In an optimisation framework, the Huber penalty function

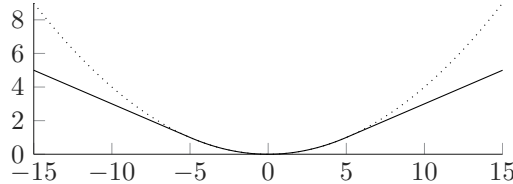


Figure 5.6: Huber penalty function (full line) and 2-norm (dotted line).

for a scalar can be formulated as [9]:

$$\begin{aligned} \Psi_{\text{Huber}}\left(\frac{y}{\sigma}\right) = & \underset{\mu, \nu}{\text{minimise}} \quad \mu^2 + 2\rho\nu \\ \text{subject to} & -\mu - \nu \leq \frac{y}{\sigma} \leq \mu + \nu, \\ & 0 \leq \mu \leq \rho, \\ & 0 \leq \nu, \end{aligned} \quad (5.26)$$

where  $\mu$  and  $\nu$  are slack variables.  $\mu$  covers the quadratic region of the Huber penalty function and  $\nu$  covers the linear region. Thus, the overall optimisation problem can be formulated as an NLP with three continuously differentiable problem functions. For each residual two slack variables are needed. The threshold  $\rho$  should be large enough that normal noise levels lie within the  $\ell_2$ -region, but not so large that outliers lie within the  $\ell_1$ -region. A good value for  $\rho$  is for example 5, which means only about one in three million correct measurements fall outside the  $\ell_2$ -region. It can be verified that the constraint  $0 \leq \mu \leq \rho$  is not required. This can intuitively be seen by observing that when  $\mu$  equals  $\rho$ , it is more beneficial to increase  $\nu$  rather than to increase  $\mu$  beyond  $\rho$ . The constraint  $0 \leq \mu \leq \rho$  is thus only weakly active and can be left out.

Applying the Huber penalty function to the term for the absolute measurements, and using the formulation with slack variables, results in the following

optimisation problem:

$$\begin{aligned}
 \text{minimise}_{\mathbf{x}, \mathbf{p}, \boldsymbol{\mu}, \boldsymbol{\nu}, \mathbf{b}} \quad & \sum_{k=N_c-N}^{N_c} (\|\boldsymbol{\mu}_k\|_2^2 + 2\rho\mathbf{e}^T\boldsymbol{\nu}_k) \\
 & + \sum_{k=N_c-N}^{N_c-1} \sum_{j=1}^6 \sigma_j^{-2} \|\mathbf{p}_{k,j} - \tilde{\mathbf{p}}_{k,j}\|_2^2 \\
 & + \|\mathbf{b} - \bar{\mathbf{b}}\|_B^2
 \end{aligned} \tag{5.27}$$

$$\text{subject to } \mathbf{x}_{k+1} = \mathbf{F}(\mathbf{x}_k, \mathbf{p}_k, \mathbf{b}),$$

$$g(\mathbf{x}_{N_c}) = 0,$$

$$-\boldsymbol{\mu}_k - \boldsymbol{\nu}_k \leq R^{-1/2}(\mathbf{y}_{\text{abs},k} - \mathbf{h}_{\text{abs}}(\mathbf{x}_k)) \leq \boldsymbol{\mu}_k + \boldsymbol{\nu}_k,$$

$$\mathbf{0} \leq \boldsymbol{\nu}_k,$$

where  $\boldsymbol{\mu}_k$  and  $\boldsymbol{\nu}_k$  are vectors of slack variables.  $\mathbf{e}$  is a column vector whose entries are all ones, such that  $\mathbf{e}^T\boldsymbol{\nu}_k$  gives the sum of the elements of  $\boldsymbol{\nu}_k$ . Because of the slack variables, Problem (5.27) requires  $24(N+1)$  more optimisation variables than Problem (5.24), namely  $2(N+1)$  more per camera measurement, of which we have 12. This brings the total of optimisation variables to 457 for an horizon length of 6 and second order polynomials.

## 5.7 Simulation results

To assess the performance of the developed estimators, a series of simulations are done. In these simulations, a model of the system is simulated to create simulated measurements, to which Gaussian noise and, for the camera measurements, outliers are added. These simulated measurements are then used to the estimator based on the Huber penalty function with the estimator based on the  $\ell_2$ -norm.

Both for the simulations as for the experiments, the stereo vision system is sampled at a frequency of 15 Hz. The IMU is sampled at 800 Hz. The MHE is implemented using CasADi. All results shown in this chapter are obtained using CasADi [2]. The optimisation problems are solved using an SQP method, allowing full convergence of each problem. The horizon includes 7 absolute measurements and hence spans 0.375 s. In the simulation, there are 50 relative measurements in between 2 absolute measurements. Gaussian noise with a standard deviation of 5 pixels is added to the absolute measurements, and there

is a 5 % change that there is an outlier. An outlier means that the position of the marker is random within the image.  $\rho$  is taken to be 5. For the relative measurements, Gaussian noise with a standard deviation of  $0.1 \frac{\text{m}}{\text{s}^2}$  and  $0.57 \frac{\text{°}}{\text{s}}$  is added for the acceleration and angular velocity measurements respectively, corresponding to the specifications of the IMU. Polynomials of degree 2 are used to approximate the relative measurements. Both the MHEs using the  $\ell_2$ -norm and the Huber penalty function for the absolute measurements are implemented and tested for data with and without outliers. A comparison with an EKF is also made. This is a standard EKF as described in Section 4.4.2 in which the IMU measurements are used at the frequency they are captured. It uses the same covariances as the MHE.

In case there are no outliers present in the measurements, all estimators have the same estimation performance and converge to the solution. Figure 5.7 shows the reprojection for one marker in time in case there are outliers present in the measurements for both the  $\ell_2$ -norm and the Huber penalty function. There is an outlier at a time of about 3.45 s. It is clear from the figure that the Huber penalty function (full line) gives a better estimate than the  $\ell_2$ -norm (dotted line) in case of an outlier. Once the outlier is out of the horizon, the performance of both MHEs is the same. Each time an estimator comes into the estimation horizon, the state estimate is perturbed. As the horizon window passes over the outlier, the effect the outlier has on the state estimates reduces.

Figure 5.8 shows the corresponding error in the estimation of position and orientation for both moving horizon estimators and for the EKF. For the error in orientation, the equivalent angle of rotation of the relative orientation between the estimate and the solution is taken. This simulation experiment is repeated 100 times, using noise with the same characteristics. Table 5.3 shows the average and maximum estimation error over all runs. The maximum position error for the robust MHE is about 10 times lower than the maximum position error of the EKF, and about 8 times lower than the maximum position error of the MHE using the  $\ell_2$ -norm. The robust MHE thus performs much better than the EKF and the MHE using the  $\ell_2$ -norm.

## 5.8 Results with experimental data

To validate the developed estimators, they are run off line on several batches of experimental data. In the experiments, the IMU is running at 800 Hz, and the cameras are running at 7.5 Hz. Figure 5.9 shows a time series of absolute measurements for the position of one marker in one camera image and the corresponding reprojected state estimates from the robust MHE. Because the

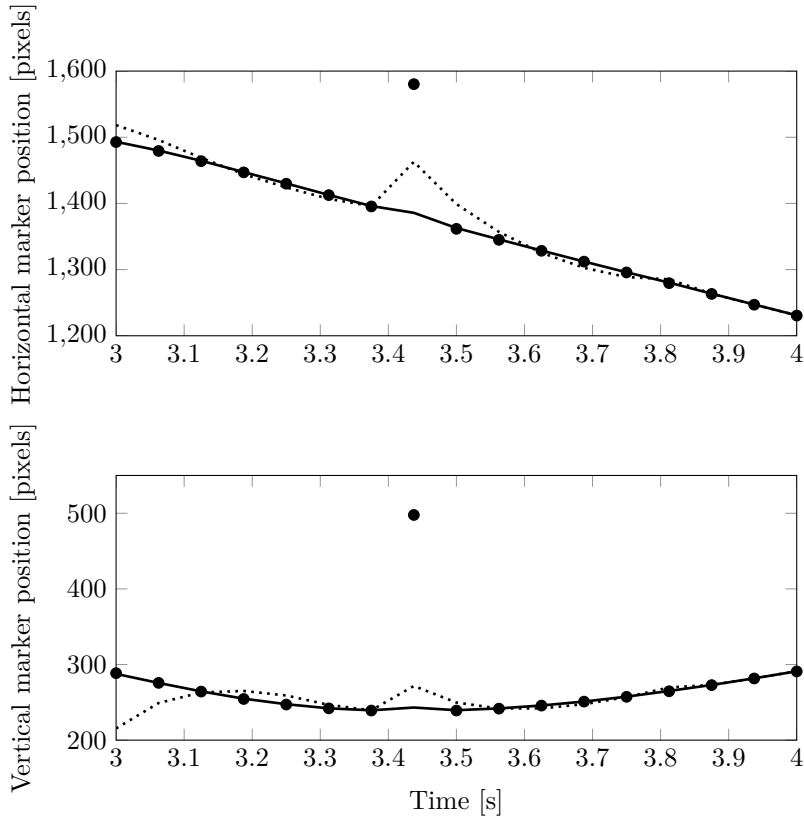


Figure 5.7: Reprojection of MHE state estimate on camera image for one marker on one image. The dots denote the actual measurements. The dotted line is the reprojected  $\ell_2$ -estimate, the full line is the reprojected estimate using the Huber penalty function.

experiments are done in a darkened room, the marker detection algorithm is always successful and therefore there are no outliers in the data. Because there are no outliers present in the data, the performance of the  $\ell_2$ -norm and the Huber norm is the same.

Figure 5.10 shows the  $x$ -component of the acceleration measurements (dotted line) in combination with the polynomials that try to fit this acceleration component (full line). Five frames of one MHE solution are shown. Note that we are not aiming for the optimal fit of the polynomial on these measurements, but for an optimal fit in combination with the camera measurements. Polynomials

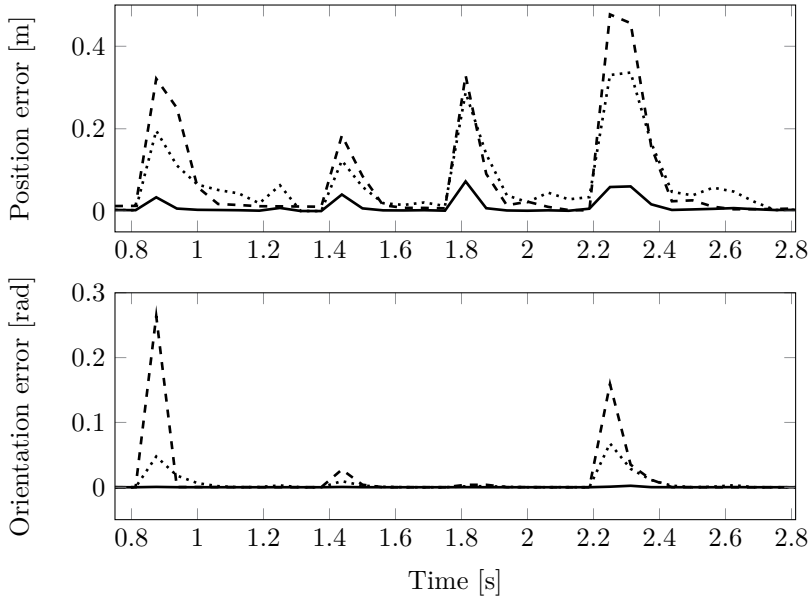


Figure 5.8: Error in pose estimates. Dashed line: EKF estimate, dotted line: MHE estimate using the  $\ell_2$ -norm, full line: MHE estimate using the Huber penalty function.

Estimator	Unit	EKF	MHE( $\ell_2$ )	MHE(Huber)
Mean position error	mm	93.2	72.6	6.6
Max position error	mm	687.2	540.8	65.8
Mean orientation error	mrad	39.9	13.2	0.1
Max orientation error	mrad	745.9	182.9	1.3

Table 5.3: Average estimation error over 100 runs for EKF and MHE using Huber penalty function and  $\ell_2$ -norm.

of degree 2 are used to approximate the IMU measurements. From the IMU measurements, we can see that the aeroplane is oscillating at a frequency of about 4 Hz. The polynomials seem to capture this oscillation quite well. There are jumps in the polynomials, for example visible at  $t \approx 0.55$  s because there are no continuity constraints on the polynomials.

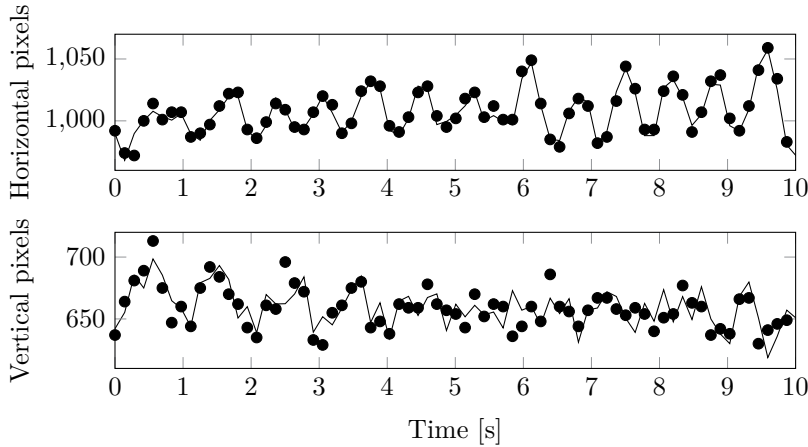


Figure 5.9: Camera image reprojection of state estimate for one marker on one image. The dots denote the measurements. The line is the estimate of the robust MHE.

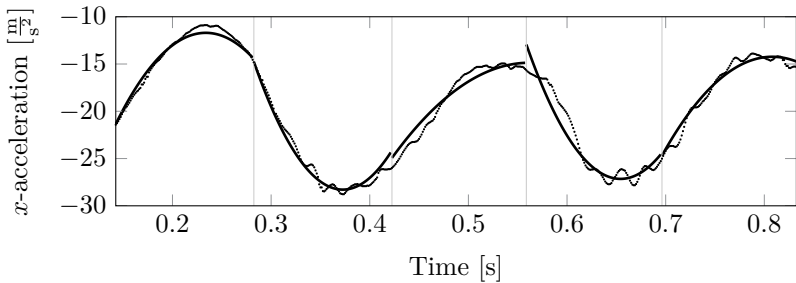


Figure 5.10:  $x$ -component of acceleration measurements (dotted line) and polynomials that fit this acceleration measurement (full line) for four frames of one MHE solution.

## 5.9 Conclusion

We demonstrated a moving horizon estimator that is able to fuse IMU measurements and measurements from a stereo vision system, and can reliably estimate the pose of a tethered aeroplane while it performs high acceleration aerobatic manoeuvres. The estimator approximates the IMU measurements with polynomials to reduce the number of optimisation variables in the optimisation problem. The estimator is made robust against outliers present in the camera

measurements by using the Huber penalty function instead of the  $\ell_2$ -norm. A comparison of both MHE formulations is performed in simulation, showing that the Huber penalty function performs much better than the  $\ell_2$ -norm when outliers are present in the measurements. In experiments on data recorded on the indoors test set-up, there are only slight differences between the filters, but it is expected that once experiments are done in a less controlled environment there may be outliers present in the data, and the Huber penalty function is needed.

The idea to approximate measurements that come at a high sampling rate using polynomials could potentially be used for other estimation problems as well. For systems where measurements can be considered as inputs to a model, which is the case for the IMU measurements, the approach could be employed as described in this chapter. If this is not the case, integrators that provide continuous output are needed, e.g. the integrators described in [79]. This continuous output, which may also come in the form of a set of polynomials, can then be compared to the continuous approximation of the measurements.

After the relative and absolute measurements have been fused, the dead reckoning approach is typically used to provide state updates at a higher frequency. In dead reckoning, the IMU measurements are kinematically integrated using the previous state estimates as starting point. It is discussed in more detail in Chapter 6.

# Chapter 6

## Moving horizon estimation and control with a dynamic model

### 6.1 Introduction

This chapter focuses on the development and performance assessment of different types of estimators that can be used to estimate the position and orientation of the tethered aeroplane, and shows some results from closed loop control experiments. This chapter is based on [46] and [47].

The typical approach to fuse measurements coming from an IMU and an absolute measurement system is to use a kinematic model of the system and to use the IMU measurements to integrate the system. Some form of a Kalman Filter, extended or unscented, or possibly a moving horizon estimator, is then typically used to fuse in the absolute measurement and remove the drift due to the integration of the noisy IMU signal [5, 15, 19, 89, 6, 61, 18, 21]. In [35] a kinematic model is proposed for an AWE system. Chapter 5 proposed to use MHE to perform the sensor fusion and made the estimator robust by using appropriate penalty functions. A kinematic model has the advantage that it does not depend on the system dynamics and characteristics such as mass or aerodynamics.

In the case of AWE systems high fidelity models of the system exist. Such a model could improve the estimation performance compared to using a kinematic

model because it bears with it extra information about the behaviour of the system. By solving the resulting estimation problem that uses the dynamic model of the system with moving horizon estimation, the nonlinearities of these models are fully captured. This can lead to a better estimation performance compared to traditional techniques such as the Kalman filter.

The MHE problem described above would operate at the frequency of the absolute measurements. To achieve updates of the state estimation at a higher frequency, the dead reckoning approach, in which the acceleration and angular velocity measurements are kinematically integrated, is typically used. We propose to replace it by an '*inner Moving Horizon estimator*' that combines the dynamic model with the IMU measurements to provide state estimates at a higher frequency. It runs in between 2 steps of the outer estimator at a higher frequency.

In this chapter, a test problem for the developed estimators with both simulation and experimental data and a comparison methodology for different estimators is presented. A comparison of estimators based on kinematic and dynamic models for the considered system is made.

One of the goals of the developed estimators and the experimental set-ups described in Chapter 2 and Chapter 3 is to use them for closed loop experiments in combination with Nonlinear Model Predictive Control (NMPC). In [47], closed loop experiments performed on the indoors set-up are discussed, which is outlined in this chapter. The estimator used for these experiments is a simplified version of the outer estimator that is developed in this chapter. The setup of the controller used for the experiments is described. No claims on the performance of this controller are made, it just serves to show feasibility of closed-loop control experiments on the developed set-up.

This chapter is organised as follows: Section 6.2 presents a dynamic model of the system, Section 6.3 discusses the '*outer*' estimation problem that fuses the model, IMU measurements and absolute measurements. Section 6.4 discusses the '*inner*' estimation problem that used the IMU measurements to provide fast state updates. Section 6.5 describes the NMPC controller that is implemented on the system and gives the results of the control experiments. Section 6.6 forms a conclusion. The results in this chapter are obtained using the **ACADO Code Generation Tool**.

State variable	Defines	Unit
$\mathbf{r}$	Position of aeroplane in arm frame	m
$\dot{\mathbf{r}}$	Velocity of aeroplane w.r.t. arm frame	$\frac{m}{s}$
$\mathbf{R}$	Orientation of aeroplane w.r.t. arm frame	—
$\boldsymbol{\omega}$	Angular velocity of aeroplane	$\frac{rad}{s}$
$\phi_a$	Angle of aileron of aeroplane	rad
$\phi_e$	Angle of elevator of aeroplane	rad
$l$	Tether length	m
$\dot{l}$	Tether velocity	$\frac{m}{s}$
$c_\delta$	Cosine of carousel angle	—
$s_\delta$	Sine of carousel angle	—
$\dot{\delta}$	Angular velocity of carousel	$\frac{rad}{s}$
$T_c$	Torque of carousel motor	N m

Table 6.1: State definition for dynamic model.

Control variable	Defines	Unit
$\dot{\phi}_a$	Angular velocity of aileron of aeroplane	$\frac{rad}{s}$
$\dot{\phi}_e$	Angular velocity of elevator of aeroplane	$\frac{rad}{s}$
$\ddot{l}$	Tether acceleration	$\frac{m}{s^2}$
$\dot{T}_c$	Time derivative of carousel motor torque	$\frac{N\ m}{s}$

Table 6.2: Control definition for dynamic model.

## 6.2 Dynamic model for AWE system

### 6.2.1 State definition

To define the state of the dynamic model, the same frame definitions presented in Section 5.2 are used, but some extra states and control inputs are needed compared to the kinematic model. A complete overview of the state and control vector is given in Table 6.1 and Table 6.2 respectively. A more detailed description of some of the components is given below.

The position of the aeroplane is again defined as the position of its centre of mass expressed in the arm frame using Cartesian coordinates, but now in combination with the tether constraint

$$c(\mathbf{r}, \mathbf{R}, l) = \frac{1}{2} \left( (\mathbf{r} + R\mathbf{r}_T)^T (\mathbf{r} + R\mathbf{r}_T) - l^2 \right) = 0, \quad (6.1)$$

which expresses that the tether attachment point on the aeroplane is always at a distance  $l$  from the attachment point on the carousel.  $\mathbf{r}_T$  is the position of the

tether attachment point on the aeroplane and  $l$  is the tether length. Similarly, the velocity of the aeroplane is also expressed in Cartesian coordinates as the velocity of the aeroplane with respect to the arm frame.

Different from the kinematic model where quaternions are used to represent the orientation of the aeroplane, the dynamic model uses the  $3 \times 3$  direct cosine matrix that transfers body frame coordinates to arm frame coordinates. This choice is justified in Section 6.2.4. Early results suggest that the direct cosine matrix may be better suited because it reduces the nonlinearity of the model equations. The 9 coefficients are linked via 6 orthonormality constraints given by:

$$R^T R = \mathbb{I}_{3 \times 3} \quad (6.2)$$

of which due to symmetry only the upper triangle is relevant.  $\mathbb{I}_{3 \times 3}$  is the 3 by 3 identity matrix.

The straightforward solution to model the angle of the carousel would be to just use the single variable  $\delta$ , as is done for the kinematic model. A problem with this however is that it continues to grow unbounded as the carousel keeps rotating during the rotation start. Therefore two variables  $c_\delta$  and  $s_\delta$  are used that represent the cosine and sine of the carousel angle  $\delta$  respectively, with the constraint

$$c_\delta^2 + s_\delta^2 = 1. \quad (6.3)$$

The derivatives of the aileron and elevator angles, the carousel motor torque and the tether velocity are controlled such that they display a continuous behaviour.

### 6.2.2 Model equations

The dynamic system model for the system considered in this thesis is discussed in detail in [49].

The time evolution of the rotation matrix reads:

$$\dot{R} = R \tilde{\omega}_\times, \quad (6.4)$$

with  $\tilde{\omega} = \omega - R^T \mathbf{1}_z \dot{\delta}$  is the angular velocity between the aeroplane and the arm frame, given in body frame coordinates and with  $\cdot_\times$  the skew operator that transforms a vector of  $\mathbb{R}^3$  into the corresponding skew-symmetric matrix.

The aeroplane and carousel dynamics are derived using Lagrangian mechanics. In Lagrangian mechanics, the configuration of a system is described by an arbitrary, independent set of generalised coordinates  $\mathbf{q} \in Q$  restricted to evolve

on a given manifold  $\mathbf{c}(\mathbf{q}) = \mathbf{0}$  with  $\mathbf{c} : Q \rightarrow C$ . The Lagrange function of the system is defined as:

$$\mathcal{L}(\mathbf{q}, \dot{\mathbf{q}}, \boldsymbol{\lambda}) = T(\mathbf{q}, \dot{\mathbf{q}}) - V(\mathbf{q}) - \langle \boldsymbol{\lambda}, \mathbf{c}(\mathbf{q}) \rangle, \quad (6.5)$$

With  $T$  and  $V$  the kinetic and potential energy of the system respectively,  $\boldsymbol{\lambda}$  the set of Lagrange multipliers associated to the constraints  $\mathbf{c}$  and  $\langle \cdot, \cdot \rangle$  the scalar product on  $C$ . The motion of the system is defined by the Lagrange equations:

$$\frac{d}{dt} \frac{\partial \mathcal{L}}{\partial \dot{\mathbf{q}}} - \frac{\partial \mathcal{L}}{\partial \mathbf{q}} = \mathbf{F}_q, \quad \mathbf{c}(\mathbf{q}) = \mathbf{0}, \quad (6.6)$$

where  $\mathbf{F}_q$  is the vector of generalised forces acting on the system that are defined by the virtual work condition: for any infinitesimal displacement  $\delta \mathbf{q}$  of the system configuration, yielding the work  $\delta W$  on the system, the equality

$$\delta W = \langle \delta \mathbf{q}, \mathbf{F}_q \rangle \quad (6.7)$$

must hold. Equation (6.6) results in an index-3 Differential Algebraic Equation (DAE).

Assuming the tether is massless, the kinetic and potential energy  $T$  and  $V$  of the system are:

$$T = \frac{1}{2} J_c \dot{\delta}^2 + \frac{1}{2} m \dot{\mathbf{r}}_{\text{world}}^T \dot{\mathbf{r}}_{\text{world}} + \frac{1}{2} \boldsymbol{\omega}^T J_a \boldsymbol{\omega}, \quad (6.8a)$$

$$V = -mgz, \quad (6.8b)$$

where  $m$  is the mass of the aeroplane,  $J_a$  the matrix representation of the inertia tensor of the wing in the body frame,  $J_c$  the rotational inertia of the carousel. Note that the potential energy has a negative sign due to the north-east-down convention.  $\dot{\mathbf{r}}_{\text{world}}$  is the position of the aeroplane in the world frame, and is related to its position in the arm frame by:

$$\dot{\mathbf{r}}_{\text{world}} = R_c R \left( \mathbf{r} + \begin{bmatrix} r_{\text{arm}} \\ 0 \\ 0 \end{bmatrix} \right), \quad (6.9)$$

in which  $R_c$  is the rotation matrix that transfers carousel frame coordinates to world frame coordinates and is given by:

$$\begin{bmatrix} \cos(\delta) & -\sin(\delta) & 0 \\ \sin(\delta) & \cos(\delta) & 0 \\ 0 & 0 & 1 \end{bmatrix}. \quad (6.10)$$

Using  $\xi^T = [\delta \ r^T \ R]$ , the aeroplane and carousel dynamics are given by:

$$\frac{d}{dt} \nabla_{\dot{\xi}} \mathcal{L} - \nabla_{\xi} = \frac{d}{dt} \nabla_{\dot{\xi}} T - \nabla_{\xi} (T - V) + \nabla_{\xi} (\lambda^T c(r, R, l)) = F_{\xi}, \quad (6.11)$$

where  $\frac{d}{dt} \nabla_{\dot{\xi}} T = M \ddot{\xi} + C \dot{\xi}$ , with  $M$  and  $C$  the generalised inertia matrix  $M$  and the Coriolis matrix given by:

$$M = \nabla_{\dot{\xi}} \dot{\xi} \left( \frac{1}{2} J_c \dot{\delta}^2 + \frac{1}{2} \dot{r}_{\text{world}}^T \dot{r}_{\text{world}}^T \right), \quad (6.12a)$$

$$C = \nabla_{\dot{\xi}} \xi \left( \frac{1}{2} J_c \dot{\delta}^2 + \frac{1}{2} \dot{r}_{\text{world}}^T \dot{r}_{\text{world}}^T \right). \quad (6.12b)$$

This is an index-3 DAE. A better form can be obtained by index reduction techniques, in which the constraint (6.1) is differentiated twice in order to impose  $\ddot{c}(\mathbf{x}) = 0$  instead of  $c(\mathbf{x}) = 0$  in the model equation. This yields an index-1 DAE with consistency conditions [49]

$$c(\mathbf{x}) = 0, \quad \dot{c}(\mathbf{x}) = 0, \quad (6.13)$$

that must be satisfied at some point on the system trajectory, with  $\dot{c}$  the time derivative of Equation (6.1) given by:

$$\dot{c}(\mathbf{x}) = (\dot{r} + R(\tilde{\omega} \times \mathbf{r}_T))^T (\mathbf{r} + R\mathbf{r}_T) - \dot{l}l = 0. \quad (6.14)$$

The index-reduced dynamics of the system read:

$$\begin{bmatrix} M & \mathbf{0} & \nabla_{\xi} c \\ \mathbf{0} & J_a & \mathbf{r}_T \times \mathbf{r}^T \mathbf{r} \\ \nabla_{\xi} c^T - (\mathbf{r}_T \times R^T \mathbf{r})^T R^T \mathbf{I}_z & (\mathbf{r}_T \times R^T \mathbf{r})^T & 0 \end{bmatrix} \begin{bmatrix} \ddot{\xi} \\ \dot{\omega} \\ \lambda \end{bmatrix} = \begin{bmatrix} \mathbf{F}_{\text{aero}} - C \dot{\xi} + \nabla_{\xi} (T - V) \\ \mathbf{M}_{\text{aero}} - \omega \times J_a \omega \\ -\nabla_{\xi} \dot{c}^T \dot{\xi} - 2P_R (\nabla_R \dot{c})^T (\omega - R^T \mathbf{1}_z \dot{\delta}) + l^2 + l \ddot{l} \end{bmatrix}, \quad (6.15)$$

where  $\mathbf{F}_{\text{aero}}$  and  $\mathbf{M}_{\text{aero}}$  are the aerodynamic force and torque respectively.

Apart for the system dynamics given by Equation (6.15), the rest of the model is given by the trivial kinematic relations:

$$\frac{d}{dt} \begin{bmatrix} \mathbf{r} \\ \phi_a \\ \phi_e \\ l \\ \dot{l} \\ c_\delta \\ s_\delta \\ T_c \end{bmatrix} = \begin{bmatrix} \dot{\mathbf{r}} \\ \dot{\phi}_a \\ \dot{\phi}_e \\ \dot{l} \\ \ddot{l} \\ -s_\delta \dot{\delta} \\ c_\delta \dot{\delta} \\ \dot{T}_c \end{bmatrix}. \quad (6.16)$$

## Aerodynamics

The aerodynamic forces and torques depend on the wind relative to the aeroplane. The velocity of the wind relative to the aeroplane is given by:

$$\mathbf{v}_w^{\text{world}} = \dot{\mathbf{r}}_{\text{world}} - \mathbf{w}(\dot{\mathbf{r}}_{\text{world}}, t), \quad (6.17)$$

in which  $\mathbf{w}$  is the local wind vector expressed in world frame coordinates which depends on the position of the aeroplane and is time dependent. The relative wind velocity in the body frame is then given by:

$$\mathbf{v}_w = R_c^T R_c^T \mathbf{v}_w^{\text{world}}. \quad (6.18)$$

The aerodynamic forces  $\mathbf{F}_{\text{aero}}$  and moments  $\mathbf{T}_{\text{aero}}$  read:

$$\mathbf{F}_{\text{aero}} = \frac{1}{2} \rho A \| \mathbf{v}_w \|_2 (C_L \mathbf{v}_w \times \mathbf{e}_2 - C_D \mathbf{v}_w + C_T \| \mathbf{v}_w \|_2 \mathbf{e}_2), \quad (6.19a)$$

$$\mathbf{T}_{\text{aero}} = \frac{1}{2} \rho A \| \mathbf{v}_w \|_2^2 \begin{bmatrix} b_{\text{ref}} C_R \\ c_{\text{ref}} C_P \\ b_{\text{ref}} C_Y \end{bmatrix}, \quad (6.19b)$$

in which  $\rho$  is the air density and  $A$  the wing area of the aeroplane,  $b_{\text{ref}}$  and  $c_{\text{ref}}$  are the wing span and wing chord respectively.  $\mathbf{e}_2$  is the  $y$ -axis of the body frame which is orientated along the wing and  $\times$  denotes the cross product between two vectors. The aerodynamic coefficients  $C_L$ ,  $C_D$  and  $C_T$  are needed to compute the lift, drag and lateral force;  $C_R$ ,  $C_P$  and  $C_Y$  are needed for the roll, pitch and yaw torque. The coefficients are function of the angle of attack and side-slip angle of the aeroplane  $\alpha$  and  $\beta$ , its angular velocity  $\boldsymbol{\omega}$  and the angles of the

aileron and elevator  $\phi_a$  and  $\phi_e$ . The angle of attack and side-slip angle read:

$$\alpha = \tan \left( \frac{\mathbf{v}_{w_z}}{\mathbf{v}_{w_x}} \right) \approx \frac{\mathbf{v}_{w_z}}{\mathbf{v}_{w_x}}, \quad (6.20a)$$

$$\beta = \tan \left( \frac{\mathbf{v}_{w_y}}{\mathbf{v}_{w_x}} \right) \approx \frac{\mathbf{v}_{w_y}}{\mathbf{v}_{w_x}}. \quad (6.20b)$$

The aerodynamic coefficients are computed by:

$$C_L = C_{L_\alpha} \alpha + C_{L_e} \phi_e + C_{L_0}, \quad (6.21a)$$

$$C_D = C_{D_\alpha} \alpha + C_{D_{\alpha^2}} \alpha^2 + C_{D_{\beta^2}} \beta^2 + C_{D_e} \phi_e + C_{D_{a^2}} \alpha^2 + \quad (6.21b)$$

$$C_{D,e^2} \phi_e^2 + C_{D_{\alpha,e}} \alpha \phi_e + C_{D_{\beta,a}} \beta \phi_a + C_{D_0},$$

$$C_T = C_{T_\beta} \beta, \quad (6.21c)$$

$$C_R = C_{R_\beta} \beta + C_{R_{\alpha\beta}} \alpha \beta + C_{R_a} \phi_a + C_{R_{\omega_x}} \boldsymbol{\omega}_x + C_{R_{\omega_y}} \boldsymbol{\omega}_y + C_{R_{\omega_z}} \boldsymbol{\omega}_z, \quad (6.21d)$$

$$C_P = C_{P_\alpha} \alpha + C_{P_e} \phi_e + C_{P_{\omega_x}} \boldsymbol{\omega}_x + C_{P_{\omega_y}} \boldsymbol{\omega}_y + C_{P_{\omega_z}} \boldsymbol{\omega}_z + C_{P_0}, \quad (6.21e)$$

$$C_Y = C_{Y_\beta} \beta + C_{Y_{\alpha\beta}} \alpha \beta + C_{Y_{\omega_x}} \boldsymbol{\omega}_x + C_{Y_{\omega_y}} \boldsymbol{\omega}_y + C_{Y_{\omega_z}} \boldsymbol{\omega}_z. \quad (6.21f)$$

Table C.2 in Appendix C lists the aerodynamic parameters of this model for the indoors carousel set-up. The other parameters of the model are listed in Table C.1.

### 6.2.3 Process noise

The model described above does not yet have process noise, which is needed when using the model for state estimation purposes. A first form of process noise is the difference between the control inputs we send to the system and control that is actually applied. This accounts for possible errors e.g. introduced by the servomotors that actuate the control surfaces.

Adding process noise only in this form would not account for modelling errors. An intuitive way to add more process noise to the system is to add three disturbance forces and three disturbance torques. A downside of this approach is that it is hard to determine what covariance should be set for these disturbance forces and torques. After all, the actual forces that act on the system are dependent on the air speed of the aeroplane, such that a constant covariance for the disturbances may prove to be too large for low air speeds, and too small for high air speeds.

Therefore we propose to add dimensionless disturbance forces and torques  $\mathbf{f}_d$  and  $\mathbf{t}_d$ . They are multiplied with the dynamic pressure  $\frac{1}{2}\rho \parallel \mathbf{v}_w \parallel_2^2 A$ , to give an actual force or torque. These are then added to  $\mathbf{F}_{\text{aero}}$  and  $\mathbf{M}_{\text{aero}}$  respectively. Throughout the rest of the chapter, we write the system model as  $\mathbf{f}(\mathbf{x}, \dot{\mathbf{x}}, \mathbf{u}, \lambda, \mathbf{w}) = \mathbf{0}$ , where  $\mathbf{w}$  comprises the control disturbances and disturbance forces and torques.

The complete state vector has size  $n_x = 26$  that are linked via 8 constraints, namely the two consistency conditions given by Equation (6.13), and the 6 orthonormality conditions given by Equation (6.2). We thus have 18 independent degrees of freedom. The control vector has size  $n_u = 4$ . The process noise vector has size  $n_w = 10$ , namely 6 disturbance forces and torques and 4 noise terms on the control inputs. The measurement noise vector has size  $n_v = 17$ , namely 12 camera measurements, one carousel encoder measurement, measurements of  $\phi_a$  and  $\phi_e$ , measurements of  $l$  and  $\dot{l}$ . If the IMU measurements are not approximated by polynomials, in total 6 terms may be added to the measurement noise vector.

### 6.2.4 Minimal versus natural coordinates

[49] makes a comparison between using a minimal versus a natural coordinate representation for the position and orientation of the aeroplane for a model of a balanced kites AWE system consisting of two aeroplanes. In the minimal coordinate representation, spherical coordinates and Euler angles are used to represent the position and orientation of the aeroplanes. In the natural coordinate representation, Cartesian coordinates and the direct cosine matrix are used to represent the position and orientation of the aeroplanes. The functions needed to solve the MHE problems are the model evaluation and the sensitivities with respect to all variables (labelled Jacobian). The derivative of their directional sensitivities with respect to all variables (labelled Hessian) is given for completeness. The comparison proposed in [49] considers for each of these three functions the number of nodes in their graph representations<sup>1</sup>, providing a measure of their symbolic complexity, and the typical computation time required for their evaluation. Table 6.3 shows the comparison for the model without aerodynamics. From the table it can be observed that despite the extra number of variables, the natural coordinate approach results in a significant reduction of the complexity and cost-of-evaluation of the model equations, Jacobian and Hessian of the system.

Table 6.4 shows the comparison for the model including a high-fidelity model of the aerodynamic forces and torques. It can be observed that even with the

<sup>1</sup>Each node in the graph representation of the model represents an elementary operation such as addition, multiplication, sine, cosine, . . . .

Model type	Model	Jacobian	Hessian
	#nodes & time	#nodes & time	#nodes & time
Natural	532 / 14.7 $\mu$ s	325 / 14.3 $\mu$ s	412 / 15.9 $\mu$ s
Minimal	1099 / 17.9 $\mu$ s	3302 / 35.6 $\mu$ s	15660 / 128.3 $\mu$ s
Ratio Minimal/Natural	2.1 / 1.22	10.2 / 2.5	38 / 8.1

Table 6.3: Model comparison without aerodynamic forces, the computational times are averaged over  $10^4$  function evaluations [49].

Model type	Model	Jacobian	Hessian
	#nodes & time	#nodes & time	#nodes & time
Natural	967 / 18.3 $\mu$ s	2127 / 32.2 $\mu$ s	30667 / 250.5 $\mu$ s
Minimal	2050 / 24.7 $\mu$ s	10546 / 87.3 $\mu$ s	169479 / 1273.8 $\mu$ s
Ratio Minimal/Natural	2.11 / 1.3	4.9 / 2.7	5.5 / 5.1

Table 6.4: Model comparison with aerodynamic forces, the computational times are averaged over  $10^4$  function evaluations [49].

introduction of a complex aerodynamic model, the advantage of the natural coordinate approach remains significant.

## 6.3 Outer estimation problem

The goal of the outer estimation problem is to provide the best possible estimate of the system state given measurements of the absolute measurement system and the IMU. It should provide state estimates at the frequency of the absolute measurements. Typically a Kalman filter is used for this estimation problem. Due to the nonlinear nature of the system and measurement models, MHE may be more appropriate to solve the estimation problem.

### 6.3.1 Polynomial approximation of the IMU measurements

To fuse the IMU measurements with the camera measurements, we can use the polynomial approximation of the IMU measurements that is outlined in Chapter 5. We first look at approximating the acceleration measurements with polynomials. Afterwards we consider the case of approximating the angular velocity measurements with polynomials.

To see how we can use the polynomial approximation for the acceleration measurements in MHE, we state the kinematic relation between the acceleration measured by the IMU ( $\bar{\mathbf{a}}_{\text{IMU}}$ ) and the acceleration of the aeroplane:

$$\ddot{\mathbf{r}} = RR_{\text{IMU}}^T(\bar{\mathbf{a}}_{\text{IMU}} - \mathbf{v}_a) + \dot{\delta}^2 \begin{bmatrix} x + r_{\text{Arm}} \\ y \\ 0 \end{bmatrix} - 2\dot{\delta} \begin{bmatrix} -\dot{y} \\ \dot{x} \\ 0 \end{bmatrix} - \ddot{\delta} \begin{bmatrix} -y \\ x + r_{\text{Arm}} \\ 0 \end{bmatrix} + \begin{bmatrix} 0 \\ 0 \\ g \end{bmatrix}, \quad (6.22)$$

with  $\bar{\mathbf{a}}_{\text{IMU}}$  the actual acceleration measurements and  $\mathbf{v}_a$  the noise on these measurements. This expression can be used to predict the aeroplane's velocity based on the acceleration measurements. Together with the expression from the dynamic model, we now have two expressions for  $\ddot{\mathbf{r}}$ .

One way to handle both expressions simultaneously is to use Equation (6.22) to integrate the velocity from time  $k$  to time  $k + 1$  given the acceleration measurements with  $\mathbf{v}_a$  set to zero, and put a penalty on the difference with the velocity estimate of the MHE for time  $k + 1$ . It would however be nontrivial on how to choose the penalty for this term since it depends on the nonlinear propagation of the covariance of the acceleration measurements.

In a different approach, we can integrate both expressions for  $\ddot{\mathbf{r}}$  independently and constrain the resulting velocities to be equal on each shooting node. We therefore add  $\dot{\mathbf{r}}_{\text{IMU}}$  (the aeroplane's velocity predicted by the IMU) to the state vector and add the constraints

$$\dot{\mathbf{r}}_k = \dot{\mathbf{r}}_{\text{IMU}_k} \quad (6.23)$$

to the MHE formulation. We are then still left with estimating  $\mathbf{v}_a$ , the measurement noise for the acceleration measurements. Because there are a lot of IMU measurements due to its high sampling frequency, this would result in a large scale optimisation problem. We therefore propose to approximate the acceleration measurements by polynomials as is done in Chapter 5.

For the polynomial approximation of the angular velocity measurements, we can use a similar strategy as for the acceleration measurements. We approximate the angular velocity measurements by:

$$\tilde{\boldsymbol{\omega}}_{\text{IMU}_k}(t) = \boldsymbol{\Gamma}_{\omega} \mathbf{p}_{\omega_k} \quad (6.24)$$

and add the following term to the objective:

$$\sum_{k=0}^N \frac{1}{\sigma_{\omega}^2} \| \mathbf{p}_{\omega_k} - \tilde{\mathbf{p}}_{\omega_k} \|_2^2, \quad (6.25)$$

in which  $\mathbf{p}_{\omega_k}$  are the polynomial coefficients for the approximation of the angular velocity measurements, which is discussed in detail in Section 5.5. The difference

with the acceleration measurements is that the angular velocity measurements are (if we do not consider the orientation of the IMU) direct measurements of the angular velocity of the aeroplane. Since the angular velocity of the aeroplane has to be continuous in time<sup>2</sup>, we state that this should be the case for the polynomial approximation by posing the continuity constraints

$$\tilde{\boldsymbol{\omega}}_{\text{IMU}_k}(T_s) = \tilde{\boldsymbol{\omega}}_{\text{IMU}_{k+1}}(0), \quad k = N_c - N, \dots, N_c - 1 \quad (6.26)$$

on the polynomials. This results in a continuous approximation of the angular velocity measurements. To relate this approximation to the actual angular velocity of the aeroplane, we put the constraints

$$\begin{aligned} \tilde{\boldsymbol{\omega}}_{\text{IMU}_k}(0) &= R_{\text{IMU}}^T \boldsymbol{\omega}_k, & k &= N_c - N, \dots, N_c - 1, \\ \tilde{\boldsymbol{\omega}}_{\text{IMU}_{N_c-1}}(T_s) &= R_{\text{IMU}}^T \boldsymbol{\omega}_{N_c} \end{aligned} \quad (6.27)$$

in the optimisation problem. The optimiser has the freedom to change  $\boldsymbol{\omega}$  by adding process noise, or to change  $\tilde{\boldsymbol{\omega}}_{\text{IMU}}$  by changing the polynomial coefficients and hence adding measurement noise to satisfy these constraints.

The complete estimation problem can now be written as:

$$\begin{aligned} \underset{\boldsymbol{x}, \boldsymbol{w}, \boldsymbol{p}}{\text{minimise}} \quad & \sum_{k=N_c-N}^{N_c-1} \| \boldsymbol{w}_k \|_{Q_k^{-1}}^2 + \sum_{k=N_c-N}^{N_c} \| \boldsymbol{y}_k - \boldsymbol{h}(\boldsymbol{x}_k) \|_{R_k^{-1}}^2 + \\ & \sum_{k=N_c-N}^{N_c} \frac{1}{\sigma_a^2} \| \boldsymbol{p}_{a_k} - \tilde{\boldsymbol{p}}_{a_k} \|_2^2 + \sum_{k=N_c-N}^{N_c} \frac{1}{\sigma_\omega^2} \| \boldsymbol{p}_{\omega_k} - \tilde{\boldsymbol{p}}_{\omega_k} \|_2^2 \end{aligned}$$

$$\begin{aligned} \text{subject to} \quad & \boldsymbol{x}_{k+1} = \boldsymbol{F}(\boldsymbol{x}_k, \boldsymbol{u}_k, \boldsymbol{p}_{a_k}, \boldsymbol{p}_{\omega_k}, \boldsymbol{w}_k), \\ & \boldsymbol{g}(\boldsymbol{x}_{N_c}) = \mathbf{0}, \end{aligned} \quad (6.28)$$

$$\dot{\boldsymbol{r}}_k = \dot{\boldsymbol{r}}_{\text{IMU}_k},$$

$$\tilde{\boldsymbol{\omega}}_{\text{IMU}_k}(0) = R_{\text{IMU}}^T \boldsymbol{\omega}_k,$$

$$\tilde{\boldsymbol{\omega}}_{\text{IMU}_k}(T_s) = \tilde{\boldsymbol{\omega}}_{\text{IMU}_{k+1}}(0),$$

$$\tilde{\boldsymbol{\omega}}_{\text{IMU}_{N_c-1}}(T_s) = R_{\text{IMU}}^T \boldsymbol{\omega}_N,$$

with  $\boldsymbol{F}$  the discrete form of the dynamic model presented in Section 6.2 and  $\boldsymbol{g}(\boldsymbol{x})$  the model invariants given by Equation (6.2), Equation (6.3) and Equation (6.13). Apart from the system model  $\boldsymbol{F}$  and consistency conditions  $\boldsymbol{g}$ , Problem (6.28) has  $6(N+1) + 3N + 3$  more constraints.

---

<sup>2</sup>Note that in reality this also holds for the acceleration of the aeroplane, but that the model does allow the acceleration to be discontinuous.

### 6.3.2 Assessment of estimation performance

The performance of an estimator can be assessed both in simulations and experiments. For simulations, the state estimates can be compared to the true state, and the root mean square of the error can serve as a performance measure. To obtain the simulation data used in this chapter, a Pseudo Random Binary Sequence (PRBS) is applied to angles of the ailerons and elevator to periodically excite the system at a constant tether length of 1.3 m and a rotation speed of 60 rpm. Input and output noise is added to the simulation according to the covariances defined in Section 6.3.3.

To assess the performance for experimental data, we usually cannot compare the state estimates with the true state. What we can do is compute the measurement prediction error, defined as the root mean square of the error between predicted measurements and the actual measurements. The predicted measurements are obtained by using the estimated state at a given time point together with measured inputs and simulate the system for a certain time. The measurement function then gives the predicted measurement for that time. The experimental data used in this chapter is obtained similarly to the simulation data, with a PRBS signal as setpoints for the angles of the ailerons and elevator, a tether length of 1.3 m and a rotation speed of 60 rpm. The data used for this chapter, together with a python-script to read the data, can be found in [43].

Note that the performance of an estimator is influenced by many characteristics, some related to the estimation method like estimator type or horizon length, some to the considered model. Of course, an estimator can only be as good as the model is.

### 6.3.3 MHE settings

Now that the general formulation of the estimator is defined, we need to specify the settings under which it runs. These settings include the weighting matrices used for the process and measurement noise, the order of polynomials for the acceleration and angular velocity measurements and the horizon length.

#### Weighting matrices

Table 6.5 lists the standard deviations used in the MHE. The standard deviations for the measurements are obtained from the sensor producer. For the IMU, these values are increased a bit to account for sensor misalignment and structural vibrations. Since in the current experiments the tether length is constant, the

Measurement	Unit	Standard deviation
Carousel angle	°	0.5
IMU acceleration	$\frac{m}{s^2}$	0.1
IMU angular velocity	$\frac{rad}{s}$	5
Marker positions	pixels	20
Tether length	mm	5
Tether velocity	$\frac{mm}{s}$	0.1
Aileron and elevator angle	°	0.05
Dimensionless disturbance forces	—	0.1
Dimensionless disturbance torques	—	0.01

Table 6.5: Standard deviations of process and measurement noise.

tether velocity has a very low standard deviation. The standard deviations for the disturbance forces and torques are set by the user. At the typical velocity the kite has during the experiments conducted for the results obtained in this chapter, the dimensionless disturbance forces and torques listed in Table 6.5, when scaled with the dynamic pressure and area of the kite, amount to actual disturbance forces and torques with a standard deviation of 1 N and 0.1 N m respectively.

### Polynomial interpolation

To define the order of the polynomial approximation for the IMU measurements, we first look at only the order for the acceleration measurements. For the angular velocity measurements, we downsample them to the frequency of the camera measurements, and add them as normal measurements for the aeroplane's angular velocity. Now we can vary the polynomial order for the acceleration measurements and look at how the performance changes in function of the polynomial order.

Table 6.6 shows the root mean square of the error in the estimates of position, orientation, velocity and angular velocity for different polynomial orders for a moving horizon estimator with a horizon length of 8 estimation intervals for a typical simulation. The error of the orientation is defined as the equivalent angle of rotation of  $R_{\text{true}}^T R_{\text{estimate}}$ .

We see from the data that doing a zeroth order approximation gives poor estimation performance compared to first order polynomials. Taking higher order approximations barely improves the estimation performance. If the system dynamics are faster compared to the sampling period, higher order

Type	Unit	Polynomial order					
		0	1	2	3	4	5
Position	mm	86.4	7.3	7.3	7.3	7.3	7.3
Orientation	°	11.1	0.8	0.8	0.8	0.8	0.8
Velocity	$\frac{\text{mm}}{\text{s}}$	788.0	72.0	72.0	71.0	71.0	71.0
Angular velocity	$\frac{\text{°}}{\text{s}}$	134.3	5.4	5.4	5.4	5.4	5.4

Table 6.6: Estimation performance, expressed as root mean square of the estimation error, for different orders of polynomials for approximation of acceleration measurements for MHE with a horizon length of 8 estimation intervals for a typical simulation.

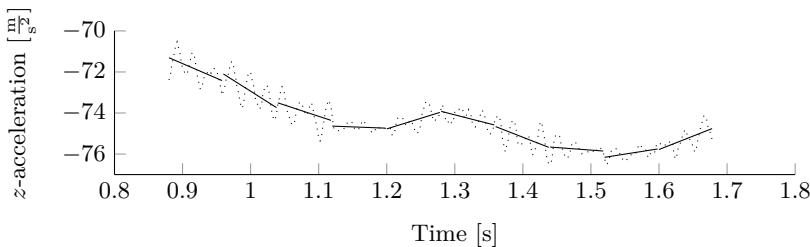


Figure 6.1: z-component of acceleration measurements (dotted line) and polynomials that fit these measurements (full line) for ten frames of one MHE solution.

approximations may provide a better estimation performance. Keeping in mind that higher order approximations result in more optimisation variables for the optimiser and hence longer execution times, we choose a first order approximation for the acceleration measurements. To give an impression of the approximation of the measurements, Figure 6.1 shows the z-component of a set of acceleration measurements from a typical experiment (dotted line) in combination with the polynomials that try to fit this acceleration (full line). Ten frames of one MHE solution are shown. Note that we are not aiming for the optimal fit of the polynomial on these measurements, but for an optimal fit in combination with the model and other measurements. There are jumps in the polynomials because there are no continuity constraints on the polynomials. Note that since the polynomials are modelling derivatives of the state, the state is not discontinuous.

Now we have defined the order of polynomials for the approximation of the acceleration measurements, we can look at the angular velocity measurements. Because of continuity constraints (6.26), zeroth order polynomials result in a constant angular velocity over the entire horizon, and are not suited. Table 6.7

Type	Unit	Polynomial order				
		1	2	3	4	5
Position	mm	38.9	9.9	7.2	7.2	7.2
Orientation	°	3.474	0.778	0.489	0.489	0.489
Velocity	$\frac{\text{mm}}{\text{s}}$	420.8	97.4	63.7	63.7	63.7
Angular velocity	$\frac{\text{°}}{\text{s}}$	36.94	10.35	3.98	3.98	3.98

Table 6.7: Estimation performance, expressed as root mean square of the estimation error, for different orders of polynomials for approximation of angular velocity measurements for MHE with a horizon length of 8 estimation intervals for a typical simulation.

shows how the estimation performance changes for different polynomial orders for the approximation of the angular velocity measurements. The order of the polynomials for the acceleration measurements is set to 1 and the horizon length is 8 estimation intervals.

Here we see that the performance does not improve for polynomial orders of three or higher. Compared to the MHE where we considered the angular velocity measurements as ‘*normal*’ measurements that are downsampled, the performance for the position and velocity estimate of the aeroplane is hardly better: the position error is nearly the same, from 7.3 mm without polynomial approximation for angular velocity to 7.2 mm with polynomial approximation and from 72  $\frac{\text{mm}}{\text{s}}$  to 63  $\frac{\text{mm}}{\text{s}}$  for the velocity error. There is some noticeable improvement of the estimation performance for the orientation and angular velocity: from an error of 0.8° to 0.49° for orientation and from 5.4  $\frac{\text{°}}{\text{s}}$  to 4  $\frac{\text{°}}{\text{s}}$  for the angular velocity. To achieve this performance gain, we need to use at least third order polynomials, which comes at a cost of a considerable increase of the execution time: for an MHE with a horizon length of 8 estimation intervals, first order polynomial approximation of the acceleration measurements and no polynomial approximation of the angular velocity measurements, the total execution time is 65.6 ms. For the same MHE, but with third order polynomial approximation for the angular velocity measurements, the total execution time increases to 151.3 ms. At the sampling period of 80 ms, this would no longer be real time feasible. Therefore we do not do a polynomial approximation of the angular velocity measurements, but downsample them to the frequency of the camera measurements. When more accuracy is needed, longer execution times are possible because e.g. the sampling frequency is lower, or when more processing power is available, one could consider approximating the angular velocity measurements by polynomials as well.

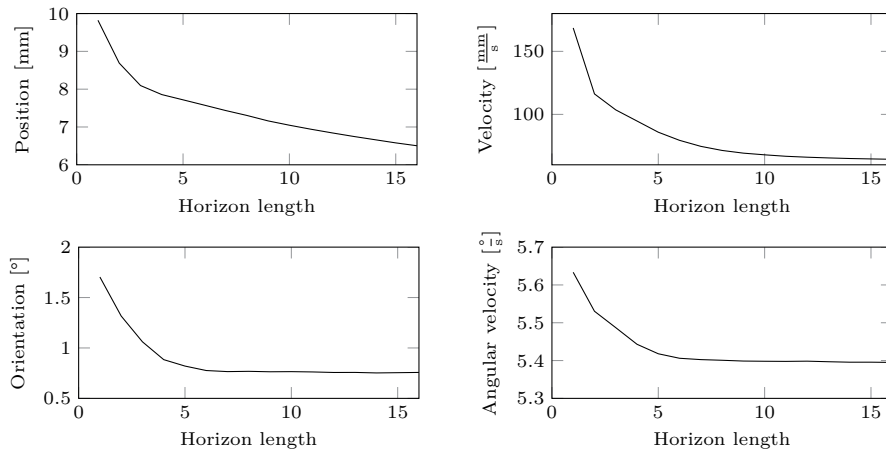


Figure 6.2: Root mean square of estimation error of MHE for position, orientation, velocity and angular velocity in function of horizon length.

### Horizon length

The selection of the horizon length is an important decision when formulating MHE. A short horizon may result in a poor estimation performance and a long horizon may be computationally too expensive. We can select the horizon length by looking at the estimation performance as a function of horizon length. Figure 6.2 shows the root mean square of the error in the estimate for position, orientation, velocity and angular velocity in function of horizon length.

We can see from Figure 6.2 that the performance rapidly increases as we increase the horizon length for short horizons. But from a horizon length of around 8 estimation intervals, there is little improvement in estimation performance for velocity, orientation and angular velocity.

The same behaviour is observed when we use experimental data. Figure 6.3 shows the 2-norm of the difference between the estimated and predicted state. Also here we see a drastic improvement in performance for short horizon lengths, but stagnation for horizon lengths longer than 8 estimation intervals.

Another thing to consider when determining the horizon length is the execution time of the MHE. Figure 6.4 shows the execution times for different horizon lengths obtained on a Dell Precision T1650 with an Intel Core i7-3770 Processor. The dotted line marks the sampling period of 80 ms of the camera system. On the computer used for the computations, a horizon length of 11 estimation intervals is the longest possible, with an execution time of 76 ms compared to

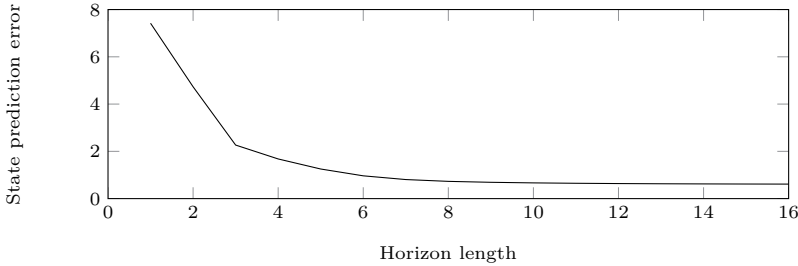


Figure 6.3: Experimental performance of MHE for different horizon lengths.

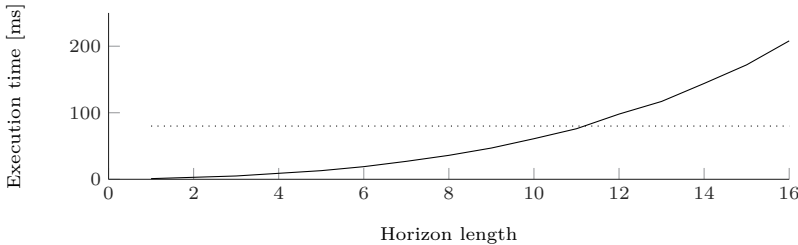


Figure 6.4: Execution times of MHE based on dynamic model for different horizon lengths.

the sampling period of 80 ms. Since a horizon length longer than approximately 8 estimation intervals does not give much better performance, it is best to take a horizon of 8 estimation intervals to limit the feedback delay as much as possible.

Using these settings, namely first order polynomials for the acceleration measurements, no polynomial approximation for the angular velocity measurements and an horizon length of 8, the number of optimisation variables in the MHE is equal to  $n_o = (N + 1)(n_x + n_v) + N(n_w + n_p)$ , with  $n_x = 26$ ,  $n_v = 20$ ,  $n_w = 10$  and  $n_p = 6$ . This results in a total of 542 optimisation variables.

The execution times for MHE are obtained using the **ACADO Code Generation** tool [94], which is part of the open source software package ACADO Toolkit [56]. It implements the real time iteration scheme, in which a single full Newton-type iteration is performed on each sampling time [26]. It exports code tailored for the specific problem which can significantly reduce the execution times. The MHE solver used in this chapter utilises qpOASES as QP-solver [36]. An alternative option would be to use a solver coupled to a structure exploiting QP-solver such as qpDUNES [41] which may further reduce the execution times [42].

### 6.3.4 Comparison with dynamic Kalman filters

To examine the performance of the MHE formulated above, we can compare it to an extended Kalman filter and an unscented Kalman filter. In the Kalman filters the IMU measurements are not projected onto polynomials, but are considered as normal measurement at their high sampling frequency.

#### Extended Kalman filter comparison

To overcome the problem with the invariants in the system model, the Kalman filter used for the comparison is the null space Kalman filter presented in Section 4.4.1.

Figure 6.5 shows the position and orientation error as a function of time for a typical simulation for an EKF (dotted line) and an MHE (full line) with a horizon length of 8 estimation intervals. The range on the  $y$ -axes is limited because the large initial error of the EKF would make the rest of the figure too small. The initial error reaches a value of about 270 mm for the position error and about  $13^\circ$  for the orientation error. Thus even for the same starting point, the EKF initially has a large initial error due to a bad guess of the initial state covariance. When the estimator settles, the estimation error of the EKF still is considerably larger than the error of the MHE. The root mean square of the estimate errors for this simulation of the EKF, after it has settled, are 31.3 mm and  $0.84^\circ$  for position and orientation respectively. For MHE, the root estimation errors are 11.2 mm and  $0.67^\circ$  position and orientation respectively. MHE thus has better start-up behaviour and average estimation performance compared to an extended Kalman filter.

#### Unscented Kalman filter comparison

Figure 6.6 shows the position and orientation error in function of time for UKF and MHE for the same simulation that is used for Figure 6.5, such that the results can be compared. Also for this figure, the ranges on the  $y$ -axes are limited because of the large initial error. The initial error reaches similar values as the EKF, about 270 mm for the position error and about  $13^\circ$  for the orientation error. The figure shows that the behaviour of the UKF is very similar to that of the EKF. The root mean square values of the estimate errors for this simulation of the UKF, after it has settled, are 31.2 mm and  $0.83^\circ$  for position and orientation respectively. The UKF has the same performance as the EKF, and for this system does not seem to offer an advantage over EKF.

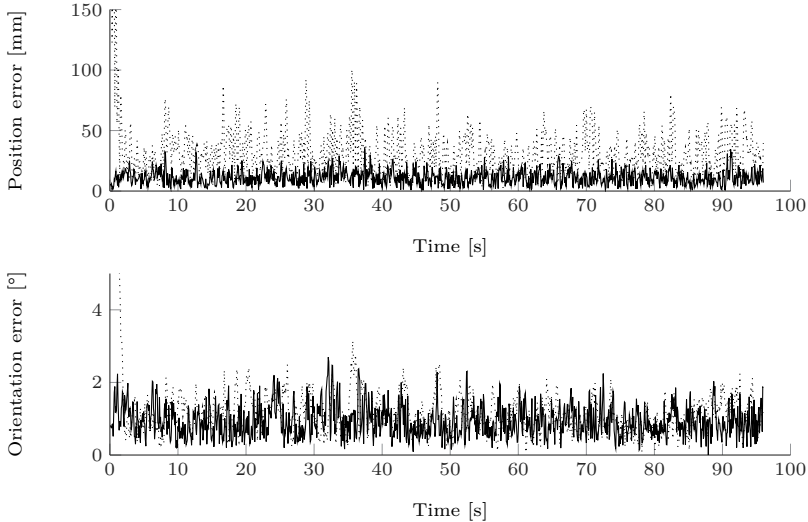


Figure 6.5: 2-norm of pose estimate error of EKF (dotted, upper, line) compared to MHE (full, lower, line).

### 6.3.5 Comparison with kinematic MHE

Often when doing inertial navigation with a fast IMU and a slow position measurement system, a kinematic model as the one presented in Section 5.2 is used. This has the advantage that no knowledge about the system dynamics and its characteristics is needed.

An MHE based on the kinematic model for our system is developed. The performance stopped improving from a horizon length of about 14 estimation intervals. To compare the performance of the kinematic MHE with the dynamic MHE, we have to use experimental data since the model used in the simulations is the dynamic model and hence they cannot truly be compared. We look at the prediction of measurements one sampling period forward in time, which we get by taking the state estimate, simulating forward in time, and then projecting this state prediction on the measurement of that time. Table 6.8 shows the root mean square of the prediction error of the camera measurements for different experiments for MHEs with a horizon length of 16 estimation intervals, which for both is more than long enough. We see that for all experiments, the MHE with a dynamic model of the system performs better than the MHE with a kinematic model, and can conclude that using the information the system model provides can significantly improve the performance of the estimator.

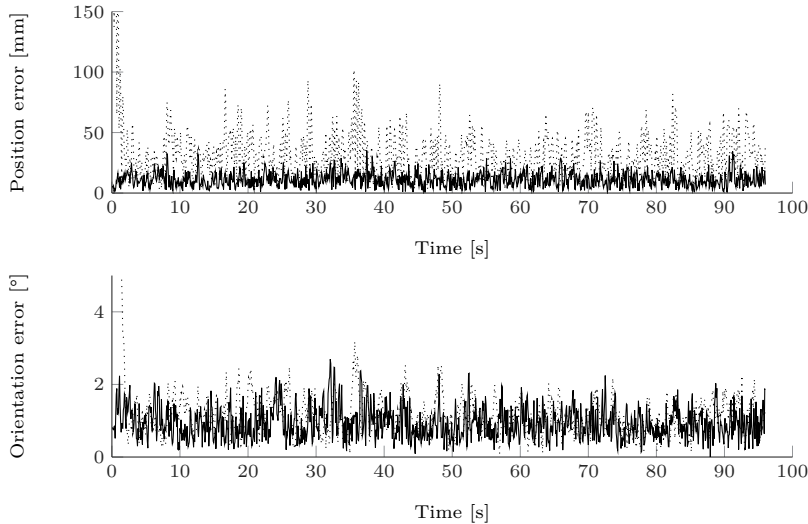


Figure 6.6: 2-norm of pose estimate error of UKF (dotted, upper, line) compared to MHE (full, lower, line).

PRBS signal on	Dynamic model	Kinematic model
None	46.2	78.2
None	53.1	93.8
Ailerons	72.7	334.9
Ailerons	73.5	258.6
Elevators	71.7	190.9
Elevators	70.6	179.2
Both	71.7	129.2
Both	86.2	284.8

Table 6.8: Root mean square of marker prediction error in pixels for different experiments for MHEs with a horizon length of 16 estimation intervals.

An advantage of the kinematic model, compared to the dynamic model, is its simplicity. Figure 6.7 shows the execution times of MHE based on a kinematic model on the same computer as the timings obtained in Figure 6.4. The execution times are a factor 2 to 3 lower for the same horizon lengths, which can be beneficial for systems where the processing power is limited or where the dynamic model is even more complex, resulting in longer execution times.

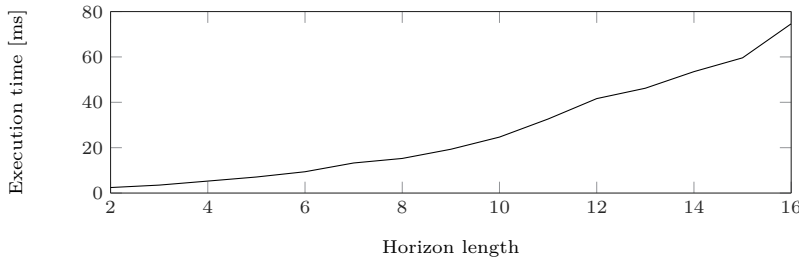


Figure 6.7: Execution times of MHE based on kinematic model for different horizon lengths.

## 6.4 Dead reckoning using fast MHE

After the state estimate has been updated using the absolute measurement, i.e. the camera measurement for our system, typically ‘*dead reckoning*’ is done to give state estimates at a faster rate. In dead reckoning, the state is updated by kinematic integration of the IMU measurements. However, since a system model is available, it would be better if we could use this information as well. Therefore we propose to use a second, fast, MHE that runs in between two updates of the outer estimation problem.

### 6.4.1 Setup

The setup of the inner MHE is similar to the one for the outer MHE, except that there are no camera measurements. Instead, we use an arrival cost based on the outer MHE’s state estimate. The integrator runs over a shorter time, thus can use fewer integrator steps. We run MHE with sampling time  $T_s^{\text{inner}}$  from  $t_k$  to  $t_{k+1} - T_s^{\text{inner}}$ . Running to  $t_{k+1}$  is not needed since the outer MHE provides the state estimate for that time.

### 6.4.2 MHE settings

The weighting matrices used in the MHE are the same as those used in the outer MHE, listed in Table 6.5. The arrival cost is computed by inverting the covariance of the state estimate of the outer MHE, which is computed according to [67]. Note that to invert the covariance matrix, we do a subspace projection since due to the model invariants, the covariance of the state estimate is positive semi-definite.

Horizon length	Sampling period [ms]	Execution time [ms]
1	40	0.8
3	20	3.3
4	16	5.1
7	10	13.5
9	8	22.6
19	4	151.4

Table 6.9: Execution times and sampling periods of inner MHE for different horizon lengths.

Type	Unit	Inner MHE	Dead reckoning
Position	mm	12.0	12.3
Orientation	$^\circ$	0.74	0.77
Velocity	$\frac{\text{mm}}{\text{s}}$	102.3	100.0
Angular velocity	$\frac{\text{°}}{\text{s}}$	5.2	5.7

Table 6.10: Average prediction error of dead reckoning compared to inner MHE.

For the polynomial interpolation, polynomials of order 1 are used for the acceleration measurements and no polynomials are used for the angular velocity measurements, as is done for the outer MHE.

The horizon length for this MHE determines the sampling frequency of the MHE. A horizon of  $N$  results in a sampling period  $T_{\text{inner}}$  of  $\frac{T_s}{N+1}$ . We keep the number of IMU measurements per frame for the inner MHE a whole number. The outer MHE has 40 IMU measurements per frame. Therefore for the inner MHE 1, 2, 4, 5, 8, 10 or 20 IMU measurements per frame are possible. Table 6.9 lists the execution times for the MHEs with a different horizon length and the corresponding sampling periods obtained on the same Dell Precision T1650 with an Intel Core i7-3770 Processor. We can see from Table 6.9 that the fastest MHE that is real time feasible on this PC has a sampling period of 16 ms and uses 8 IMU measurements per frame.

### 6.4.3 Results

To assess the performance of the inner MHE, we compare it to the typical estimation approach, dead reckoning. For dead reckoning, the state is updated by kinematically integrating the IMU measurements. Table 6.10 compares the estimation performance of a typical simulation between dead reckoning and the inner MHE using 8 IMU measurements per frame. We see from Table 6.10 that the inner MHE performs slightly better than the typical dead reckoning,

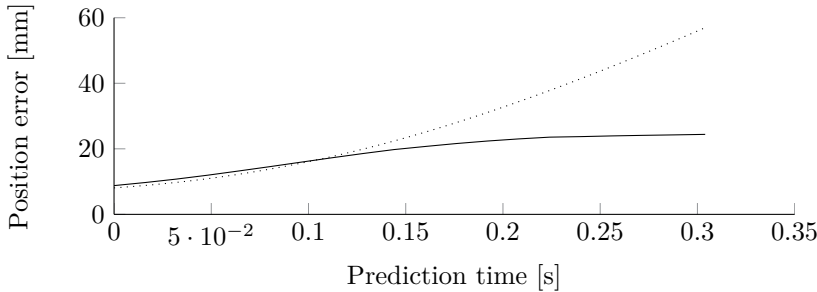


Figure 6.8: Root mean square of position estimate error in function of prediction time for MHE (full line) and dead reckoning (dotted line).

but the difference is small. The benefits of combining the IMU measurements with the system model become much more obvious when we need to update the state with only IMU measurements for a longer time. Figure 6.8 shows the root mean square of the error in position estimates when the inner MHE and dead reckoning are used for a longer time. We see from Figure 6.8 that for short prediction times, the performance of MHE and dead reckoning is similar, but when the state is predicted for a longer time, MHE performs much better than dead reckoning. For systems where the outer estimator runs at a longer sampling time, because for example it uses a GPS that runs at only 1 Hz, it is thus beneficial to replace dead reckoning with MHE.

If we want to compare MHE and dead reckoning on experimental data, we can again look at the prediction of the marker measurements obtained when we run the inner estimation for one sampling period of the outer estimation problem. Figure 6.9 shows the root mean square of the prediction error of the camera measurements for MHEs and dead reckoning for a typical experiment. From the figure we see again that MHE performs similar to dead reckoning for short prediction times, but for longer prediction times it performs better.

## 6.5 Closed loop control experiments

The purpose of the control experiments is to show feasibility of running a combination of MHE and NMPC in a closed loop on the indoors carousel. Section 6.5.1 first gives a short introduction to NMPC and Section 6.5.2 presents some results of flight experiments.

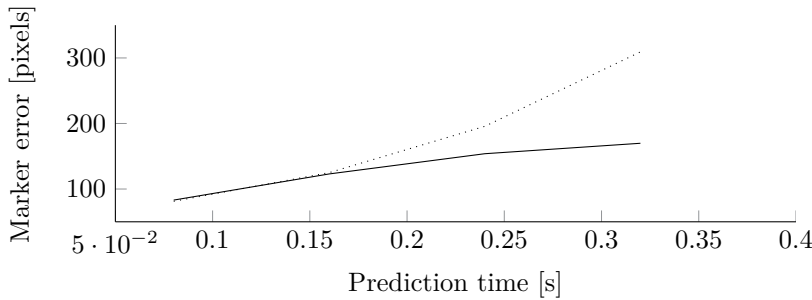


Figure 6.9: Root mean square of marker prediction error for MHE (full line) and dead reckoning (dotted line).

### 6.5.1 Nonlinear Model Predictive Control

Nonlinear Model Predictive Control is an ideal framework when dealing with the control of nonlinear, constrained systems, and has been previously applied to airborne wind energy systems in e.g. [50, 58, 55, 38]. At each sampling interval we look for the control action that optimises a certain objective function over a time horizon, subject to a combination of (nonlinear) dynamical, input, and state constraints. The objective can for example be to track a certain reference trajectory or the average power generation of the AWE system. The first part of this optimal control action is then applied to the system, and on the next sampling interval the problem is reformulated and solved again.

In our setup, the objective is to track a precomputed reference state trajectory. The following optimisation problem is solved at each sampling time:

$$\begin{aligned}
 \text{minimise}_{\mathbf{x}, \mathbf{u}} \quad & \sum_{k=N_c}^{N_c+N-1} \|\mathbf{x}_k - \mathbf{x}_k^{\text{ref}}\|_V^2 + \sum_{k=N_c}^{N_c+N-1} \|\mathbf{u}_k - \mathbf{u}_k^{\text{ref}}\|_W^2 + \\
 & \|\mathbf{x}_{N_c+N} - \mathbf{x}_{N_c+N}^{\text{ref}}\|_S^2 \\
 \text{subject to} \quad & \mathbf{x}_{k+1} = \mathbf{F}(\mathbf{x}_k, \mathbf{u}_k), \\
 & \underline{\phi}_a \leq \phi_{a_k} \leq \bar{\phi}_a, \\
 & \underline{\phi}_e \leq \phi_{e_k} \leq \bar{\phi}_e, \\
 & \underline{\mathbf{u}} \leq \mathbf{u}_k \leq \bar{\mathbf{u}}, \\
 & \ddot{\delta}_k = 0, \\
 & \mathbf{x}_{N_c} = \mathbf{x}_{N_c}^{\text{est}},
 \end{aligned} \tag{6.29}$$

where  $\mathbf{x}^{\text{ref}}$  is the reference trajectory for the state the system has to follow, and  $\mathbf{u}^{\text{ref}}$  is the reference for the control input that, when applied in simulation to the system model, results in the reference state being tracked.  $V$ ,  $W$  and  $S$  are weighting matrices for the tracking objective,  $\underline{\phi}_a$ ,  $\bar{\phi}_a$ ,  $\underline{\phi}_e$ ,  $\bar{\phi}_e$ ,  $\underline{\mathbf{u}}$  and  $\bar{\mathbf{u}}$  are lower and upper limits on the control surface angles and control inputs. The angular velocity of the carousel is not controlled by the NMPC and is constant.  $\mathbf{x}_{N_c}^{\text{est}}$  is the state estimate for the current time provided by the MHE. The model invariants are not part of the constraints, because the state estimate  $\mathbf{x}_{N_c}^{\text{est}}$  given by the MHE already satisfies these conditions.

The components of  $V$  that relate to  $\dot{\phi}_a$  and  $\dot{\phi}_e$  are set to zero, so that the angle of the control surfaces is not penalised. A weight on  $\dot{\phi}_a$  and  $\dot{\phi}_e$  ensures that the variation of the control input is not too large, which benefits the life span of the actuators. The terminal cost matrix  $S$  is computed by solving the Riccati equation for the system linearised around the reference state at the end of the prediction horizon. The horizon of the controller is chosen to be 1 s, with a sampling period of 0.1 s. Like for the MHE, this controller is implemented in the ACADO Toolkit and specialised C-code is exported using the ACADO Code Generation tool.

### 6.5.2 Flight experiments and observations

The first flight experiments on the carousel immediately showed a huge advantage of the rotation start: the system is open loop stable at start-up. This observation is indeed predicted by the model; the linearised system also shows this stability. This open loop stability simplifies the task of the controller during start-up and landing.

Several closed-loop experiments are performed on this test setup. The goal of these experiments is to test advanced estimation and control techniques, developed within the Highwind project. In this first phase, these experiments do not aim at achieving a high performance, but rather on showing that these techniques can be used in practice on the developed set-up.

The results shown here come from an experiment at a constant carousel velocity of 60 rpm that had a duration of 2.6 hours, during which the setpoint for the controller is periodically toggled between two values for a constant tether length of 1.3 m. The Model Predictive Controller presented in Section 6.5.1 is used in these experiments. The references are computed by finding the steady state of the aeroplane, given a certain feasible height  $z$ . The heights are chosen here to be 0.118 m and 0.06 m below the arm level. The height of 0.06 m is the height the aeroplane would have when all control surfaces are neutral. The controller has to track one reference for 6 s at a time. Then the Trajectory generator transitions to the other reference. The transition from one reference to the other is done by a linearly interpolated ramp in the height state with a duration of 0.5 s.

Figure 6.10 shows the closed-loop tracking performance for the roll angle, angular velocity around the  $z$ -axis of the aeroplane and for the height  $z$ . The roll is defined here to be 0° when the wing is vertical. From the figure, it is clear that there is an oscillation that is not controlled. These oscillations are also present when the controller is turned off and the system ran in open loop. Figure 6.11 shows the same variables for an open loop experiments with all control surfaces set to neutral, and shows oscillations similar to those in Figure 6.10. We suspect these oscillations are caused by the turbulence of the plane flying through its own wake. Since there is no direct yaw control via a rudder and the aeroplane has a small vertical stabiliser, there is little yaw damping. This makes the control of these oscillations hard or even impossible. Controlling these oscillations is not the goal of the current experiments. The figures show that, except for the oscillations described before, the tracking behaviour for the roll and angular velocity is reasonable. The tracking behaviour for the height is worse. This is related to the fact that the height is only indirectly controlled via the orientation.

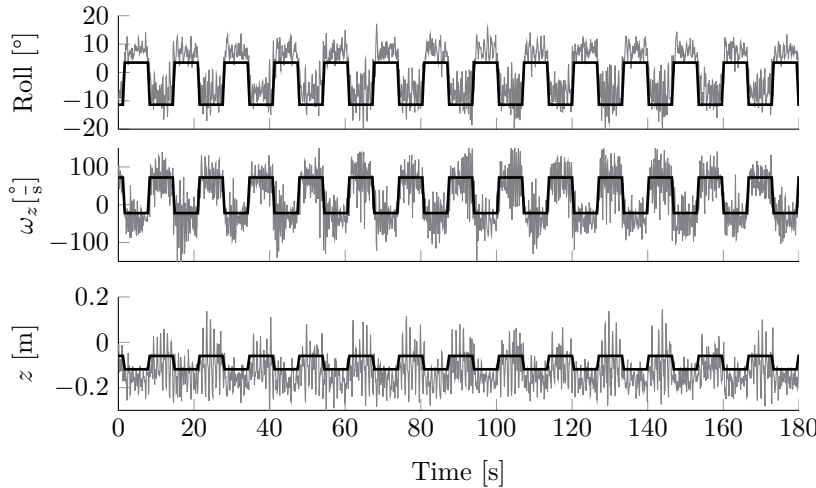


Figure 6.10: Closed loop tracking behaviour for roll, angular velocity around the  $z$ -axis and height. Reference in black, estimated variables in grey [47].

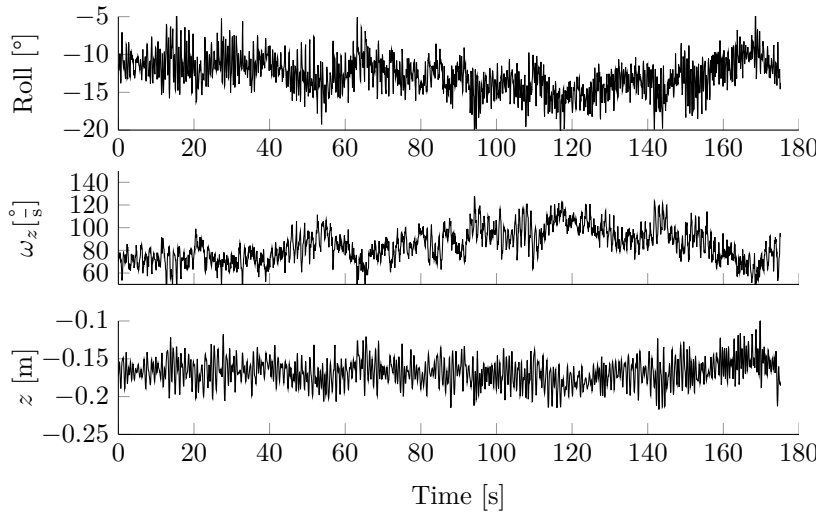


Figure 6.11: Open loop behaviour for roll, angular velocity around the  $z$ -axis and height.

Table 6.11 shows the low execution time of the auto-generated C-code. At each sampling time, one Real-Time Iteration (RTI) is done for both the MHE and

MHE	
	Average
Preparation phase	3.76 ms
MHE Estimation phase	0.75 ms
Overall execution time 4.51 ms	
MPC	
Preparation phase	3.56 ms
MPC Feedback phase	0.50 ms
Overall execution time 4.06 ms	

Table 6.11: Execution times of the MHE and NMPC.

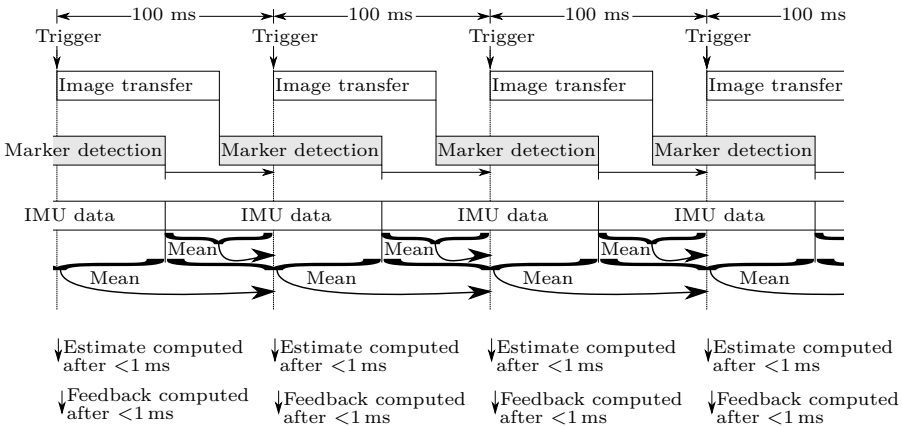


Figure 6.12: Timing diagram of the closed loop system.

the NMPC. The average execution time is 4.51 ms for the MHE and 4.06 ms for the NMPC. The average feedback time is 0.75 ms and 0.50 ms for the MHE and NMPC respectively. To provide the feedback control signal, only the feedback phases need to be completed. It thus takes an average of 1.25 ms to provide the feedback control signal after the measurement is taken. After the feedback is applied, the preparation phases are done in the remaining time. Execution times are measured with OROCOS timer services. Those services internally use the Linux function `clock_gettime()`, which provides resolution in the nanosecond range. Figure 6.12 shows a timing diagram of the closed loop system.

## 6.6 Conclusion

This chapter developed a moving horizon estimator to fuse measurements from an IMU with measurements from a stereo vision system using a dynamic model of the system. We showed that approximating the acceleration measurements with linear interpolations improves the estimation performance, but higher order approximations are not necessary. For the angular velocity measurements, at least third order approximations would be needed to improve the estimation performance, which is at the cost of more computation time.

The developed MHE is compared with both an extended and unscented Kalman filter. MHE is shown to have both a better start-up behaviour and a better average estimation performance than both the EKF and the UKF.

A comparison is made between the MHE based on the dynamic model and an MHE based on a kinematic model, such as the estimator developed in Chapter 5. The comparison is done using experimental data. It is shown that a significant increase in estimation performance can be achieved when using the estimator based on the dynamic model. The MHE based on the kinematic model has the advantage of a lower execution time, which can be beneficial when less processing power is available.

Note that this conclusion, that an estimator based on a dynamic model outperforms an estimator based on a kinematic model, is not true for all systems. This can be the case when the dynamic model offers a good approximation of the system behaviour. It then offers an extra layer of filtering to the measurements. When a bad system model is used, it may decrease the estimation performance.

To achieve state estimates at a higher frequency, a second inner MHE is proposed to replace the typical dead reckoning. This strategy proved to have the same performance as dead reckoning for short prediction times, but performed better than dead reckoning for a long prediction time. For systems where the absolute measurement system has a slower sampling frequency, e.g. a GPS system, or for systems where long prediction times are needed, this strategy can thus be helpful to provide more accurate state estimates.

The chapter further presented a tracking controller based on NMPC that runs in a closed-loop system together with MHE to control the aeroplane on the indoors test set-up. Both the MHE and NMPC are implemented using the ACADO Code Generation Tool that exports C-code tailored to the specific problem. The execution time is below 5 ms for both MHE and NMPC, with an estimation/feedback phase lower than 1 ms. The results of a closed-loop experiment are given. The controller is able to control the roll of the aeroplane reasonably well, but the tracking behaviour for the height of the aeroplane is

much worse. The goal of this experiment is to show feasibility of closed-loop control on the indoors set-up. Further actions include the implementation of the more advanced estimator, such as the one the MHE described in Chapter 6, which runs at a higher sampling frequency, and simultaneously increasing the sampling frequency of the controller. Different NMPC implementations can be tested to see which is best suited for this type of system.



# Chapter 7

## Concluding remarks

This chapter summarises and lists the contributions of the thesis and presents suggestions for future research directions.

### 7.1 Summary of the thesis

Part I of this thesis focussed on the design and development of experimental test set-ups for airborne wind energy, a technology that is capable of capturing wind energy at higher altitudes using less material than conventional wind turbines. The cost of these savings is that AWE systems need to be constantly controlled to stay airborne. Part II therefore focussed on the development of state estimation algorithms based on moving horizon estimation.

Launch and landing of AWE systems can be done using the rotation start, for which an indoors and outdoors test set-up is developed in Chapter 2 and Chapter 3 respectively. The basis of the indoors set-up is designed and realised during the master thesis of K. Geebelen and J. Gillis [45]. The contributions to the indoors test set-up in this thesis are the further development of the stereo vision system, on-board electronics and software system. The outdoors set-up is developed in collaboration with M. Clinckemaillie, J. Stuyts and W. Vandermeulen during their master theses [16, 88]. The main contributions are the design for a balanced kites set-up which formed the basis for the design of a single kite set-up. This single kite set-up consisting of a carousel and winch is completely designed and built. This chapter also detailed the design of a line angle sensor that measures the angle of the tether with the arm.

Part II of this thesis covers the estimation of the aeroplane's position and orientation. One of the contributions of this part is the development of a moving horizon estimator based on a kinematic model that fuses the IMU measurements with the measurements of the stereo vision system. It does this in a robust manner with respect to outliers in the camera measurements by employing the Huber penalty function. To use the IMU measurements at their high sampling frequency, without becoming too computationally expensive, the MHE approximates them using polynomials. Another contribution in this part is the development of a moving horizon estimator based on a dynamic model to fuse the measurements. A thorough comparison between different formulations and other estimation techniques is done. This study showed that linear approximations of the acceleration measurements improves the estimation performance, but higher order approximations do not further improve the estimation performance. For the angular velocity measurements, third order polynomials are needed to achieve a performance increase for the considered system, at the cost of a higher computation time. Based on both simulation and experimental data, the developed estimator is compared with an extended and an unscented Kalman filter and shown to have a better start-up behaviour and average estimation performance than both the EKF and the UKF. A comparison of the developed estimator with an MHE based on a kinematic model teaches us that using the extra information present in the dynamic model can considerably increase estimation performance. A third contribution is the development of an alternative to dead reckoning using a second inner MHE is also presented. This strategy proved to be beneficial when long prediction times are needed. A final contribution of Part II is the application of NMPC and MHE on the indoors set-up, showing the feasibility of closed-loop control experiments using a simplified version of the developed estimator.

## 7.2 Future work

Future work on the outdoors test set-up includes the further development of the aeroplane that is used for flight experiments. Once the aeroplane is completed, the algorithms developed in Part II can be implemented and tested on the outdoors set-up. They have to use the line angle sensor instead of the stereo vision system for absolute measurements, but other than that no big changes need to be made to the existing algorithms. Before commencing experiments that involve the aeroplane, it is safer to experiment with a dead weight such as a ball on a string to build up experience in the operation of the set-up and ensure all sensors and actuators on the carousel work properly. Simple strategies to control the motion of the ball using measurements of the line angle sensor and

the carousel and winch motor as actuators can be implemented to achieve a first closed-loop system on the set-up.

Once the outdoors aeroplane is completed and equipped with the necessary sensors, the first control experiments with the aeroplane can be carried out. Initially this should be done indoors or on days when there is little to no wind. A first step is to fly circular trajectories on a short tether and control e.g. the height of the aeroplane as is done on the indoors test set-up in Section 6.5.2. By increasing the tether length while still flying circular trajectories on the outdoors carousel, the effect of the aerodynamic forces increase as the rotational forces decrease, resulting in more control authority. Step by step, the complexity of the reference trajectories can be increased. The step towards flying outdoors in windy conditions can be made, which probably leads to the necessity to estimate the wind speed and direction in the estimator. A pitot tube on the aeroplane can help for this purpose. Although already realised in simulation in [54], the transition from the circular trajectory to crosswind flight still needs to be realised in practice and will be a major achievement in the project. Control strategies for launching, crosswind flight and landing need to be developed, implemented and validated on the set-up.

On the algorithmic side of MHE, further developments include the inclusion of an arrival cost in the objective function to possibly reduce the horizon length and thus computational effort. A better approach to handle the polynomial approximation of the IMU measurements would be to use integrators that provide continuous output, such as the one presented in [78, 79], since it would not require the extra states that are now added. An interesting development would be the estimation of the wind field. Current models assume a uniform wind field of which the wind speed is only dependent on height. In reality however, the wind speed and direction is dependent on the position as well, and there can be large turbulent regions that can have a lower or higher wind speed. Since the power that can be extracted is proportional to the cube of the wind speed, it can be very interesting to fly in those regions. To enable this, new sensors that are e.g. based on LIDAR [85] need to be developed that map the complete wind field around the aeroplane. The resulting wind field estimate can then also be used to predict the wind in front of the aeroplane such that the controller can already anticipate to it.

For AWE in general, many challenges are still ahead of us. A lot of groups have already shown automated operation of their prototypes, but these still provide only a few dozen kilowatt of generated power, which is far from the multi-megawatt wind turbines that are being built today. Makani Power's latest developments focus on a 600 kW Energy kite [71], which is already an order of magnitude closer to current wind turbines. Once realised, their Energy kite will give more insight to the entire field of AWE on the looks, size and operation

of an AWE system that is closer to the commercial scale. Once a system of megawatt-scale is operational and shown to be safe and reliable, it may attract the attention of the general public, which could accelerate the developments of the entire field.

# Bibliography

- [1] AMPYX POWER. Ampyx Power Website. <http://www.ampyxpower.com/>. Accessed: 20–03–2015. Cited on page 10.
- [2] ANDERSSON, J., ÅKESSON, J., AND DIEHL, M. CasADi – A symbolic package for automatic differentiation and optimal control. In *Recent Advances in Algorithmic Differentiation* (Berlin, 2012), S. Forth, P. Hovland, E. Phipps, J. Utke, and A. Walther, Eds., Lecture Notes in Computational Science and Engineering, Springer. Cited on page 91.
- [3] ARCHER, C., AND CALDEIRA, K. Global assessment of high-altitude wind power. *Energies* 2 (2009), 307–319. Cited on page 3.
- [4] ARCHER, C., AND JACOBSON, M. Geographical and seasonal variability of the global practical wind resources. *Applied Geography* 45 (2013), 119–130. Cited on page 3.
- [5] BAR-SHALOM, Y., LI, X., AND KIRUBARAJAN, T. *Estimation with Applications to Tracking and Navigation*. Wiley Interscience, 2001. Cited on page 97.
- [6] BENINI, A., MANCINI, A., AND LONGHI, S. An IMU/UWB/Vision-based Extended Kalman Filter for Mini-UAV Localization in Indoor Environment using 802.15.4a Wireless Sensor Network. *Journal of Intelligent & Robotic Systems* 70, 1-4 (2013), 461–476. Cited on page 97.
- [7] BJÖRCK, A. *Numerical Methods for Least Squares Problems*. SIAM, 1996. Cited on page 87.
- [8] BOCK, H., AND PLITT, K. A multiple shooting algorithm for direct solution of optimal control problems. In *Proceedings 9th IFAC World Congress Budapest* (1984), Pergamon Press, pp. 242–247. Cited on page 71.
- [9] BOYD, S., AND VANDENBERGHE, L. *Convex Optimization*. University Press, Cambridge, 2004. Cited on page 90.

- [10] BREUKELS, J. Kite launch using an aerostat. Tech. rep., Delft University of Technology Faculty of Aerospace Engineering The Netherlands, 2007. Cited on pages 12 and 13.
- [11] BREUKELS, J., SCHMEHL, R., AND OCKELS, W. Aeroelastic simulation of flexible membrane wings based on multibody system dynamics. In *Airborne Wind Energy*, U. Ahrens, M. Diehl, and R. Schmehl, Eds. Springer, 2013. Cited on page 5.
- [12] BRUYNINCKX, H. Open robot control software: the OROCOS project. In *Robotics and Automation, 2001. Proceedings 2001 ICRA. IEEE International Conference on* (2001), vol. 3, IEEE, pp. 2523–2528. Cited on page 29.
- [13] BRUYNINCKX, H., AND DE SCHUTTER, J. *Introduction to Intelligent Robotics*. KU Leuven, 2001. Cited on page 79.
- [14] CANALE, M., FAGIANO, L., AND MILANESE, M. Power kites for wind energy generation - fast predictive control of tethered airfoils. *IEEE Control Systems Magazine* 27 (2007), 25–38. Cited on page 5.
- [15] CHOUKROUN, D., BAR-ITZHACK, I., AND OSHMAN, Y. Optimal-request algorithm for attitude determination. *Journal of Guidance Control and Dynamics* 27, no. 3 (2004). Cited on pages 76 and 97.
- [16] CLINCKEMAILLIE, M., GEEBELEN, K., DIEHL, M., AND VANDEPITTE, D. An experimental set-up for energy generation using balanced kites. Master's thesis, KU Leuven, 2012. Cited on pages 20, 33, 35, 37, 38, 39, 40, 43, 49, and 129.
- [17] COSAERT, D., ELST, K., GEEBELEN, K., DIEHL, M., SWEVERS, J., AND VANDEPITTE, D. Design of a winch for modeling and control of the tethered flight of a model airplane. Master's thesis, KU Leuven, 2011. Cited on page 25.
- [18] CRASSIDIS, J., AND MARKLEY, F. Unscented filtering for spacecraft attitude estimation. *Journal of Guidance Control and Dynamics* 26, 4 (2003), 536–542. Cited on page 97.
- [19] CRASSIDIS, J., MARKLEY, F., AND CHENG, Y. Survey of nonlinear attitude estimation methods. *Journal of Guidance Control and Dynamics* 30, 1 (2007), 12–28. Cited on pages 76 and 97.
- [20] DANISH WIND INDUSTRY ASSOCIATION. A Wind Energy Pioneer: Charles F. Brush, 2003. Cited on page 3.

[21] DE MARINA, H., PEREDA, F., GIRON-SIERRA, J., AND ESPINOSA, F. UAV Attitude Estimation Using Unscented Kalman Filter and TRIAD. *IEEE Transactions on Industrial Electronics* 59, 11 (2012), 4465–4474. Cited on page 97.

[22] DE TIJD. Onderzoek naar sabotage doel 4 richt zich op terrorisme. [http://www.tijd.be/politiek\\_economie/belgie\\_algemeen/Onderzoek\\_naar\\_sabotage\\_Doel\\_4\\_richt\\_zich\\_op\\_terrorisme.9576268-4002.art?highlight=doel%204](http://www.tijd.be/politiek_economie/belgie_algemeen/Onderzoek_naar_sabotage_Doel_4_richt_zich_op_terrorisme.9576268-4002.art?highlight=doel%204). Accessed: 20–03–2015. Cited on page 2.

[23] DE TIJD. Winter in met 2 reactoren minder. [http://www.tijd.be/nieuws/ondernemingen\\_energie/Winter\\_in\\_met\\_2\\_reactoren\\_minder.9242227-3093.art?ckc=1](http://www.tijd.be/nieuws/ondernemingen_energie/Winter_in_met_2_reactoren_minder.9242227-3093.art?ckc=1). Accessed: 20–03–2015. Cited on page 2.

[24] DEADMAN, E., HIGHAM, N., AND RALHA, R. Blocked Schur algorithms for computing the matrix square root. In *Applied Parallel and Scientific Computing*. Springer, 2013, pp. 171–182. Cited on page 68.

[25] DIEHL, M. *Airborne Wind Energy*. Springer, 2013. Cited on pages 6 and 8.

[26] DIEHL, M., BOCK, H., AND SCHLÖDER, J. A real-time iteration scheme for nonlinear optimization in optimal feedback control. *SIAM Journal on Control and Optimization* 43, 5 (2005), 1714–1736. Cited on pages 72 and 114.

[27] DIEHL, M., BOCK, H., SCHLÖDER, J., FINDEISEN, R., NAGY, Z., AND ALLGÖWER, F. Real-time optimization and Nonlinear Model Predictive Control of Processes governed by differential-algebraic equations. *Journal of Process Control* 12, 4 (2002), 577–585. Cited on page 72.

[28] DIEHL, M., FINDEISEN, R., ALLGÖWER, F., BOCK, H., AND SCHLÖDER, J. Nominal Stability of the Real-Time Iteration Scheme for Nonlinear Model Predictive Control. *IEE Proc.-Control Theory Appl.* 152, 3 (2005), 296–308. Cited on page 73.

[29] ENERGY TRANSITION. The German Energiewende. <http://energytransition.de/>. Accessed: 20–03–2015. Cited on page 2.

[30] ENERKITE. Enerkite - airborne wind energy. <http://www.enerkite.de/en/>. Accessed: 20–03–2015. Cited on page 9.

[31] ERC HIGHWIND PROJECT. ERC Highwind Project Website. <http://www.highwind.be>. Accessed: 20–03–2015. Cited on page 18.

[32] EUROPEAN COMMISION. Europe 2020. [http://ec.europa.eu/europe2020/index\\_nl.htm](http://ec.europa.eu/europe2020/index_nl.htm). Accessed: 20–03–2015. Cited on page 2.

- [33] EUROPEAN COMMISION. Report from the commission to the european parliament and the council progress towards achieving the kyoto and eu2020 objectives. Tech. rep., Europa, 2014. Cited on page 2.
- [34] FAGIANO, L., CANALE, M., MILANESE, M., AND LAFACE, P. *Control of Tethered Airfoils for High-Altitude Wind Energy Generation*. PhD thesis, Politecnico di Torino, 2009. Cited on page 5.
- [35] FAGIANO, L., HUYNH, K., BAMIEH, B., AND KHAMMASH, M. On Sensor Fusion for Airborne Wind Energy Systems. *IEEE transactions on control systems technology* (2014). Cited on page 97.
- [36] FERREAU, H. qpOASES – An Open-Source Implementation of the Online Active Set Strategy for Fast Model Predictive Control. In *Proceedings of the Workshop on Nonlinear Model Based Control – Software and Applications, Loughborough* (2007), pp. 29–30. Cited on page 114.
- [37] FERREAU, H. *Model Predictive Control Algorithms for Applications with Millisecond Timescales*. PhD thesis, K.U. Leuven, 2011. Cited on page 73.
- [38] FERREAU, H., HOUSKA, B., GEEBELEN, K., AND DIEHL, M. Real-time control of a kite-carousel using an auto-generated nonlinear MPC algorithm. In *Proceedings of the IFAC World Congress* (2011). Cited on page 121.
- [39] FERREAU, H., KRAUS, T., VUKOV, M., SAEYS, W., AND DIEHL, M. High-speed moving horizon estimation based on automatic code generation. In *Proceedings of the 51th IEEE Conference on Decision and Control (CDC 2012)* (2012). Cited on page 73.
- [40] FINKEN, T., HOMBITZER, M., AND HAMEYER, K. Study and comparison of several permanent-magnet excited rotor types regarding their applicability in electric vehicles. *Emobility - Electrical Power Train* (2010), 1–7. Cited on page 50.
- [41] FRASCH, J. qpDUNES Website. <https://github.com/jfrasch/qpDUNES/wiki>. Accessed: 20–03–2015. Cited on page 114.
- [42] FRASCH, J. V., VUKOV, M., FERREAU, H., AND DIEHL, M. A new Quadratic Programming Strategy for Efficient Sparsity Exploitation in SQP-based Nonlinear MPC and MHE. In *Proceedings of the 19th IFAC World Congress* (2013). Cited on page 114.
- [43] GEEBELEN, K. Indoors Carousel Data. [http://homes.esat.kuleuven.be/~highwind/wp-content/uploads/2014/09/indoors\\_carousel\\_data.tar.gz](http://homes.esat.kuleuven.be/~highwind/wp-content/uploads/2014/09/indoors_carousel_data.tar.gz). Accessed: 20–03–2015. Cited on page 109.

- [44] GEEBELEN, K., AHMAD, H., VUKOV, M., GROS, S., SWEVERS, J., AND DIEHL, M. An experimental test set-up for launch/recovery of an Airborne Wind Energy (AWE) system. In *Proceedings of the 2012 American Control Conference* (2012). Cited on page 76.
- [45] GEEBELEN, K., AND GILLIS, J. Modelling and control of rotational start-up phase of tethered aeroplanes for wind energy harvesting. Master's thesis, KU Leuven, June 2010. Cited on pages 15, 16, 20, 23, 25, 27, 77, and 129.
- [46] GEEBELEN, K., VUKOV, M., GROS, S., SWEVERS, J., AND DIEHL, M. Comparison of moving horizon estimators with kinematic and dynamic models based on tethered flight experiments. *IEEE Transactions on Control Systems Technology* (2015). (submitted). Cited on page 97.
- [47] GEEBELEN, K., VUKOV, M., WAGNER, A., AHMAD, H., ZANON, M., GROS, S., VANDEPITTE, D., SWEVERS, J., AND DIEHL, M. An experimental test setup for advanced estimation and control of an airborne wind energy systems. In *Airborne Wind Energy*, U. Ahrens, M. Diehl, and R. Schmehl, Eds. Springer, 2013. Cited on pages 26, 97, 98, and 124.
- [48] GEEBELEN, K., WAGNER, A., GROS, S., SWEVERS, J., AND DIEHL, M. Moving Horizon Estimation with a Huber Penalty Function for Robust Pose Estimation of Tethered Airplanes. *Proceedings of the 2012 American Control Conference* (2013). Cited on page 75.
- [49] GROS, S., AND DIEHL, M. *Airborne Wind Energy*. Springer, 2013, ch. Modeling of Airborne Wind Energy Systems in Natural Coordinates. Cited on pages 77, 100, 102, 105, and 106.
- [50] GROS, S., ZANON, M., AND DIEHL, M. Orbit Control for a Power Generating Airfoil Based on Nonlinear MPC. In *American Control Conference* (2012). (submitted). Cited on page 121.
- [51] HASELTINE, E., AND RAWLINGS, J. Critical Evaluation of Extended Kalman Filtering and Moving-Horizon Estimation. *Industrial and Engineering Chemistry Research* 44 (2005), 2451–2460. Cited on pages 67 and 73.
- [52] HAVERBEKE, N. *Efficient numerical methods for moving horizon estimation*. PhD thesis, KU Leuven, 2011. Cited on page 60.
- [53] HEWETT, R., HEATH, M., BUTALA, M., AND KAMALABADI, F. A robust null space method for linear equality constrained state estimation. *IEEE Transactions on Signal Processing* 58 (2010), 3961–3971. Cited on page 64.
- [54] HORN, G., GROS, S., AND DIEHL, M. *Airborne Wind Energy*. Springer, 2013. Cited on pages 17 and 131.

[55] HOUSKA, B., AND DIEHL, M. Optimal Control for Power Generating Kites. In *Proc. 9th European Control Conference* (Kos, Greece,, 2007), pp. 3560–3567. (CD-ROM). Cited on page 121.

[56] HOUSKA, B., FERREAU, H., AND DIEHL, M. ACADO Toolkit – An Open Source Framework for Automatic Control and Dynamic Optimization. *Optimal Control Applications and Methods* 32, 3 (2011), 298–312. Cited on page 114.

[57] HOUSKA, B., FERREAU, H., AND DIEHL, M. An Auto-Generated Real-Time Iteration Algorithm for Nonlinear MPC in the Microsecond Range. *Automatica* 47, 10 (2011), 2279–2285. Cited on pages 72 and 73.

[58] ILZHOEFER, A., HOUSKA, B., AND DIEHL, M. Nonlinear MPC of kites under varying wind conditions for a new class of large scale wind power generators. *International Journal of Robust and Nonlinear Control* 17, 17 (2007), 1590–1599. Cited on pages 5 and 121.

[59] INTERNATIONAL ENERGY AGENCY. Norway: Electricity and Heat for 2012. <http://www.iea.org/statistics/statisticssearch/report/?country=NORWAY&product=electricityandheat&year=2012>. Accessed: 20–03–2015. Cited on page 2.

[60] JACOBSON, M., AND ARCHER, C. Saturation wind power potential and its implications for wind energy. *Proceedings of the National Academy of Sciences* 109, 39 (2012), 15679–15684. Cited on page 3.

[61] JULIER, S., UHLMANN, J., AND DURRANT-WHYTE, H. A new method for the nonlinear transformation of means and covariances in filters and estimators. *IEEE Transactions on Automatic Control* 45 (2000), 477–482. Cited on page 97.

[62] KALMAN, R. A New Approach to Linear Filtering and Prediction Problems. *Transactions of the ASME-Journal of Basic Engineering* 82 (1960), 35–45. Cited on page 62.

[63] KERKHOFS, B. Ontwerp van een vlieger voor energieopwekking met behulp van verankerde kites. Master's thesis, KU Leuven, 2013. Cited on page 49.

[64] KITEGEN. Kite Gen Stem website. <http://www.kitegen.com/en/>. Accessed: 20–03–2015. Cited on pages 9, 12, and 13.

[65] KOLAR, J. W., FRIEDLI, T., KRISMER, F., LOOSER, A., SCHWEIZER, M., STEIMER, P., AND BEVIRT, J. Conceptualization and multi-objective optimization of the electric system of an airborne wind turbine. *Proceeding of the 20th IEEE International Symposium on Industrial Electronics (ISIE 2011)* (2011), 32–55. Cited on page 14.

- [66] KRAUS, T. Real-Time State And Parameter Estimation for NMPC-Based Feedback Control With Application To The Tennessee Eastman Benchmark Process. Master's thesis, University of Heidelberg, 2007. Cited on page 83.
- [67] KÜHL, P., DIEHL, M., KRAUS, T., SCHLÖDER, J. P., AND BOCK, H. G. A real-time algorithm for moving horizon state and parameter estimation. *Computers & Chemical Engineering* 35, 1 (2011), 71–83. Cited on page 118.
- [68] LEFEBVRE, T., BRUYNINCKX, H., AND DE SCHUTTER, J. Kalman filters for non-linear systems: a comparison of performance. *International Journal of Control* 77, 7 (2004), 639–653. Cited on page 62.
- [69] LEFFERTS, E., MARKLEY, F., AND SHUSTER, M. Kalman filtering for spacecraft attitude estimation. *Journal of Guidance, Control, and Dynamics* 5, 5 (1982), 417–429. Cited on pages 76 and 78.
- [70] LOYD, M. Crosswind Kite Power. *Journal of Energy* 4, 3 (July 1980), 106–111. Cited on pages 4 and 5.
- [71] MAKANI POWER. Makani Power Website. <http://www.google.com/makani/>. Accessed: 20–03–2015. Cited on pages 10 and 131.
- [72] MAYNE, D., AND RAWLINGS, J. *Model Predictive Control*. Nob Hill, 2013. Cited on page 61.
- [73] MHI VESTAS. Offshore wind. <http://www.mhivestasoffshore.com/Products-and-services/The-Turbines/V164>. Accessed: 20–03–2015. Cited on page 6.
- [74] OLINGER, D., GOELA, J., AND TRYGGVASON, G. Modeling and Testing of a Kite-Powered Water Pump. In *Airborne Wind Energy*, U. Ahrens, M. Diehl, and R. Schmehl, Eds. Springer, 2013. Cited on page 11.
- [75] OPEC. Organization of the Petroleum Exporting Countries. <http://www.opec.org>. Accessed: 20–03–2015. Cited on page 2.
- [76] PAMADI. *Performance, Stability, Dynamics, and Control of Airplanes*. American Institute of Aeronautics and Astronautics, Inc., 2003. Cited on page 26.
- [77] PENEDO, R., PARDAL, T., SILVA, P., FERNANDES, N., AND FERNANDES, T. High Altitude Wind Energy from a Hybrid Lighter-than-Air Platform Using the Magnus Effect. In *Airborne Wind Energy*, U. Ahrens, M. Diehl, and R. Schmehl, Eds. Springer, 2013. Cited on page 11.
- [78] QUIRYNEN, R. Automatic code generation of Implicit Runge-Kutta integrators with continuous output for fast embedded optimization. Master's thesis, KU Leuven, 2012. Cited on page 131.

[79] QUIRYNEN, R., GROS, S., AND DIEHL, M. Fast auto generated ACADO integrators and application to MHE with multi-rate measurements. In *Proceedings of the European Control Conference* (2013). Cited on pages 96 and 131.

[80] RAWLINGS, J., AND BAKSHI, B. Particle filtering and moving horizon estimation. *Computers and Chemical Engineering* 30 (2006), 1529–1541. Cited on page 76.

[81] RENEWABLE ENERGY WORLD. Meet The New World's Biggest Wind Turbine. <http://www.renewableenergyworld.com/rea/news/article/2014/02/meet-the-new-worlds-biggest-wind-turbine>. Accessed: 20–03–2015. Cited on page 3.

[82] RUITERKAMP, R., AND SIEBERLING, S. Description and Preliminary Test Results of a Six Degrees of Freedom Rigid Wing Pumping System. In *Airborne Wind Energy*, U. Ahrens, M. Diehl, and R. Schmehl, Eds. Springer, 2013. Cited on page 10.

[83] SCHMEHL, R., VAN DER VLUGT, R., FECHNER, U., DE WACHTER, A., AND OCKELS:, W. Airborne Wind Energy System, 2014. Cited on page 13.

[84] SIEMENS AG. *Catalog D31: SINAMICS and Motors for Single-Axis Drives*, 2012. Cited on page 49.

[85] SIMLEY, E., PAO, L., KELLEY, N., JONKMAN, B., AND FREHLICH, R. LIDAR wind speed measurements of evolving wind fields. In *Proceedings AIAA Aerospace Sciences Meeting* (2012). Cited on page 131.

[86] SKYSAILS. Skysails Marine Website. <http://www.skysails.info/english/skysails-marine/skysails-propulsion-for-cargo-ships/>. Accessed: 20–03–2015. Cited on pages 9 and 12.

[87] SKYSAILS. Skysails Power Website. <http://www.skysails.info/english/power/>. Accessed: 20–03–2015. Cited on page 9.

[88] STUYTS, J., AND VANDERMEULEN, W. Electrical Energy Conversion System for Pumping Airborne Wind Energy. Master's thesis, KU Leuven, 2013. Cited on pages 20, 33, 49, and 129.

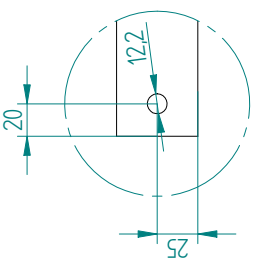
[89] TEULIÈRE, C., ECK, L., MARCHAND, E., AND GUÉNARD, N. 3d model-based tracking for UAV position control. In *The 2010 IEEE/RSJ International Conference on Intelligent Robots and Systems (IROS)* (October 2010), IEEE, pp. 1084–1089. Cited on page 97.

- [90] THE WORLD BANK. Fossil fuel energy consumption. <http://data.worldbank.org/indicator/EG.USE.COMM.FO.ZS>. Accessed: 20-03-2015. Cited on page 1.
- [91] TU DELFT. KitePower. <http://www.kitepower.eu>. Accessed: 20-03-2015. Cited on page 9.
- [92] VANDER LIND, D. Analysis and Flight Test Validation of High Performance Airborne Wind Turbines. In *Airborne Wind Energy*, U. Ahrens, M. Diehl, and R. Schmehl, Eds. Springer, 2013. Cited on pages 6, 10, and 14.
- [93] VERMILLION, C., GLASS, B., AND REIN, A. Lighter-Than-Air Wind Energy Systems. In *Airborne Wind Energy*, U. Ahrens, M. Diehl, and R. Schmehl, Eds. Springer, 2013. Cited on pages 11 and 13.
- [94] VUKOV, M., DOMAHIDI, A., FERREAU, H. J., MORARI, M., AND DIEHL, M. Auto-generated Algorithms for Nonlinear Model Predictive Control on Long and on Short Horizons. In *Proceedings of the 52nd Conference on Decision and Control (CDC)* (2013). Cited on pages 72, 73, and 114.
- [95] WAKATSUKI, Y. New radioactive water leak at Japan's Fukushima Daiichi plant. <http://edition.cnn.com/2014/02/19/world/asia/japan-fukushima-daiichi-water-leak/>. Accessed: 20-03-2015. Cited on page 2.
- [96] WAN, E., AND VAN DER MERWE, R. The unscented Kalman filter for nonlinear estimation. In *Adaptive Systems for Signal Processing, Communications, and Control Symposium 2000. AS-SPCC. The IEEE 2000* (2000), IEEE, pp. 153–158. Cited on pages 67, 68, and 69.
- [97] WHITE, N., TIERNO, N., AND GARCIA-SANZ, M. A novel approach to airborne wind energy: Design and modeling. In *Energytech, IEEE* (2011). Cited on pages 13 and 14.
- [98] X-MODELS. Stingray heavy slope version. [http://www.xmodelshop.com/stingray-heavy-slope-version-c-68\\_88.html](http://www.xmodelshop.com/stingray-heavy-slope-version-c-68_88.html). Accessed: 20-03-2015. Cited on page 49.
- [99] ZANON, M., GROS, S., ANDERSSON, J., AND DIEHL, M. Airborne Wind Energy Based on Dual Airfoils. *IEEE Transactions on Control Systems Technology* 21 (July 2013). Cited on pages 6 and 7.

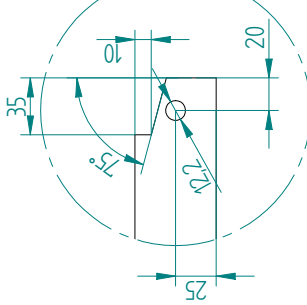


## **Appendix A**

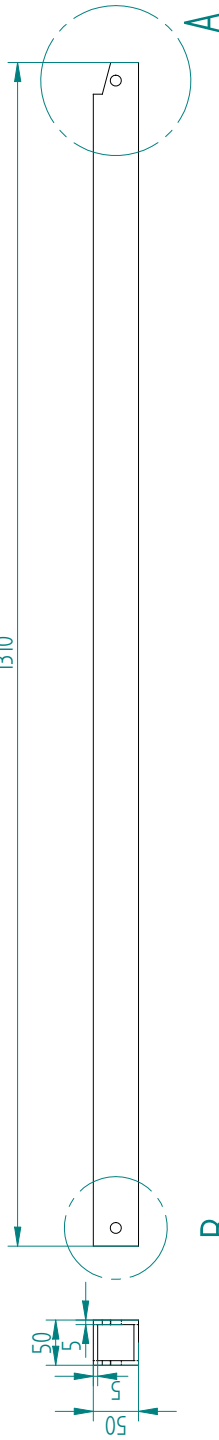
### **Technical drawings of outdoors carousel**



DETAIL B



DETAIL A



B

Allgemeine Richtlijn	Allgemeine Tolerantie	Materiaal	Aluminium profiel 50x50x5	1	Tekening Nr.	
Schaal	Projectie	Behandeling			Dossier Nr.	Aantal
1:6					Highwind	4

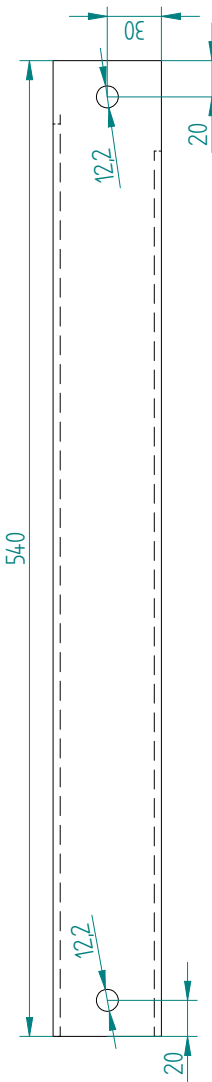
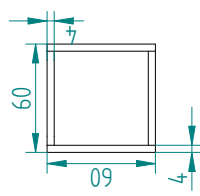
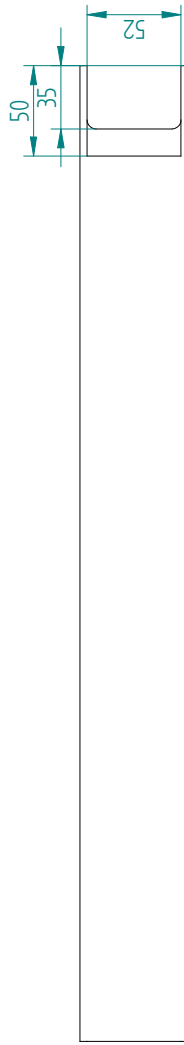
Staaf A

**KU LEUVEN**

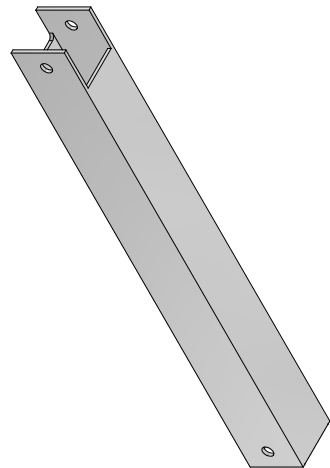
Auteur:

Datum:

A4



Algemene Rechtd	Algemene Tolerantie	Materiaal	Aluminium profiel 60x60x4	Tekening Nr.	2
Schaal	Projectie	Behandeling		Dossier Nr.	Aantal
1:3				Highwind caroussel	4



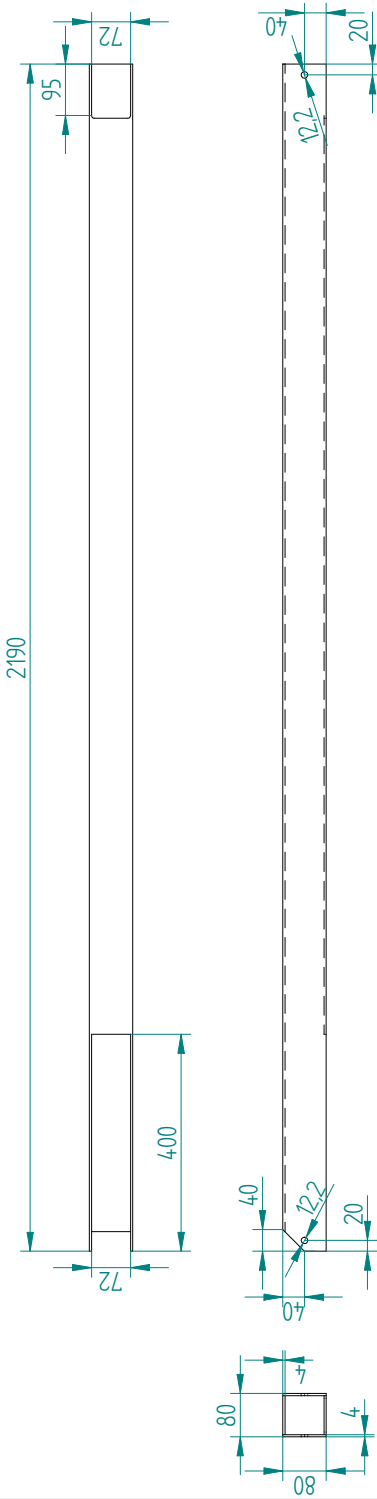
Staaf B

**KU LEUVEN**

Auteur:

Datum:

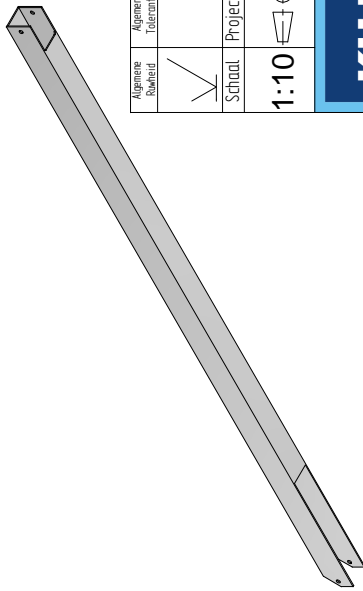
A4



Algemene Rechtd	Algemene Tolerantie	Materiaal	Aluminium profiel 80x80x4	Tekening Nr.
✓				3
Schaal	Projectie	Behandeling		Dossier Nr.

1:10 Aantal

Highwind  
carousel 4



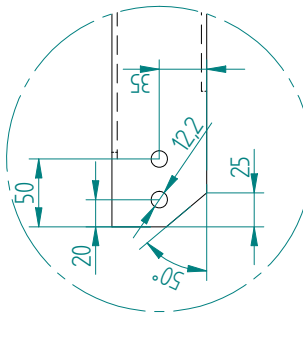
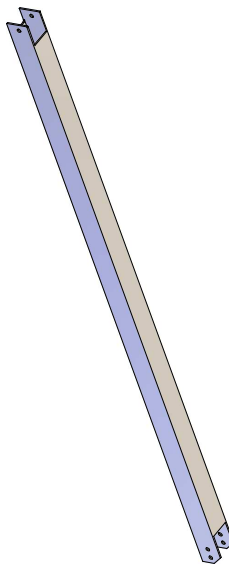
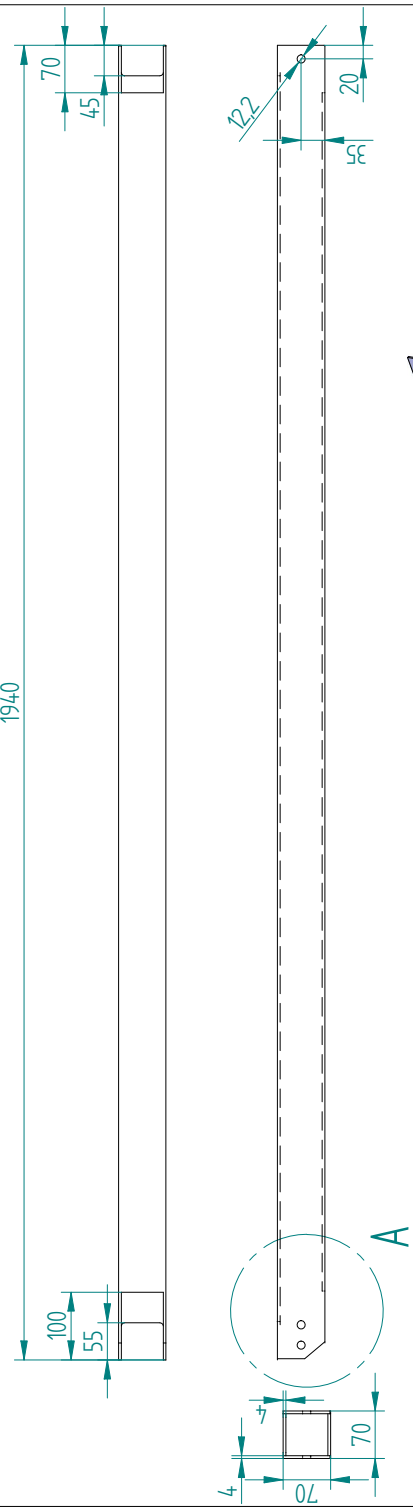
Staaf C

**KU LEUVEN**

Auteur:

Datum:

A4



DETAIL A

Allgemeine Rechtd	Allgemeine Tolerantie	Materiaal	Aluminium profiel 70x70x4
Schaal	Projectie	Behandeling	

1.8	1.8	4	4
Schaal	Projectie	Behandeling	

Doosier Nr.  
Highwind  
carouzel

Tekening Nr.  
4

Aantal  
4

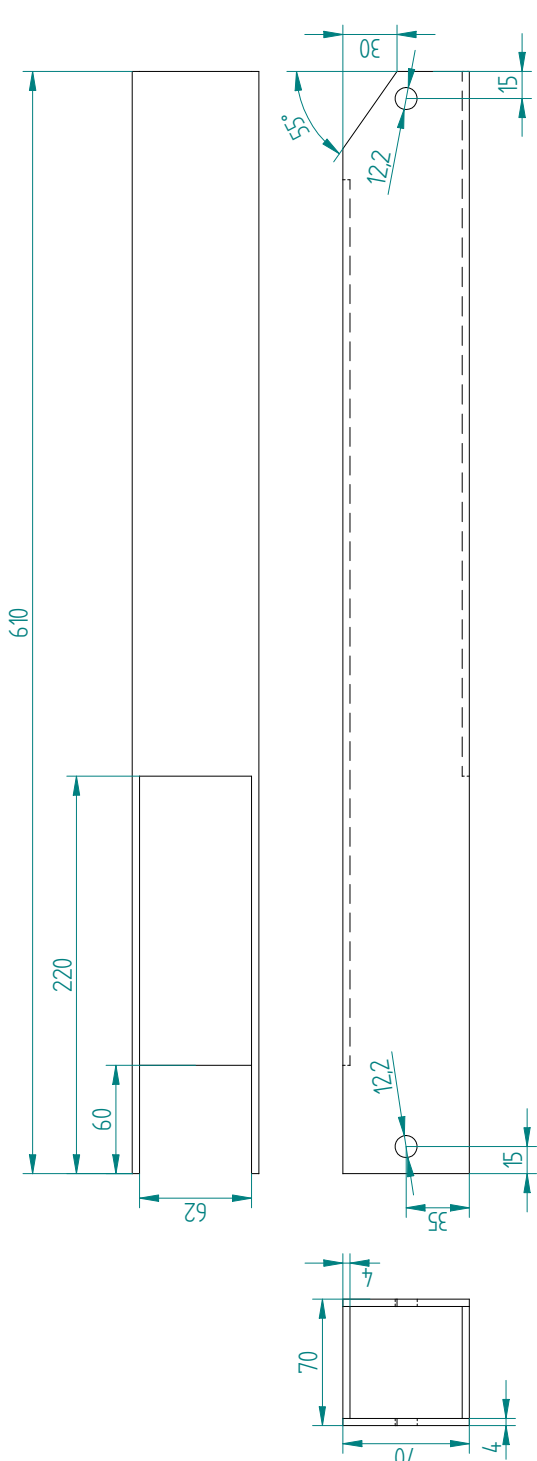
Staaf D

**KU LEUVEN**

Auteur:

Datum:

A4



Allgemeine Richtheid	Allgemeine Tolerantie	Materiaal	Tekening Nr.
✓		Aluminium profiel 70x70x4	5

Schaal	Projectie	Behandeling	
1:2			

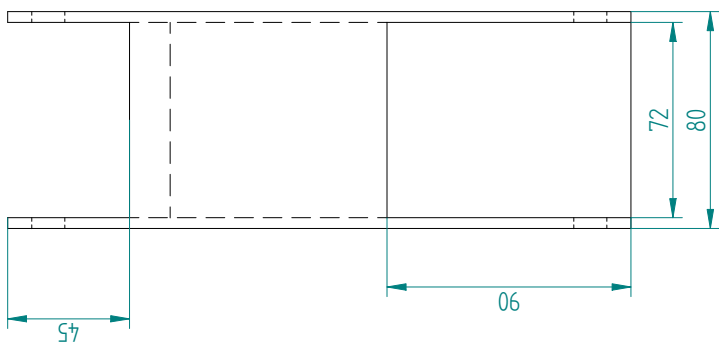
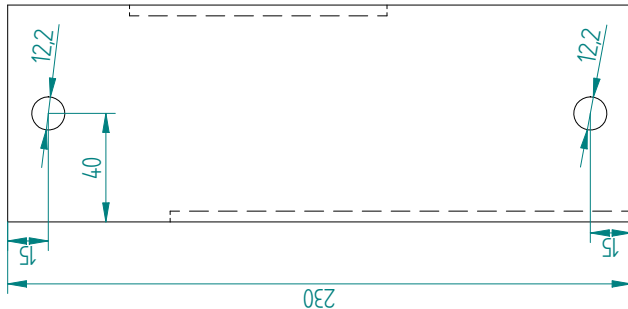
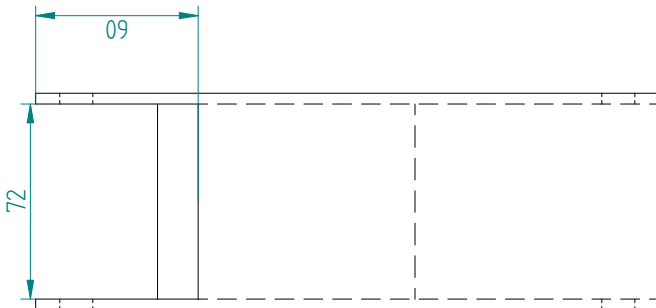
Dossier Nr. **Highwind**  
Aantal **4**  
caroussel

**KU LEUVEN**

Auteur:

Datum:

A4



Aluminium profiel 80x80x4		Tekening Nr. 6	
Algemene Rechtd.	Algemene Tolerantie	Material	
✓		Behandeling	

Dossier Nr.	Highwind
Aantal	4

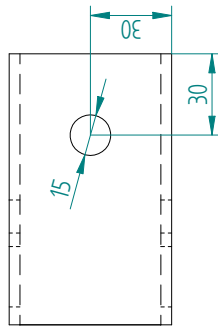
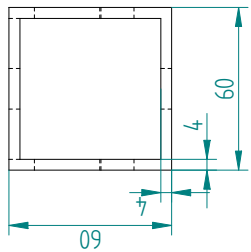
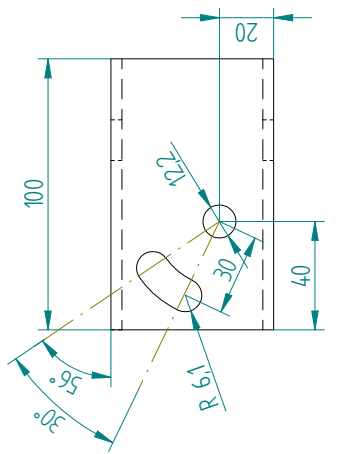
Staaf F

**KU LEUVEN**

Auteur:

Datum:

A4



Allgemeine Richtheid	Allgemeine Tolerantie	Materiaal	Aluminium profiel 60x60x4	Tekening Nr.	7
Schaal	Projectie	Behandeling		Dossier Nr.	Aantal

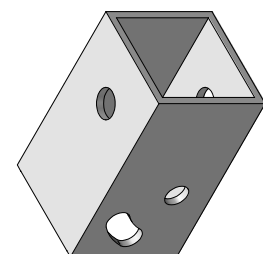
1:2			Highwind caroussel	Highwind caroussel	4
-----	--	--	-----------------------	-----------------------	---

**KU LEUVEN**

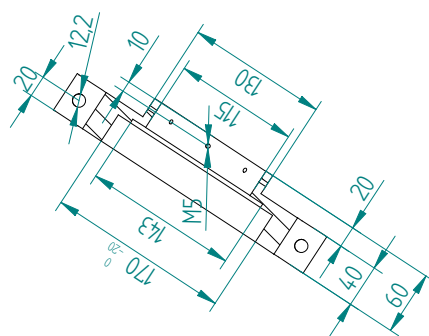
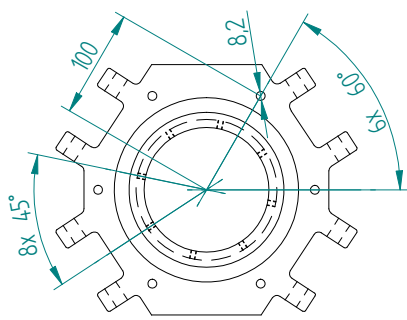
Auteur:

Datum:

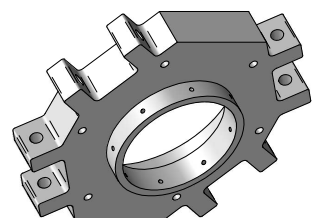
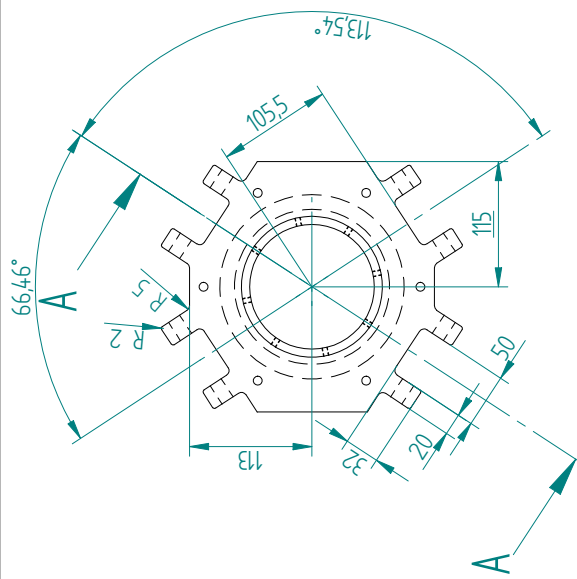
A4







SECTION A-A



Allgemeine Richtlijn	Allgemeine Tolerantie	Materiaal	Aluminium	Tekening Nr.	9
Schaal	Projectie	Behandeling		Dossier Nr.	Highwind
1:5				Aantal	1

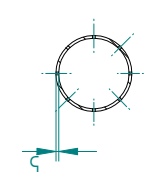
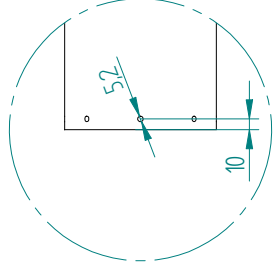
**KU LEUVEN**

Auteur:

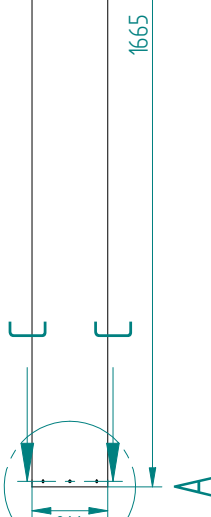
Datum:

A4

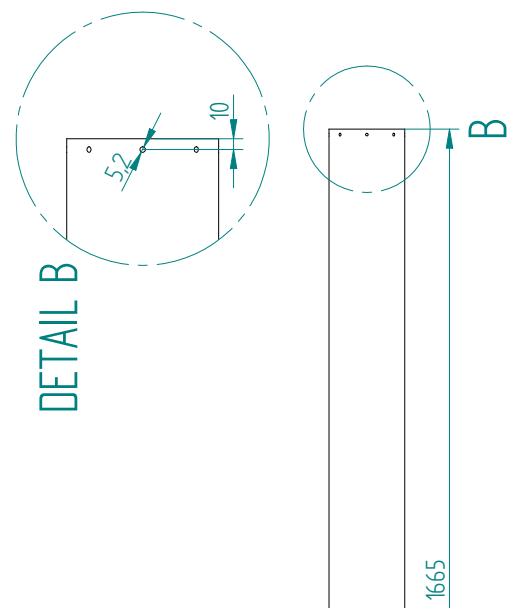
## DETAIL A



## SECTION C-C



## DETAIL B



Allgemeine Richtlijn	Allgemeine Tolerantie	Materiaal	Aluminium buis 140x5	Tekening Nr.	10
Schaal	Projectie	Behandeling		Dossier Nr.	
1:10		$\odot$		Highwind caroussel	1

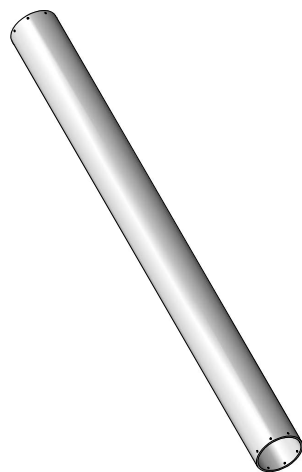
Omhulsel as

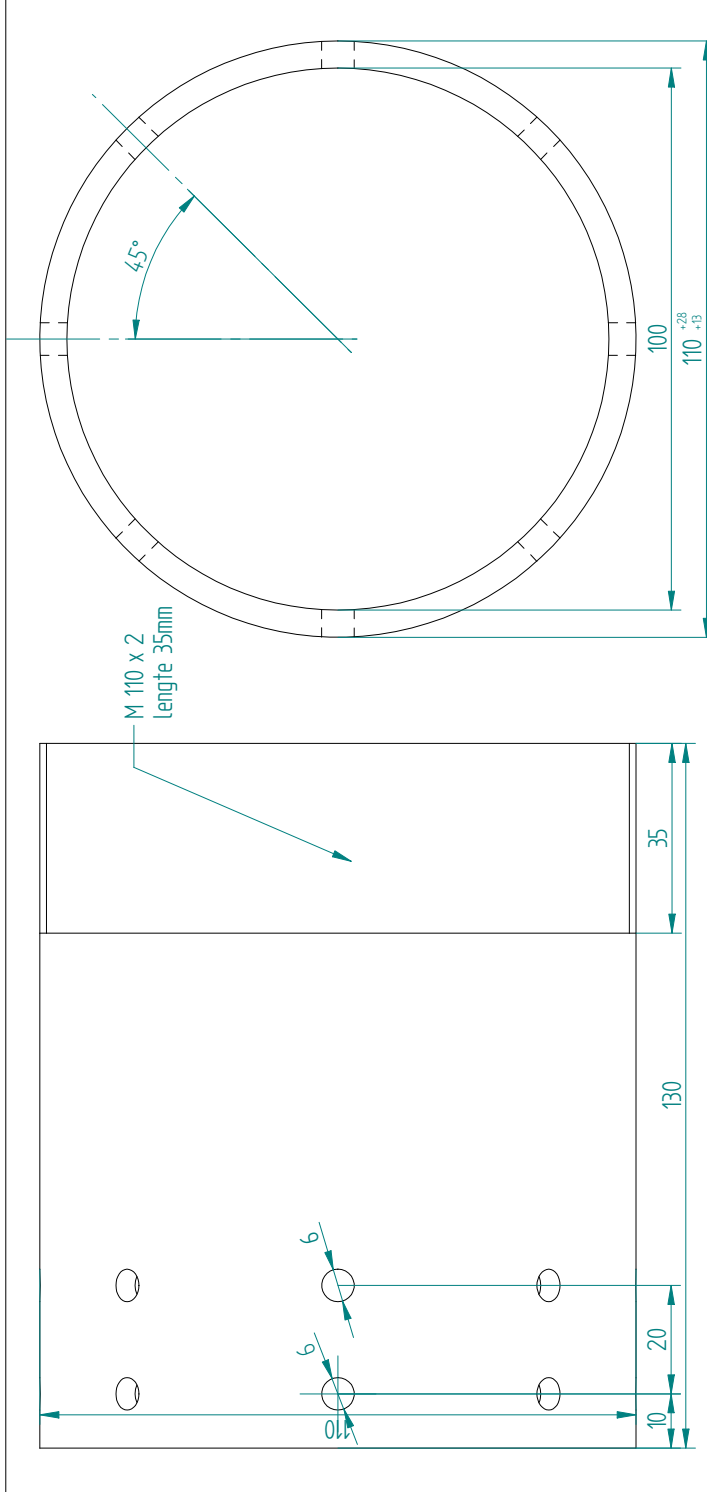
**KU LEUVEN**

Auteur:

Datum:

A4





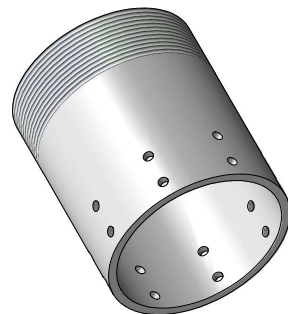
## Aluminium

11

Dossier Nr.	Aantal
Highwind carousel	1

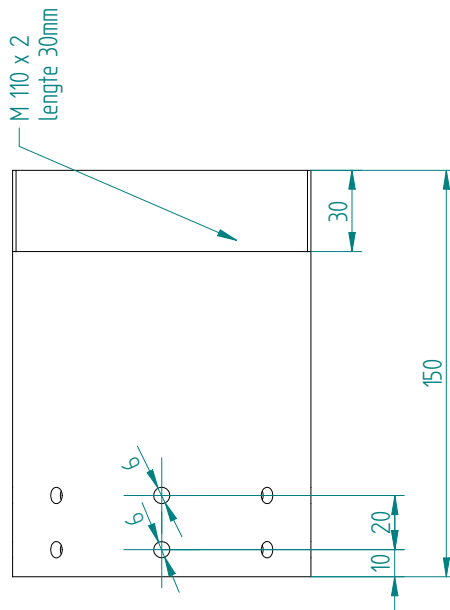
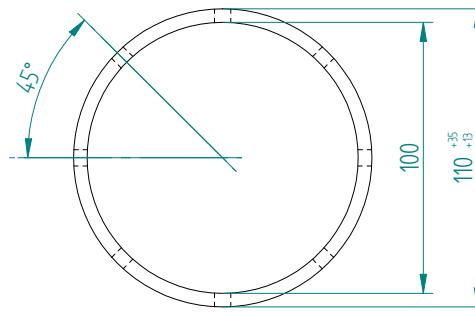
## Lagerbus onderaan

KU LEUVEN



Algemene Ruimte	Algemene Tolerantie	Material	Aluminium	Tekening Nr.
✓				11

Dossier Nr.	Aantal
Highwind carousel	1



Allgemeine Richtheid	Allgemeine Tolerantie	Materiaal	Tekening Nr.
✓		Aluminium	12
Schaal	Projectie	Behandeling	Dossier Nr.
1:2	Φ		Aantal



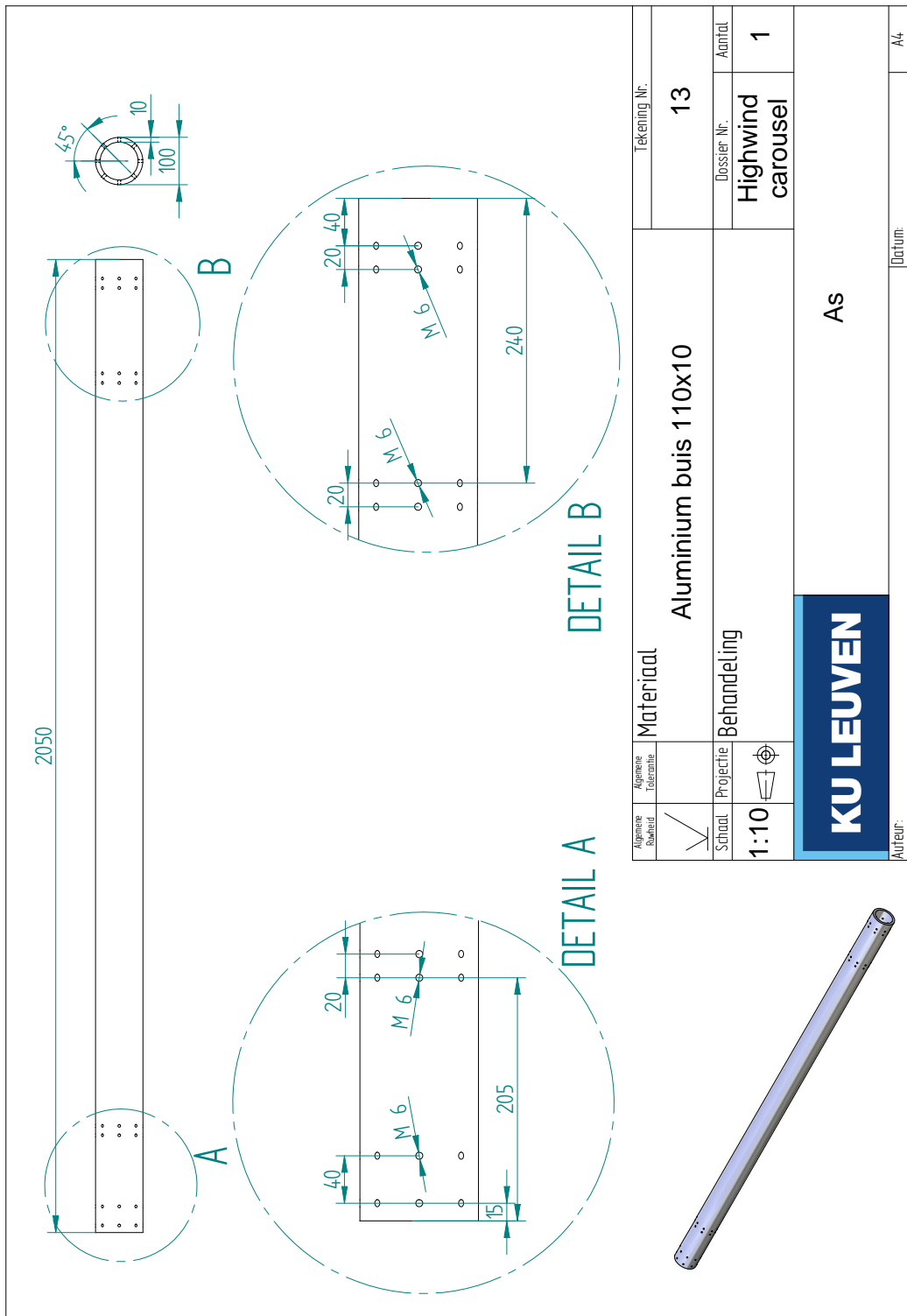
Lagerbous bovenaan

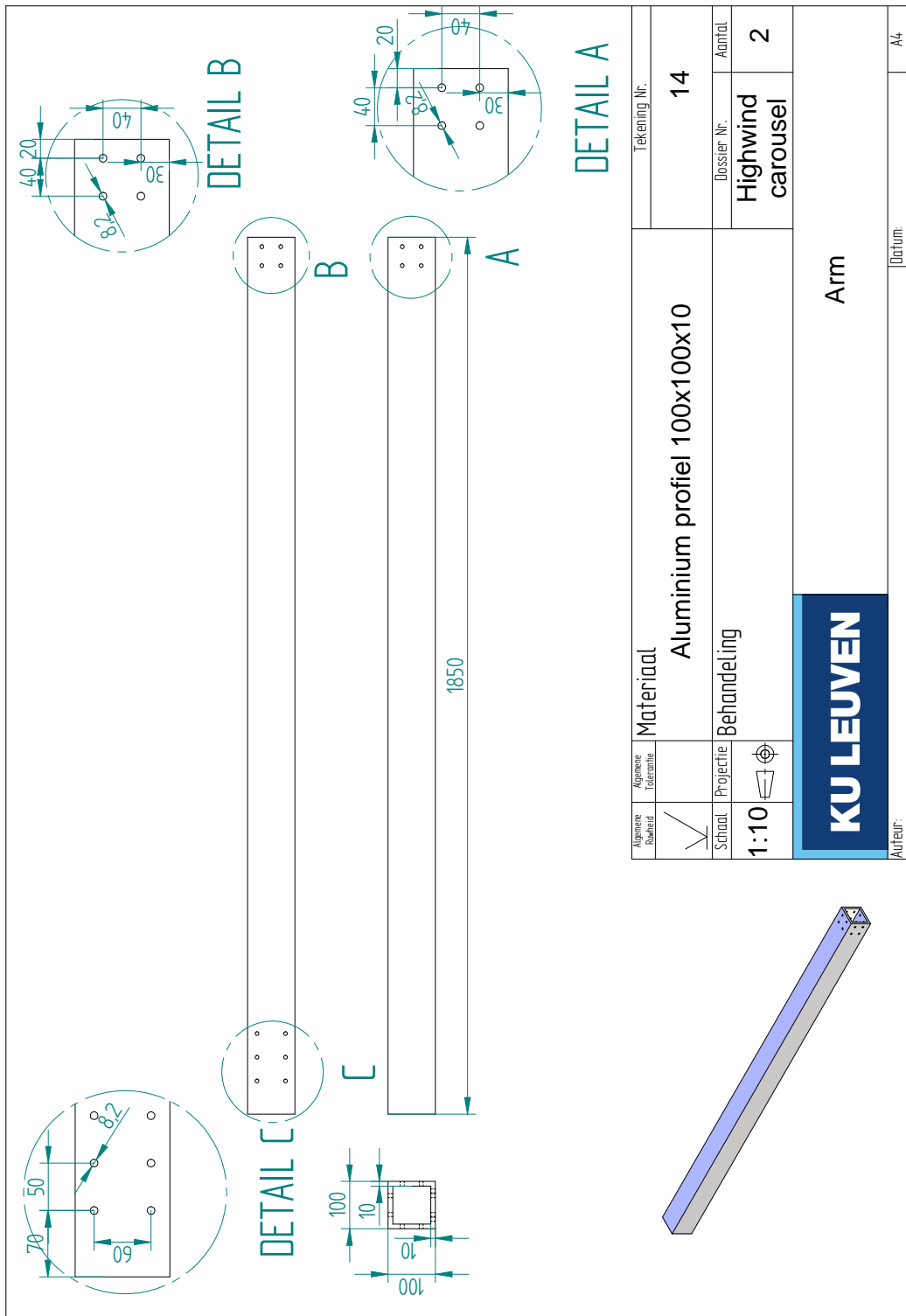
**KU LEUVEN**

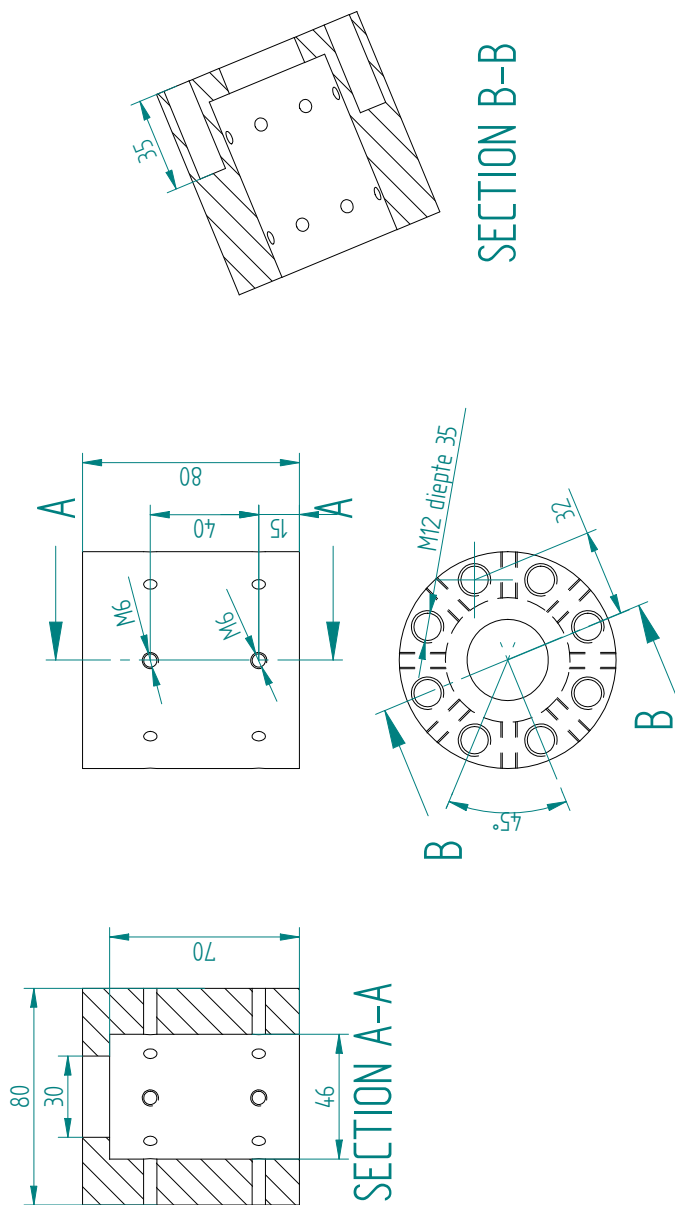
Auteur:

Datum:

A4



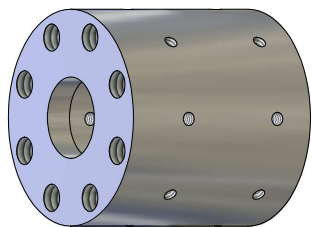


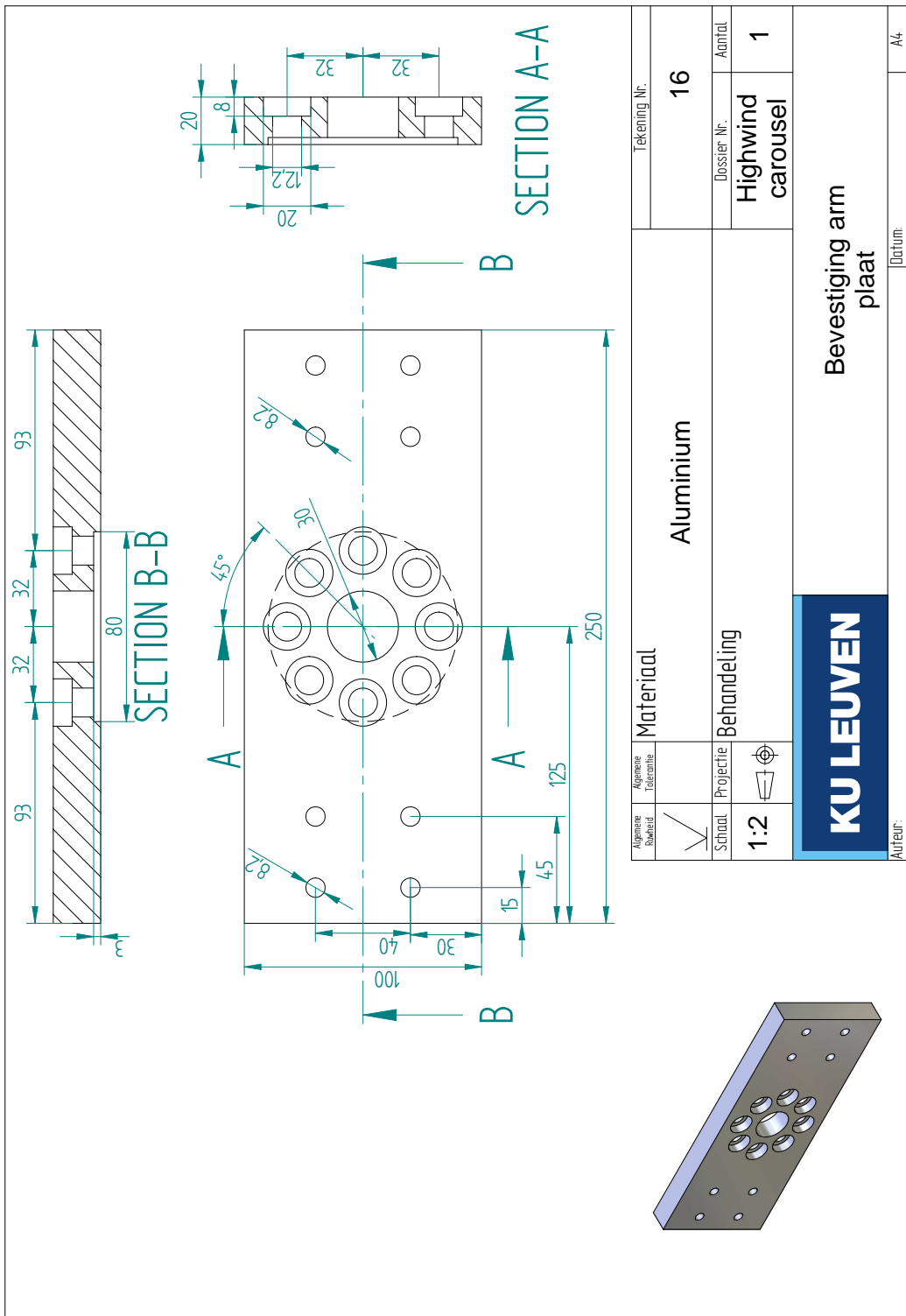


Allgemeine Richtlijn	Allgemeine Tolerantie	Tekening Nr.	
✓		15	
Schaal	Projectie	Behandeling	
1:2			

**KU LEUVEN**

Autteur: Datum:  

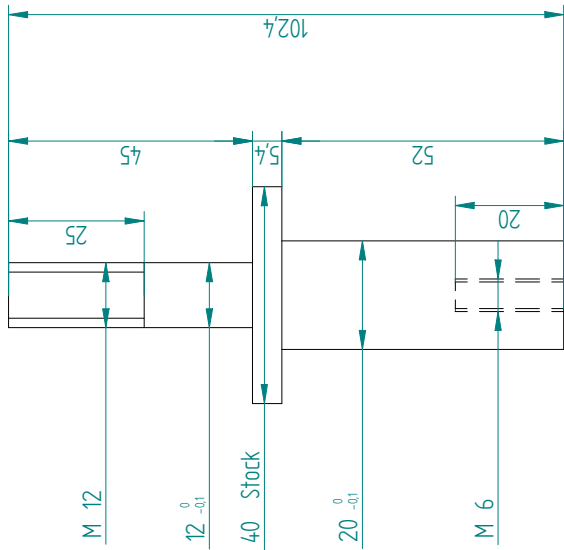
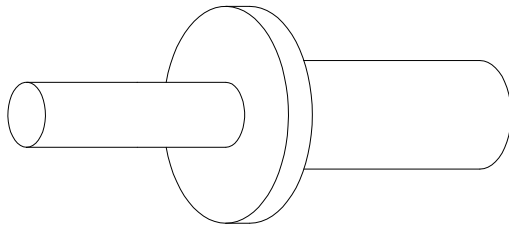






## **Appendix B**

### **Technical drawings of outdoors winch**



Allgemeine Richtlijn	Allgemeine Tolerantie	Materiaal	Tekening Nr.
✓	M	Aluminium	
Schaal	Projectie	Behandeling	Dossier Nr.
1:1			Aantal 1

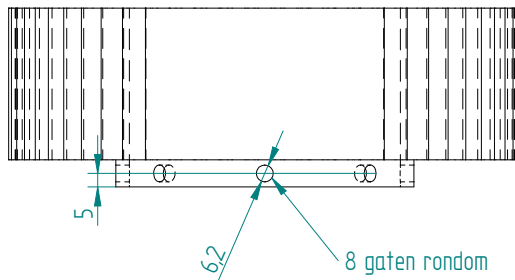
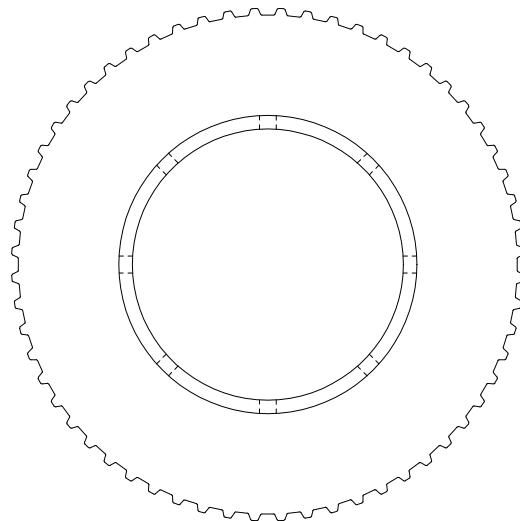
## Carousel drive aanspanner

**KU LEUVEN**

Auteur: Kurt Geethelen

Datum: 01/03/2013

A4



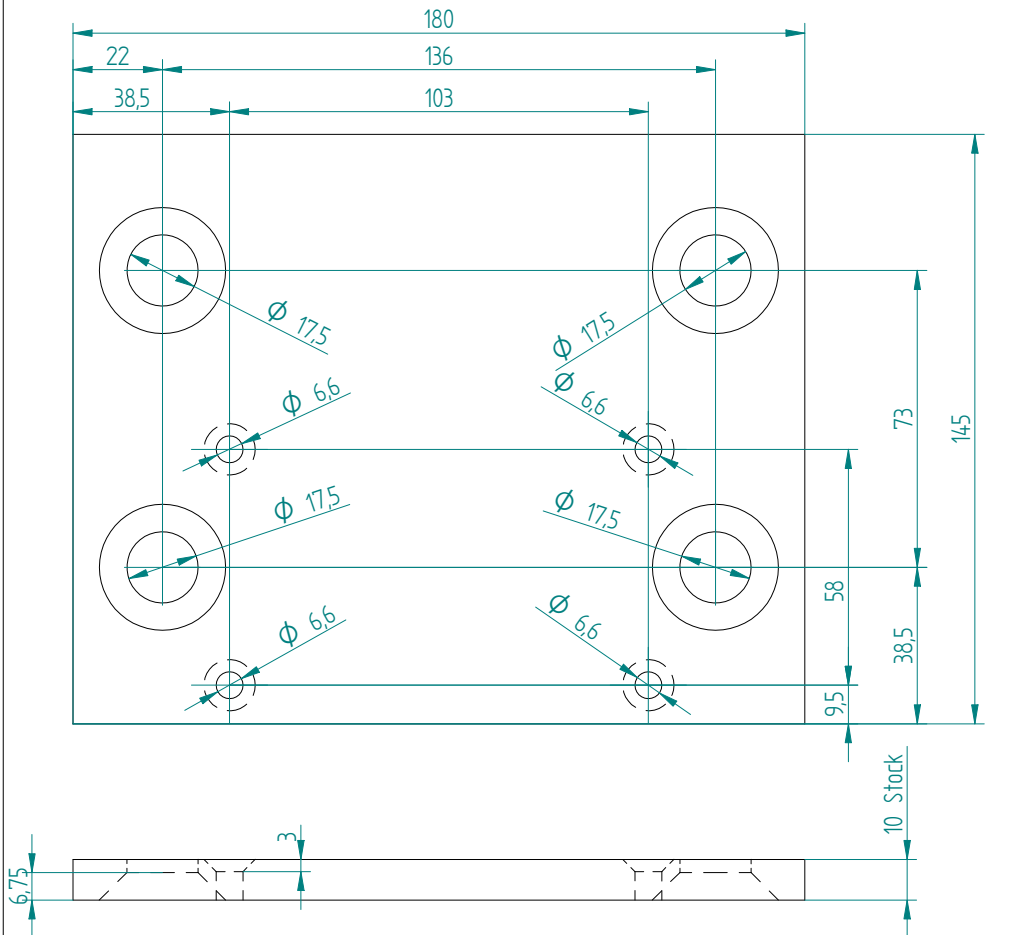
Algemene Ruwhed	Algemene Tolerantie	Materiaal aluminium	Tekening Nr.	
<input checked="" type="checkbox"/>	m			
Schaal	Projectie	Behandeling	Dossier Nr.	Aantal
2:5				1

**KU LEUVEN**

Carousel riemschijf

- a) Identieke gaten voor DIN 7991 bout M16. De bouten worden verzonken
- b) Identieke gaten voor DIN 7991 bout M6. De bouten worden verzonken.

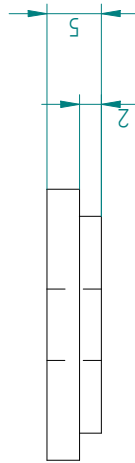
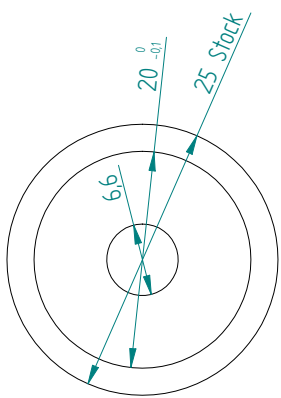
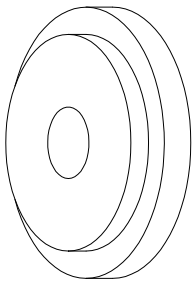
Merk op dat de M16 bouten aan de andere kant dan de M6 bouten verzonken worden.



Algemene Ruwheid	Algemene Tolerantie	Materiaal  Aluminium	Tekening Nr.	
	m			
Schaal	Projectie	Behandeling	Dossier Nr.	Aantal
3:4				1

KU LEUVEN

## Plaat wagen



Allgemeine Rohmaterial	Agemene Tolerantie	Materiaal	Aluminium of messing	Tekening Nr.
✓	m	Behandeling		Dossier Nr.
Schaal 2:1	Projectie 			Aantal 2

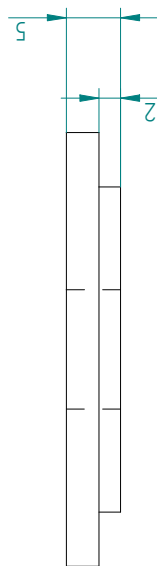
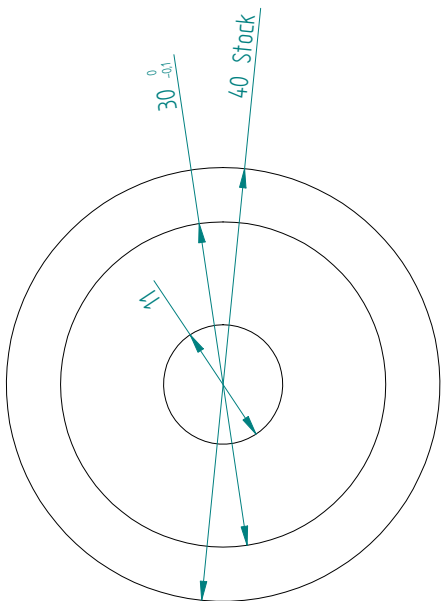
## Drive aanspannerdop

**KU LEUVEN**

Auteur: Kurt Geethelen

Datum: 01/03/2013

A4



Algemene Richtlijn		Algemene Tolerancie	Materiaal	Aluminium of messing	Tekening Nr.
✓	m				
Schaal	Projectie	Behandeling			Dossier Nr. Aantal
2:1	Ø				1

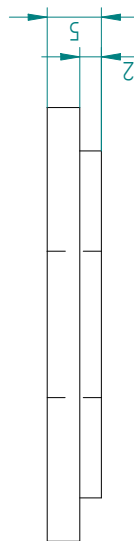
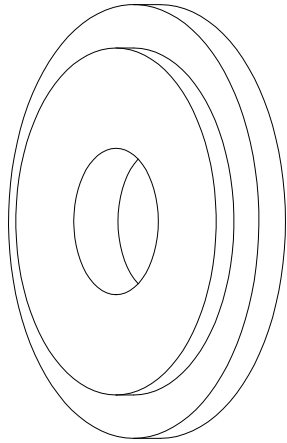
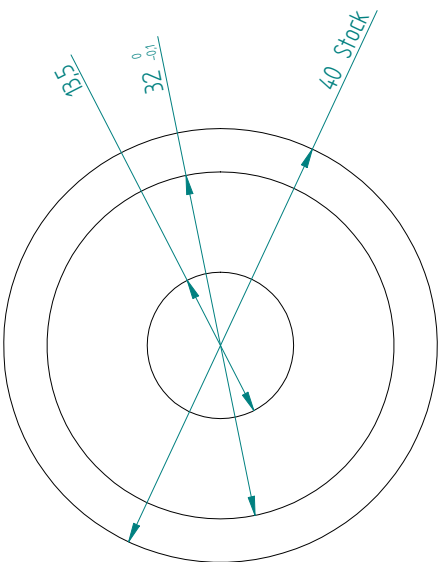
**KU LEUVEN**

Auteur: Kurt Geethelen

Datum: 01/03/2013

A4

Drive motordop



Allgemeine Rohrteil	Material	Aluminium of messing	
Schaal	Projectie	Behandeling	Tekening Nr.
2:1			Dossier Nr. 1 Aantal 1

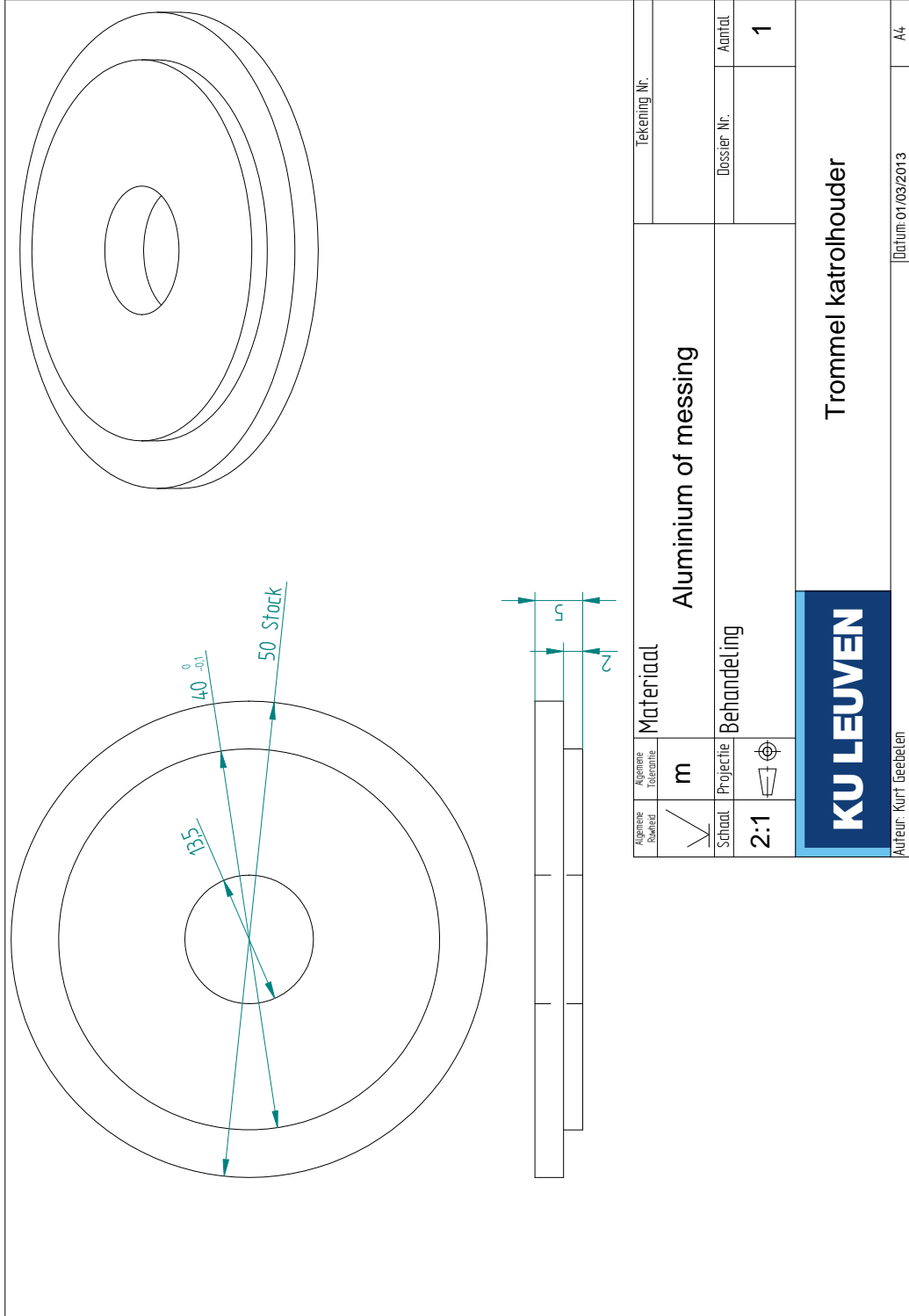
## Drive riemschijfhouder

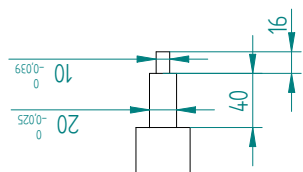
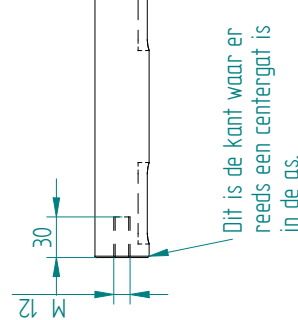
**KU LEUVEN**

Auteur: Kurt Geleijnen

Datum: 01/03/2013

A4





Allgemeine Richtlijn	Allgemeine Tolerancie	Materiaal	Tekening Nr.
✓	m	Steel	
Schaal	Projectie	Behandeling	Dossier Nr.
1:4			Aantal 1

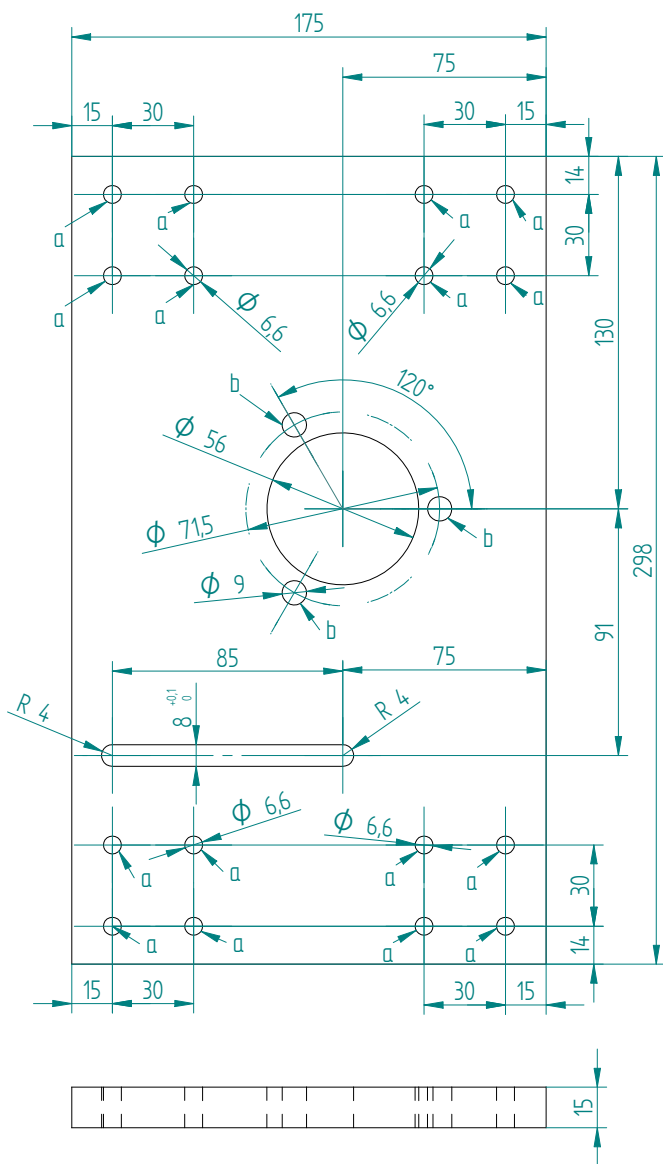
Trommelaas

**KU LEUVEN**

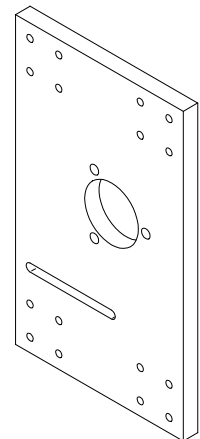
Auteur: Kurt Geethelen

Datum: 01/03/2013

A4



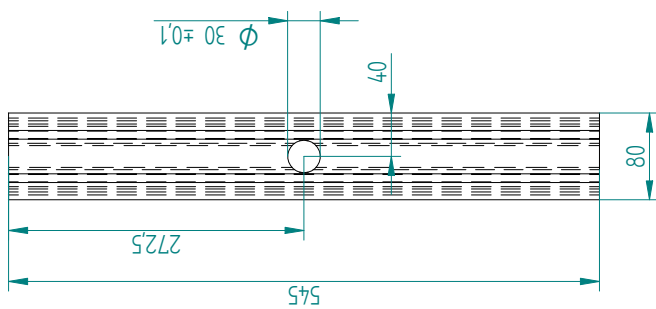
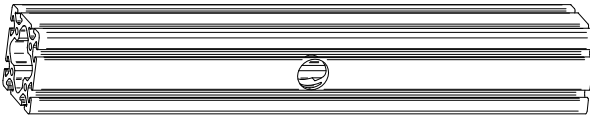
- a) Identieke doorlopende gaten voor DIN912 bout M6
- b) Identieke doorlopende gaten voor DIN912 bout M8



Algemene Ruwheid	Algemene Tolerantie	Materiaal  Alcoa aluminium	Tekening Nr.	
	m			
Schaal	Projectie	Behandeling	Dossier Nr.	Aantal
1:2				1

KU LEUVEN

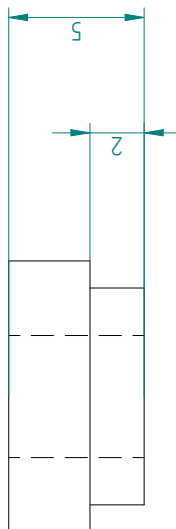
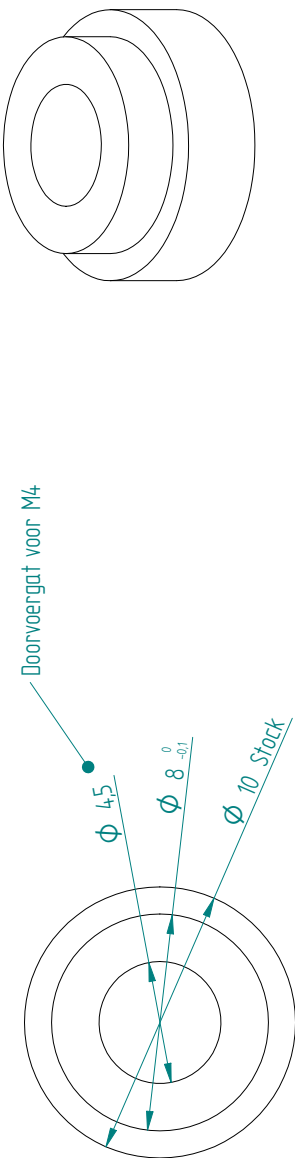
## Trommelplaat



✓	Algemeene Tolerantie	Materiaal	Aluminium	Tekening Nr.
Schaal	Projectie	Behandeling		Dossier Nr.
1:2	Ø			Aantal 1

## Item profiel 80x80

**KU LEUVEN**



Algemene Richtlijn	Algemene Tolerantie	Materiaal	Aluminium of messing	Tekening Nr.
✓	m	Behandeling		Dossier Nr.
Schaal	Projectie			Aantal
5:1				1

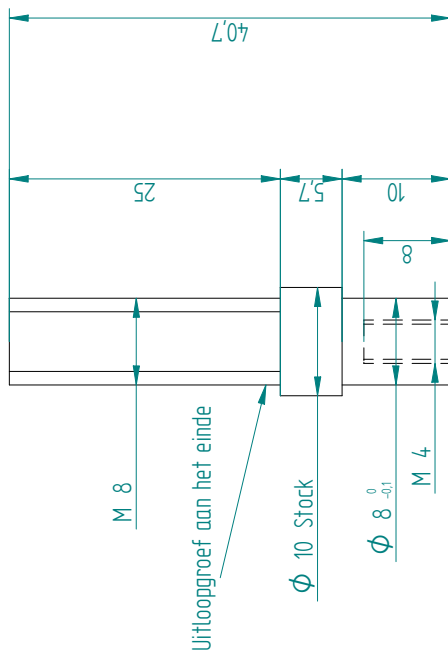
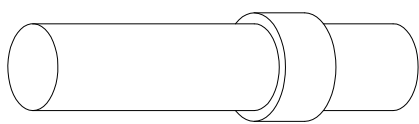
Dop lineaire geleider

**KU LEUVEN**

Auteur: Kurt Geleelien

Datum: 06/03/2013

A4



Allgemeine Röhrfeld	Allgemeine Toleranzie	Materiaal	Tekening Nr.
✓	M	Aluminium	
Schaal	Projectie	Behandeling	Dossier Nr.
2:1	Φ		Aantal 1

## Aanspanner lineaire geleider

**KU LEUVEN**

Auteur: Kurt Gelehrten

Datum: 06/03/2013

A4

De buitenste contour is symmetrisch (de 2 uitgesneden driehoeken hebben dezelfde afmetingen).

- a) Identieke doorlopende gaten voor DIN7991 bout M10. De bouten worden verzonken.

b) Identieke doorlopende gaten voor DIN912 bout M8

Technical drawing of a mechanical part with various dimensions and features. The drawing includes a main view and a cross-sectional view labeled "SECTION A-A". Key dimensions include overall height of 460, overall width of 225, and various internal features like holes, slots, and radii. The cross-sectional view shows a thickness of 20 and a height of 126.

## SECTION A-A

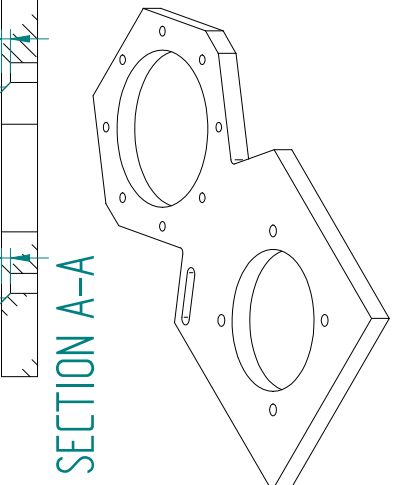
Alcoa aluminum

Beijing

1

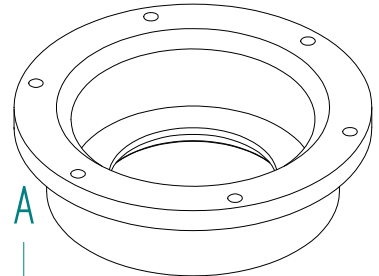
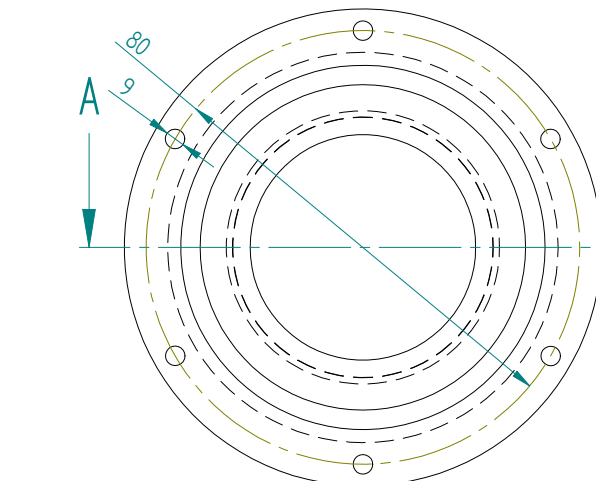
Motorhouder

KU LEUVEN

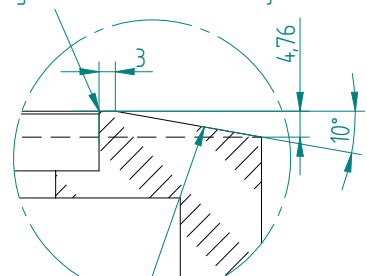


Algemene RawMeld	Algemene Tolerantie	Material	Tekening Nr.	
✓	m	Alcoa aluminium		
Schaal	Projectie	Behandeling		Dossier Nr.
1:3				Aantal

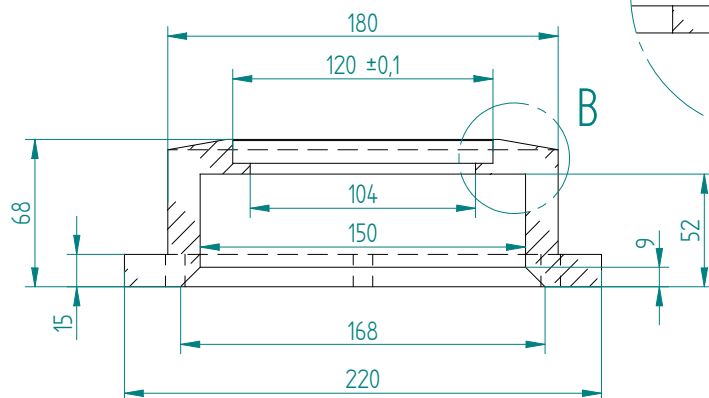
Auteur: Kurt Gebelein



Afschuining met een diepte van 0.5 mm en een hoek van 10 tot 15 graden met een verticale lijn



DETAIL B



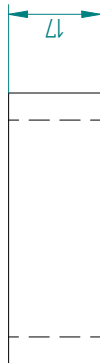
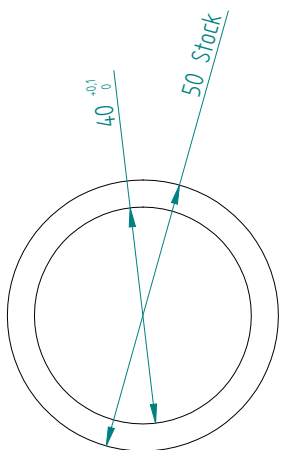
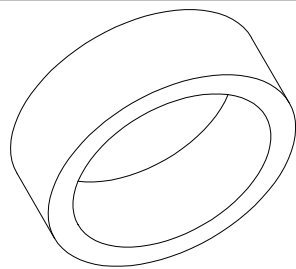
De afwerking van deze afschuining is niet zo belangrijk. Dient enkel om water af te laten lopen

## SECTION A-A

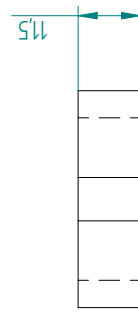
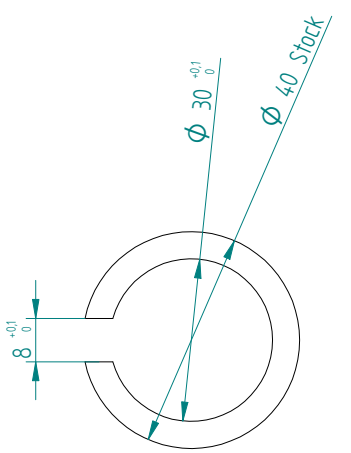
Algemene Ruwheid	Algemene Tolerantie	Materiaal	Plastic	Tekening Nr.	
✓	m				
Schaal	Projectie	Behandeling		Dossier Nr.	Aantal
2:5	∅				1

**KU LEUVEN**

Houder afdichting



✓	Algemeene Ruwheid	Material	Tekening Nr.			
1:1	Algemeene Tolerantie	Aluminium				
	Projectie	Behandeling		Dossier Nr.		
	Schaal			Aantal		
<b>KU LEUVEN</b>				1		
Auteur: Kurt Gebelein				Datum: 01/03/2013		
				A4		



Allgemeine Richtlijn	Allgemeine Tolerancie	Materiaal	Tekening Nr.
✓	0	Aluminium	
Schaal	Projectie	Behandeling	Dossier Nr.
1:1	$\phi$		Aantal
			1

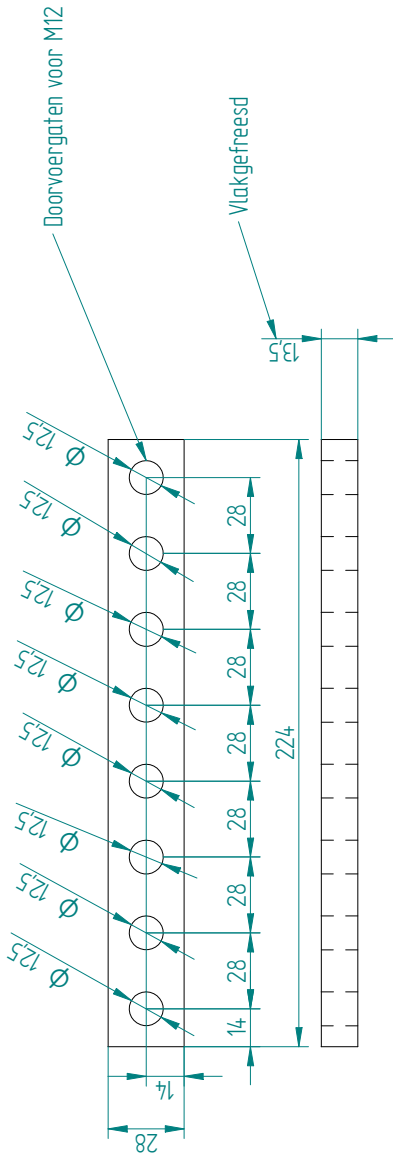
**KU LEUVEN**

Auteur: Kurt Geleijnen

Datum: 01/03/2013

A4

Spacer carousel motor

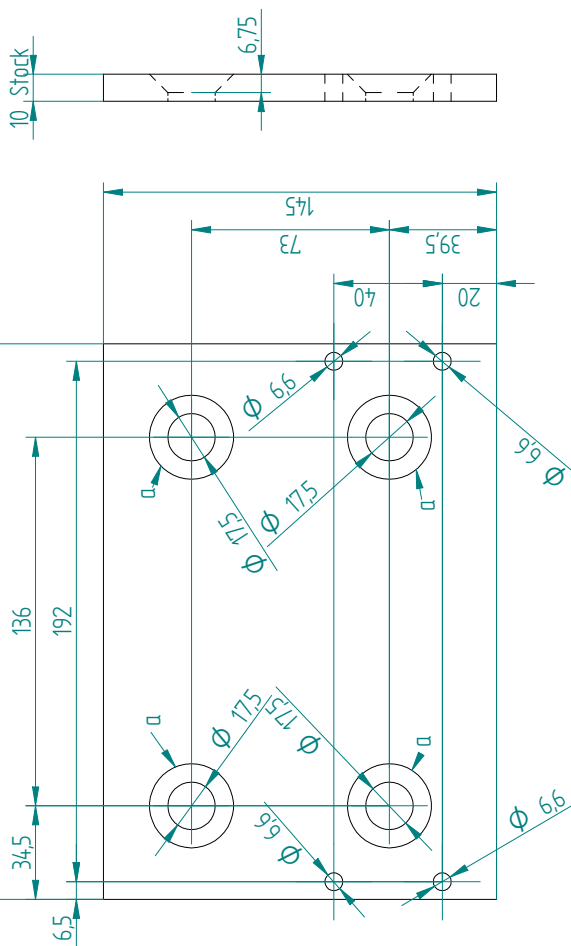
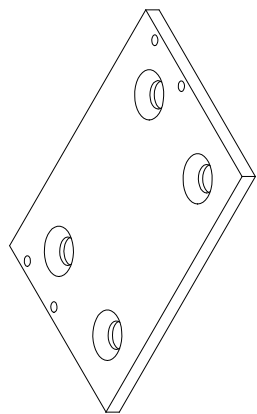


Algemene Richtlijn	Algemene Tolerantie	Materiaal	Tekening Nr.
✓	m	Aluminium	
Schaal	Projectie	Behandeling	Dossier Nr.
1:4			Aantal 1

## Spacerblock

**KU LEUVEN**

a) Identieke gaten voor DIN 7991 bout M16. De bouten worden verzonken

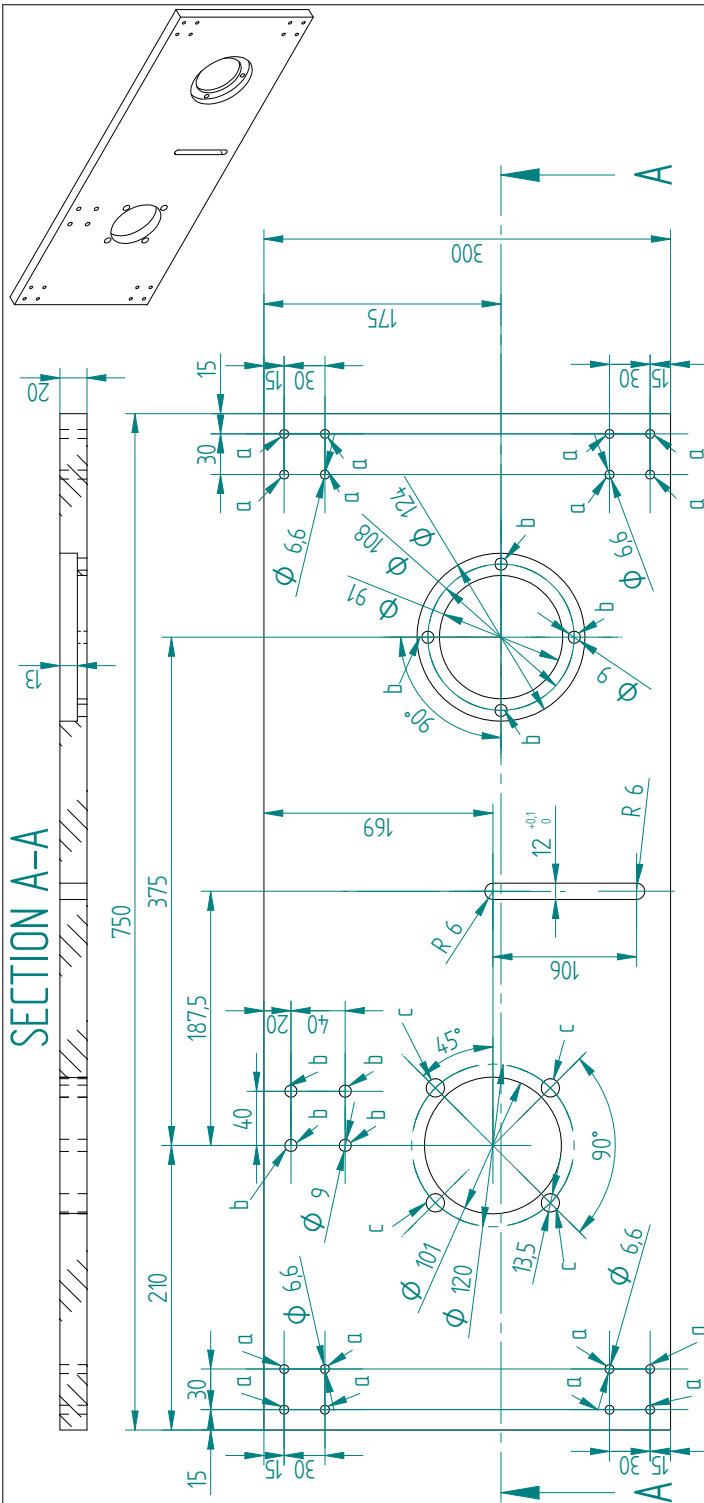


Algemeen		Materiaal		Tekening Nr.
Ruimte	Tolerantie	Projectie	Behandeling	
✓	m		Aluminium	
Schaal				Dossier Nr. Aantal
1:2		∅		1

Swivel plaat

**KU LEUVEN**

# SECTION A-A



Materiaal		Alcoa aluminium	
Algemeen Rodeind	✓	m	
Schaal	1:4	Projectie Behandeling	
a) Identieke doorlopende gaten voor DIN912 bout M6		b) Identieke doorlopende gaten voor DIN912 bout M8	
c) Identieke doorlopende gaten voor DIN912 bout M12		<b>KULEUVEN</b>	

Tekening Nr.

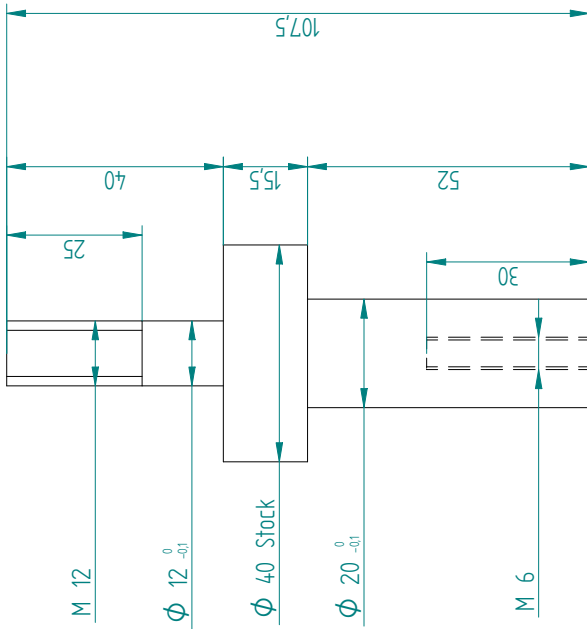
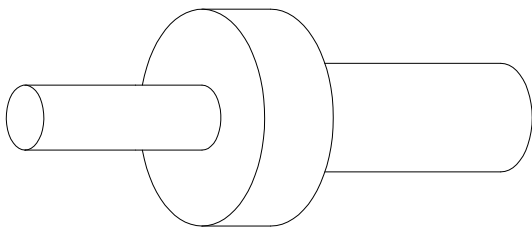
Dossier Nr.

1

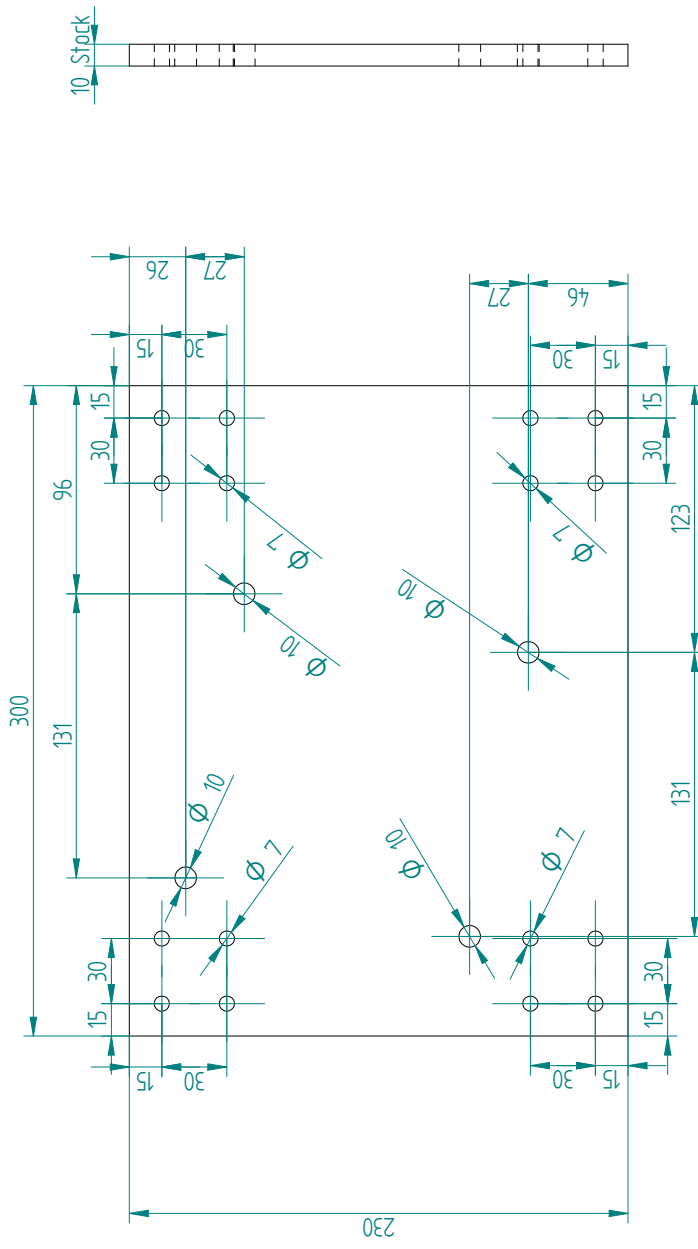
Datum: 28/02/2013

A4

Auteur: Kurt Geethelen



Allgemeine Richtlinie	Allgemeine Tolerancie	Materiaal	
<input checked="" type="checkbox"/>		Aluminium	
Schaal	Projectie	Behandeling	
1:1			
Aansteller: KU LEUVEN			Tekening Nr.:
			Dossier Nr.:
			Aantal:
			1



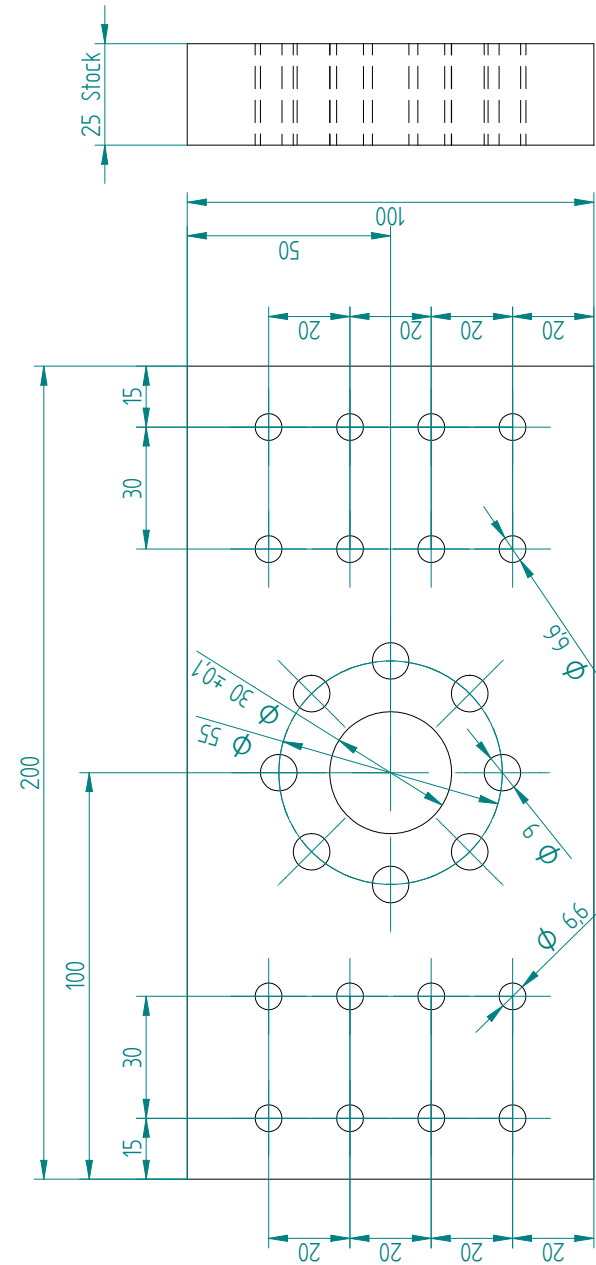
Extra plaat winchhouder

KU LEUVEN

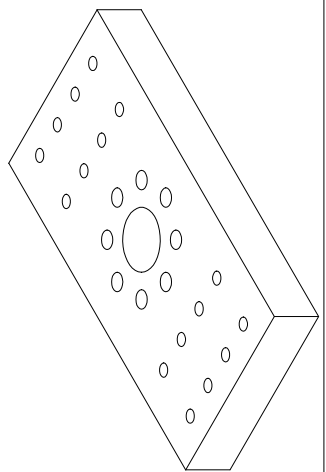
Schuljahr		Projektive Behandeling	Aluminium	Dossier Nr.	Anzahl
2:5					1

Auteur: Kurt Geebelen

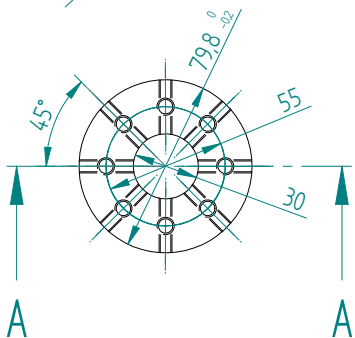
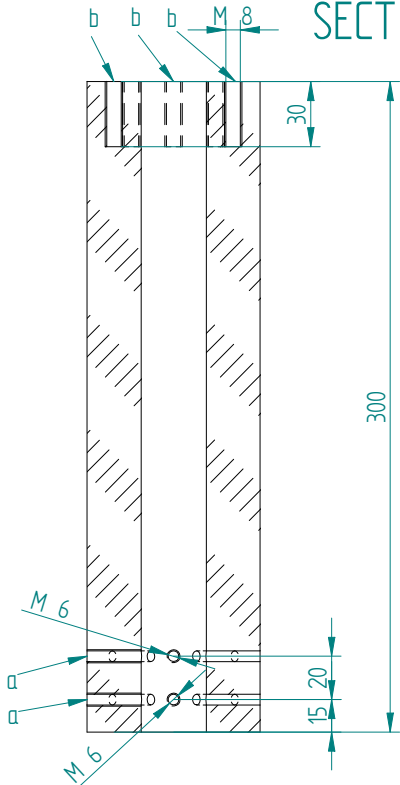
Datum: 28/02/2013



Allgemeine Richtlinie		Materiaal	Tekening Nr.	
m		Aluminium		
Schaal	Projectie	Behandeling	Dossier Nr.	Aantal
3:4	$\phi$			1
<b>KU LEUVEN</b>				A4



## SECTION A-A



Algemene Ruwhed	Algemene Tolerantie	Materiaal Standaard aluminium	Tekening Nr.	
✓	m			
Schaal	Projectie	Behandeling	Dossier Nr.	Aantal
2:5				1

**KU LEUVEN**

Winchhouder

## **Appendix C**

# **Parameters of the dynamic model**

Parameter	Description	Unit	Value
$m$	Mass of the aeroplane	kg	0.685
$A$	Wing area of the aeroplane	$\text{m}^2$	0.105
$b_{\text{ref}}$	Wing span	m	0.96
$c_{\text{ref}}$	Wing cord	m	0.128
$z_T$	Position of tether attachment on aeroplane	m	0.025
$J_{1,1}$	Element of aeroplanes inertia tensor	$\text{kg m}^2$	0.0163
$J_{2,2}$	Element of aeroplanes inertia tensor	$\text{kg m}^2$	-0.0006
$J_{3,3}$	Element of aeroplanes inertia tensor	$\text{kg m}^2$	0.0078
$J_{3,1}$	Element of aeroplanes inertia tensor	$\text{kg m}^2$	0.0229
$r_{\text{Arm}}$	Radius of arm	m	1.085
$J_C$	Rotational inertia of carousel	$\text{kg m}^2$	20
$c_{\text{fric}}$	friction of carousel	kg m	3

Table C.1: Parameters of dynamic model for the indoors carousel. Missing values of the position of tether attachment point and of the inertia tensor are 0.

Parameter	Value	Parameter	Value
$C_{L_\alpha}$	5.475	$C_{R_a}$	0.321
$C_{L_e}$	-0.424	$C_{R_{\omega_x}}$	-0.493
$C_{L_0}$	0.145	$C_{R_{\omega_y}}$	0
$C_{D_\alpha}$	0.0273	$C_{R_{\omega_z}}$	0.0566
$C_{D_{\alpha^2}}$	1.949	$C_{P_\alpha}$	-2.29
$C_{D_{\beta^2}}$	-0.0130	$C_{P_e}$	1.50
$C_{D_e}$	-6.67E-6	$C_{P_{\omega_x}}$	0
$C_{D_{\alpha^2}}$	1.20E-4	$C_{P_{\omega_y}}$	-16.7
$C_{D_{\epsilon^2}}$	3.521E-5	$C_{P_{\omega_z}}$	0
$C_{D_{\alpha,e}}$	-1.01E-4	$C_{P_0}$	-0.0568
$C_{D_{\beta,a}}$	-1.89E-5	$C_{Y_\beta}$	0.0383
$C_{D_0}$	0.107	$C_{Y_{\alpha\beta}}$	-0.0521
$C_{T_\beta}$	-0.132	$C_{Y_{\omega_x}}$	-0.0223
$C_{R_\beta}$	-0.0574	$C_{Y_{\omega_y}}$	0
$C_{R_{\alpha\beta}}$	-0.438	$C_{Y_{\omega_z}}$	-0.0636

Table C.2: Parameters of aerodynamic model (6.21) for the indoors carousel.

# Curriculum Vitae

## Personal Data

NAME: Kurt Geebelen  
DATE OF BIRTH: 27 December 1987  
NATIONALITY: Belgian  
EMAIL: kurt.geebelen@gmail.com

## Professional record

AUG 2010 - APRIL 2015	PhD student at KU Leuven, Belgium Design and Operation of Airborne Wind Energy Systems. <i>Experimental Validation of Moving Horizon Estimation for Pose Estimation.</i>
SUMMER 2009	Internship at Procter & Gamble (Mechelen, Belgium) Optimisation of stock of engines
SUMMER 2003 - 2008	Various student jobs: Puratos (production, 2007-2008), NLDC (production, 2006), Hubrechts B.V.B.A. (warehouse, 2003-2005)

## **Education**

2010 - 2015 KU Leuven, PhD thesis in Mechanical Engineering:  
Design and Operation of Airborne Wind Energy Systems.  
*Experimental Validation of Moving Horizon Estimation for Pose Estimation.*

2008 - 2010 KU Leuven, Master in Mechanical Engineering, with speciality in Thermotechnical Sciences.

2005 - 2008 KU Leuven, Bachelor in Engineering Sciences: Major in Mechanical Engineering, Minor in Electrical Engineering.

## **Languages**

DUTCH: Mothertongue

ENGLISH: Fluent

FRENCH: Fair

## **Computer Skills**

Software Matlab, Maple, Solid Edge, Orocoss, Acado Tookit  
Office Microsoft Office (Word, Excel, Powerpoint)  
OS Mircosoft Windows, Ubuntu Linux  
Programming Java, C, C++, Python, PHP  
Mark-up HTML, Latex

## **Hobbies and interests**

Running, playing recreational football on a weekly basis, tennis, skiing, watching sports and movies, travelling, photography.

# List of publications

## Articles in international journals

**Geebelen, K.**, Vukov, M., Gros, S., Swevers, J., and Diehl, M. Comparison of moving horizon estimators with kinematic and dynamic models based on tethered flight experiments. *IEEE Transactions on Control Systems Technology* (2015). (submitted).

## Articles in academic books

**Geebelen, K.**, Vukov, M., Wagner, D., Ahmad, H., Zanon, M., Gros, S., Vandepitte, D., Swevers, J., Diehl, M. (2013). An Experimental Test Setup for Advanced Estimation and Control of an Airborne Wind Energy System. In: Ahrens U., Diehl M., Schmehl R. (Eds.), bookseries: *Green Energy and Technology, Airborne Wind Energy*, Chapt. 27. Heidelberg, Germany: Springer, 459-471.

## Articles in other academic journals

Paelinck, R., **Geebelen, K.**, Gros, S., Swevers, J., Vandepitte, D., Diehl, M. (2011). Snelle vliegers maken groene stroom. *Het Ingenieursblad*, 5, 16-20.

## Articles in international conference proceedings

**Geebelen, K.**, Wagner, D., Gros, S., Swevers, J., Diehl, M. (2013). Moving Horizon Estimation with a Huber Penalty Function for Robust Pose Estimation of Tethered Airplanes. *Proceedings of the 2013 American Control Conference*. Washington DC, 17-19 June 2013 (pp. 6169-6174).

Gillis, J., Goos, J., **Geebelen, K.**, Swevers, J., Diehl, M. (2012). Optimal periodic control of power harvesting tethered airplanes. *Proceedings of the 2012 American Control Conference*. Montreal, June 27-29 2012 (pp. 2527-2532).

Gros, S., Ahmed, H., **Geebelen, K.**, Swevers, J., Diehl, M. (2012). In-flight Estimation of the Aerodynamic Roll Damping and Trim Angle for a Tethered Aircraft based on Multiple-shooting. *16th IFAC Symposium on System Identification*. Brussels, Belgium, 11-13 July 2012 (pp. 1407-1412).

**Geebelen, K.**, Ahmed, H., Vukov, M., Gros, S., Swevers, J., Diehl, M. (2012). An experimental test set-up for launch/recovery of an Airborne Wind Energy (AWE) system. *Proceedings of the 2012 American Control Conference*. Montreal, June 27-29 2012 (art.nr. 918) (pp. 4405-4410).

Ferreau, H., Houska, B., **Geebelen, K.**, Diehl, M. (2011). Real-time control of a kite-model using an auto-generated nonlinear MPC algorithm. *Proceedings of the IFAC World Congress*. Volume 18 (1). Milano, Italy, 28 August 2011

## Abstracts in conference proceedings

**Geebelen, K.**, Wagner, D., Clinckemaillie, M., Stuyts, J., Vandermeulen, W., Vandepitte, D., Swevers, J., Diehl, M. (2013). The New Highwind Carousel for Outdoor Rotational Start Experiments. *Book of abstracts of the Airborne Wind Energy Conference*. Berlin, 10-11 September 2013.

**Geebelen, K.**, Swevers, J., Diehl, M. (2012). Moving horizon estimation for airborne wind energy systems. *Proceedings of the 31th Benelux Meeting on Systems and Control*. Heijen/Nijmegen, The Netherlands, March 27-29 2012.

Gillis, J., **Geebelen, K.**, Sternberg-Kaletta, J., Gros, S., Houska, B., Diehl, M. (2012). Lyapunov based design of robust linear-feedback for time-optimal periodic quadcopter motion. *Proceedings of the 31th Benelux Meeting on Systems and Control*. Heijderbos, Heijen/Nijmegen, The Netherlands, March 27-29, 2012.

**Geebelen, K.**, Vukov, M., Swevers, J., Diehl, M. (2011). First Feedback Control Tests for Fast Flying Tethered Airplanes. *Book of abstracts of the Airborne Wind Energy Conference*. Leuven, Belgium, 24-25 May 2011.

**Geebelen, K.**, Gillis, J., Swevers, J., Diehl, M., Vandepitte, D. (2011). Automatic control of tethered airplanes for kitepower applications. *Proceedings of the Benelux Meeting on Systems and Control*. Lommel, 15-17 March 2011.

**Geebelen, K.**, Gillis, J., Swevers, J., Diehl, M. (2010). Modelling and control of tethered airplanes for wind energy harvesting. *Book of abstracts of the DYSCO Study Days*. Court-Saint-Etienne, November 28-29 2010.





FACULTY OF ENGINEERING SCIENCE  
DEPARTMENT OF MECHANICAL ENGINEERING  
DIVISION OF PRODUCTION ENGINEERING, MACHINE DESIGN AND AUTOMATION  
Celestijnenlaan 300B box 2420  
B-3001 Leuven  
[kurt.geebelen@gmail.com](mailto:kurt.geebelen@gmail.com)  
[www.mech.kuleuven.be](http://www.mech.kuleuven.be)

